Impact des associations fer-matière organique sur la dynamique de l'arsenic

Hélène Guénet

ANNÉE 2016

THÈSE / UNIVERSITÉ DE RENNES 1
sous le sceau de l'Université Bretagne Loire

pour le grade de

DOCTEUR DE L'UNIVERSITÉ DE RENNES 1

Mention : Sciences de la Terre

Ecole doctorale Sciences de la Matière

Hélène Guénet

Préparée à l'unité de recherche Géosciences Rennes
(UMR CNRS 6118)
OSUR Observatoire des Sciences de l'Univers de Rennes

Impact des associations fer-matière organique sur la dynamique de l'arsenic

Thèse soutenue à Rennes
le 5 octobre 2016

devant le jury composé de :

Laurent MICHOT
Directeur de recherche, CNRS, UPMC / *rapporteur*

Jérôme ROSE
Directeur de recherche, CNRS, CEREGE / *rapporteur*

Georges ONA-NGUEMA
Maitre de conférences, UPMC / *examinateur*

Cécile QUANTIN
Professeur, Université Paris Sud / *examinateur*

Mélanie DAVRANCHE
Professeur, Université de Rennes 1 / co-*directrice de thèse*

Delphine VANTELON
Responsable de ligne, Synchrotron SOLEIL / co-*directrice de thèse*

Jacques JESTIN
Chargé de recherche, CNRS, LLB / co-*directeur de thèse*

Remerciements

C'est la fin d'une belle aventure de trois ans !! Dire que le temps passe vite est un euphémisme lorsqu'on est bien entouré. Je voudrais donc remercier toutes les personnes que j'ai rencontrées, qui m'ont soutenues et qui ont contribuées de près ou de loin à ce projet.

Tout d'abord, un grand merci à ***Mélanie Davranche****, directrice de cette thèse et par qui tout a commencé. Merci pour ta grande disponibilité et ta confiance, j'ai énormément appris à tes côtés. Merci aussi de m'avoir botté les fesses quand il le fallait. Merci également d'avoir partagé avec moi la joie des manip synchrotron. Il faut souffrir pour avoir de belles données : la fatigue des nuits très (très) courtes et le stress des bugs en tout genre (je crois qu'on aura tout eu ! Entre le cryostat qui ne marche pas et les miroirs KB qui cassent…). Mais j'ai adoré ça et cela nous a donné l'opportunité de visiter des endroits plutôt sympas (San Francisco, Londres).*

Merci également à mes co-directeurs de thèse, ***Delphine Vantelon*** *et* ***Jacques Jestin*** *qui ont permis de nouer une collaboration entre le synchrotron SOLEIL, le LLB et l'université de Rennes 1. Je tiens à vous remercier pour votre investissement dans cet ambitieux projet.*

Merci aux membres de mon jury d'avoir pris le temps de relire et de juger ce travail. Merci à ***Jérôme Rose*** *et* ***Laurent Michot*** *pour leurs rapports très encourageants. Un grand merci à* ***Georges Ona-Nguema*** *et* ***Cécile Quantin*** *pour leurs questions et leurs critiques constructives. Grâce à vous cette soutenance de thèse a été un réel plaisir pour moi.*

Je tiens à remercier toute l'équipe Géochimie des Eaux et des Interfaces impliquée de près ou de loin dans ce projet:
Tout d'abord merci infiniment ***Martine*** *pour ta gentillesse, ton professionnalisme et pour les discussions plus personnelles que nous avons pu avoir. Merci également pour tout le temps que tu as passé avec moi sur l'HPLC/SEC (ou communément appelé, « les milles et une façons de déboucher des colonnes »).*
Merci ***Aline*** *pour toutes les relectures et corrections mais également pour ton accueil dans ton bureau pour mon dernier mois de rédaction.*
Anne-Catherine*, je voudrais te remercier pour ton écoute et toutes nos discussions (non c'est faux nous ne sommes pas du tout bavardes) mais également pour ton aide précieuse pour la Fluo 3D.*
Merci ***Patrice*** *pour ton côté McGyver (qui m'a bien aidé surtout lors de ma première année) et ta disponibilité lorsque j'avais un souci dans le labo.*
Merci également à ***Emilie*** *et* ***Julien*** *pour les analyses sur le GC et la DLS, qui ont été essentielles dans la construction de mon deuxième papier.*

Je voudrais maintenant remercier la première ligne de front, ceux qui m'ont supportée tous les jours (les bons comme les mauvais) : j'ai nommé le bureau 321 !!

***Cha'** , on se sera suivie pendant toute ma thèse finalement. Merci de m'avoir accueillie dans le labo à mon arrivée. Merci pour ta bonne humeur, d'avoir été présente pour moi (et oui la thèse est un ascenseur émotionnel permanent comme tu le sais) et pour toute les petites choses qui font que tu nous as manqué quand tu es partie vers d'autres horizons (oui bon d'accord Bordeaux ce n'est pas si loin mais quand même). Promis maintenant je fais attention quand je prends des embouts de pipette dans la boîte (bon ok non c'est faux je suis toujours aussi désordonnée mais au moins ça me fait rire et penser à toi).*

***Marie**, dixit wokdenouille (en un seul mot), quoi dire à ton propos… Ton arrivée parmi nous en provenance de l'Allemagne, pardon de la Lorraine, n'a été que du bonheur. Merci pour tous nos fous rires : ton imitation de l'accent alsacien, ça marche à tous les coups (« yopla »). J'ai trouvé mon alter ego de références pourries (« Monsieur n'est pas une tapette, monsieur est commissaire de police »). Merci également pour toutes nos sorties ciné/restau/papotage. Et pour finir merci d'avoir découvert avec moi le bonheur des urgences de Pontchallou un dimanche soir après une partie de badminton endiablée (même pas mal d'abord).*

*Merci **Edwige** pour ta gentillesse et de m'avoir fait un petit guénej' dans ma dernière ligne droite de rédaction de thèse. Et grâce à toi j'aurais une super piñata pour décorer mon prochain bureau !*

*Et non il n'y a pas que des filles dans ce bureau ! Thank you **Sen** for your cheerfulness and your patience with the chatty girls of your office. Merci également à **Pierre-Louis** qui, pendant un an, a été notre médiateur de bureau et aussi un peu Monsieur Potin (avoue-le).*

*Un grand merci aussi à LaSalle/Bordeaux etc. qui nous a envoyé **Sandra** à Rennes. Je me souviens, Sandra, de tes remerciements de thèse qui m'ont tiré une petite larme. Je n'ai pas la prétention de pouvoir rivaliser en quelques phrases je vais donc aller à l'essentiel. Merci pour tous nos moments passés ensemble, nos moments de filles et de remontage de moral. Merci d'être partie 2 semaines en vacances en Irlande juste après mon rendu de manuscrit. D'avoir développé ton côté aventureux pour moi (que c'est dur le camping sauvage). J'attends avec impatience le Guénet-Brocheray illustré n°3 !!*

*Un énorme merci à **Stéphanie** de Verbigier, notre super gestionnaire. Merci d'avoir abandonné ta flopée de petits monstres et d'être revenue un mercredi pour ma soutenance de thèse. J'ai adoré nos papotages et rires dans ton bureau et que tu ais participé à la confection des confettis pour remplir ma piñata d'anniversaire. Et surtout (j'ai failli oublier !), merci de m'avoir fait découvrir Cary Grant !*

*Je voudrais également remercier les nombreux doctorants, post-doc et ingénieurs qui font la bonne ambiance unique de Geosciences Rennes. Pour tous les bons moments passés avec vous, les week-end plages, les soirées bar et parties de volley du vendredi soir, merci à **Aurélie**, **Marie-Françoise**, **Diana**, **Redj**, **Eliot**, **Jérôme**, **Sylvia**, **Luc**, **Olivier**, **Romain**, **Lucas**, **Louise**, **Dany**, **Charline**, **Baudouin** (t'es trop cool), **Maxime**, **Pochon**, **John** (et **Emma**), **Camille**, **Nataline**, **Gemma**, **Bob**, **Polo**, **Guillaume**, **Marie**, **Antoine**… En espérant ne pas en avoir oublié trop d'entre vous.*

Une petite pensée à mes amis de Poitiers que j'ai beaucoup moins vu lors de ces trois dernières années : ***Jacques, Florian, Will, Damien, Chi-Wei, Joce, Mat, Guigui, Pib*** *et* ***Alice*** *…*

S'il existe des histoires d'amour en amitié c'est bien avec toi ***Elise****. Merci d'être dans ma vie depuis… oulà 9 ans déjà!! Merci d'être toujours là pour moi dans les bons moments comme dans les moins bons. Merci pour tous les voyages en amoureuses que l'on a faits et pour tous ceux à venir (prochaine étape l'Islande !!).*

Un grand merci également à ma famille pour son soutien inconditionnel. A mes parents et ma grande sœur, mais également à Paul et Brigitte que j'aime énormément. Une pensée pour Pierre, mon beau-frère préféré, je vais enfin pouvoir assurer mon rôle de (vieille) tante et marraine pour Anastase et Blanche.

Un homme est fait de choix et de circonstances.
Personne n'a de pouvoir sur les circonstances mais chacun en a sur ses choix.
Eric-Emmanuel Schmitt

Sommaire

Chapitre I. Introduction générale

I.1 L'arsenic

I.1.1 Un élément ubiquiste

L'arsenic, de symbole chimique As et de numéro atomique 33, est le 47ème élément en abondance sur Terre. L'arsenic est un métalloïde au comportement chimique intermédiaire entre les métaux et les non-métaux qui présente de fortes analogies avec le phosphore. Il est ubiquiste car présent dans les trois couches de la géosphère (pédosphère, hydrosphère et atmosphère). Il est globalement six mille fois plus important dans la croûte terrestre qu'il ne l'est dans la pédosphère et l'hydrosphère réunies, alors que sa concentration dans l'atmosphère, issue des volcans, des activités humaines, des feux de forêt et des embruns, est négligeable en proportion (Matschullat, 2000). Son abondance moyenne dans la croûte terrestre est de 1.5 mg kg^{-1}. Les concentrations en As dans différents compartiments terrestres et maritimes sont données dans la Tableau I.1. Les roches sédimentaires, telles que les schistes, le charbon et les mudstones, sont les plus riches en As. Les concentrations types dans les eaux naturelles sont plus faibles, avec des valeurs plus élevées dans les rivières (0.83 mg L^{-1}) et les eaux de mer profonde (1.0-1.8 mg L^{-1}) que dans les lacs (0.28 mg L^{-1}) et les eaux de pluie (0.02 mg L^{-1}). Cependant, ces concentrations de référence peuvent être dramatiquement accrues pour des sites industriels pollués tels que des mines ou environnements naturels spécifiques tels que les systèmes géothermaux (Smedley and Kinniburgh, 2002). Le haut niveau de pollution en As dans les eaux et les sols est un phénomène mondial comme le montre la Figure I.1.

Dans notre esprit, l'arsenic est associé aux poisons, que ce soit à travers l'Histoire, avec la mort de François 1er de Médicis et l'hypothèse de l'empoisonnement de Napoléon Bonaparte, ou à travers les romans et les films (Madame Bovary, « Arsenic et vieilles dentelles »). Cependant, l'As a également un usage industriel. Il a été pendant très longtemps utilisé dans les insecticides (e.g. diméthylarsinate de sodium), les désherbants et les préservateurs du bois (Smedley and Kinniburgh, 2002). Historiquement, il rentra

également dans la composition de pigments pour la peinture et les céramiques. Son utilisation a toutefois beaucoup diminué, en partie grâce à une meilleure connaissance de sa toxicité même à faible dosage.

Tableau I. 1 Concentrations en As dans le compartiment terrestre et marin (données extraites de Smedley and Kinniburgh, 2002).

Concentrations en As dans les roches, sédiments et sols		
Type de roche/sédiment/sol	**Concentration moy. en As (mg kg^{-1})**	**Gamme (mg kg^{-1})**
Basalte	2.3	0.18-113
Andésite	2.7	0.5-5.8
Granite	1.3	0.2-15
Ardoise/phyllite	18	0.5-143
Mudstone/schiste marin	3-15	< 490
Grès	4.1	0.6-120
Calcaire/dolomite	2.6	0.1-20.1
Evaporites	3.5	0.1-10
Charbons	-	0.3-35.000
Sédiments de rivière	5	-
Sédiments de marge	-	2.3-8.2
Tourbes et sols marécageux	13	2-36
Sols sulfatés acides (Canada)	-	1.5-45
Concentrations en As des eaux naturelles		
	Concentration moy. en As (mg L^{-1})	**Gamme (mg L^{-1})**
Eaux de pluie:		
maritime	0.02	-
terrestre	-	0.013-0.032
Rivières (valeur référence)	0.83	0.13-2.1
Eaux de mer profondes	-	1.0-1.8
Eaux géothermales	-	< 10-50,000
Lac:		
Colombie-Britannique	0.28	< 0.2-0.42
France	-	0.73-9.2
Eaux souterraines:		
Angleterre	-	< 0.5-10
Bengale, Argentine, Mexique, Taiwan	-	10-5000

Comme le montre la Figure I.1, la contamination naturelle en As des aquifères couvre de larges zones. La consommation des eaux contaminées est donc une problématique pour des millions de personnes dans le monde, notamment au Bengladesh, en Argentine, au Chili, au Mexique, en Chine et en Thaïlande. L'Organisation Mondiale de la Santé (OMS) a ainsi décrit ce problème comme « le plus grand empoisonnement de masse de l'histoire de l'humanité ». Il est donc d'un intérêt majeur d'appréhender la toxicité de l'As, ses origines et son comportement dans l'environnement.

Figure I. 1 Distribution mondiale des zones hautement polluées en As, associées à des sources hydrothermales, à une exploitation minière ou à des aquifères contaminés (Smedley and Kinniburgh, 2002).

I.1.2 Toxicité et formes de l'arsenic

L'arsenic est un bon exemple du lien entre la spéciation d'un élément et sa toxicité. En effet, sa forme chimique conditionne son impact sur la santé humaine et les organismes vivants. En solution, l'arsénite, sous forme H_3AsO_4, a des pKa de 9.2, 12.1 et 13.4 alors que l'arseniate a des pKa de 2.2, 6.9 et 11.5. Ainsi, dans eaux à pH proche de la neutralité, les formes dominantes de l'As seront $H_2AsO_4^-$, $HAsO_4^{2-}$ et H_3AsO^0 (Figure I.2). De nombreuses formes organiques sont retrouvées dans l'environnement suite à des

réactions de biométhylation de l'As inorganique. Les plus courantes sont les formes méthylées comme le monométhylarséniate (MMA), le diméthylarséniate (DMA) et l'arsénobétaine (AB). La plupart des arséno-sucres et arséno-lipides sont considérés comme étant les produits finaux de la réaction de détoxification par les micro-organismes et les invertébrés (Dembitsky and Rezanka, 2003). La Figure I.3 est un résumé des formes inorganiques et organiques de l'As présentes dans l'environnement.

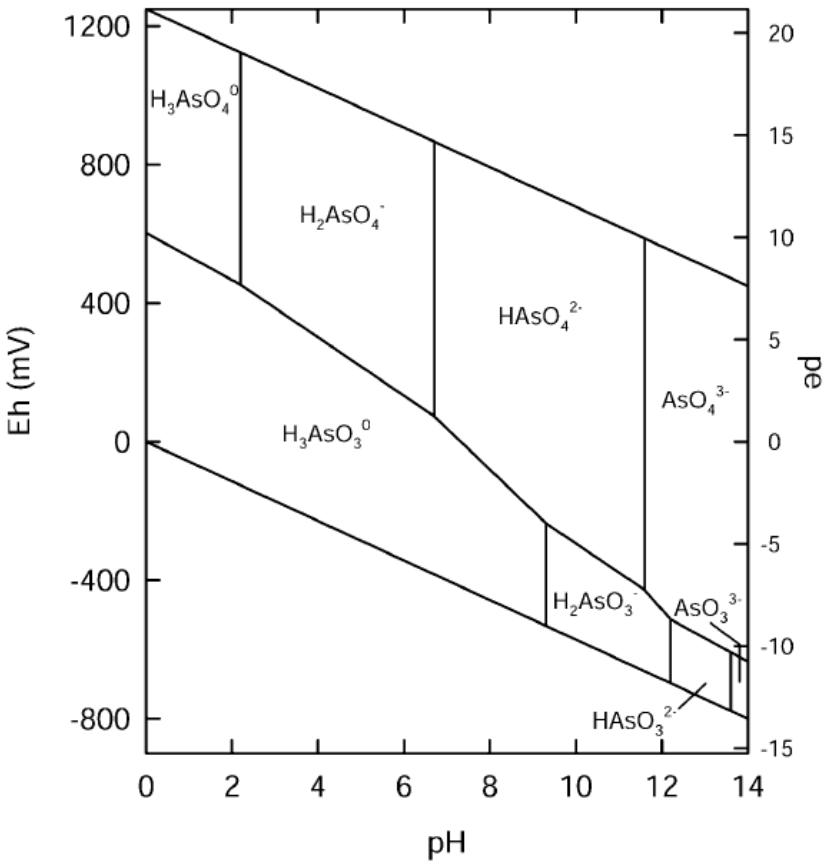

Figure I. 2 Diagramme Eh-pH de l'arsenic en solution dans un système As-O_2-H_2O à 25°C et une pression de 1 bar (Smedley and Kinniburgh, 2002).

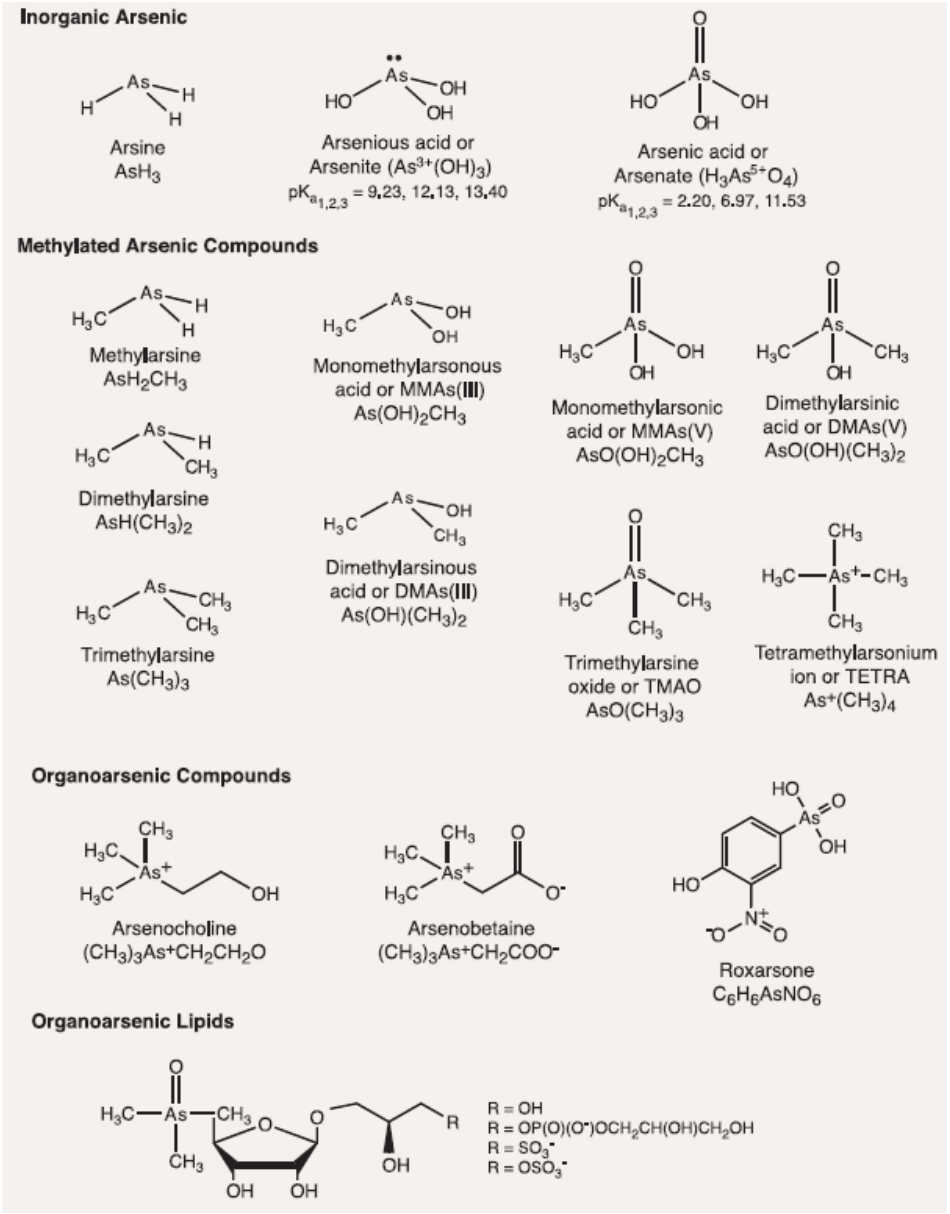

Figure I. 3 Les différentes formes de l'As (O'Day, 2006).

La forme d'As la plus toxique est le gaz arsine (AsH_3, AsIII), suivi par l'arsénite (AsO_3^{3-}, AsIII) puis l'arséniate (AsO_4^{3-}, AsV), les deux derniers pouvant être transportés en solution. L'As(V) est beaucoup moins toxique sous ses formes organiques, telles que l'AB (la principale forme d'As dans le poisson), le DMA et le MMA. Cependant, des études ont montré que le MMA et DMA, à l'état d'oxydation +III, sont beaucoup plus toxiques que les formes inorganiques (Mass et al., 2001). Le fait que l'As(III) soit considéré comme étant 60 fois plus toxique que l'As(V) (Jain and Ali, 2000) s'explique en grande partie par sa propension à se complexer au soufre de nombreuses protéines et ainsi à perturber leur fonctionnement. Par sa seule présence et à fort

dosage, il peut ainsi inhiber la production de plus de 200 enzymes humaines (Abernathy et al., 1999). Cependant, l'arséniate est capable de remplacer le phosphate dans les chaînes d'ADN et les voies de respiration cellulaire (O'Day, 2006).

L'exposition quotidienne et sur le long terme, même à une faible concentration en As, est actuellement la plus grande préoccupation des grandes instances de santé publique. En effet la consommation d'eaux contaminées (boisson et agriculture) favorise l'apparition de différents types de cancers (peau, vessie, rein, foie, prostate, etc.), diabète, maladies vasculaires, hypertension, troubles neurologiques, problèmes de reproduction ainsi que des lésions cutanées (Figure I.4). Suivant les recommandations de l'OMS, l'agence de protection de l'environnement américaine (APE) a imposé en 2001 une limite acceptable de potabilité des eaux à 10 µg L^{-1}. Cependant, dans les pays moins développés cette limite reste à la valeur déterminée en 1993 qui est de 50 µg L^{-1}.

Figure I. 4 Signes extérieurs de la toxicité de l'arsenic par la consommation de l'eau contaminée des puits au Bengladesh (©AP Photo/Pavel Rahman et Heng Chivoan).

I.1.3 Causes de la contamination naturelle des aquifères en arsenic

La présence d'une grande quantité d'As dans les eaux souterraines peut être expliquée par plusieurs mécanismes, propres à chaque système.

Dans la région du Bengladesh, où des millions de personnes sont exposées, l'épidémie en As est la conséquence malheureuse d'une décision de changement de l'approvisionnement en eau. Les eaux de

surface étaient autrefois largement utilisées pour se laver, boire ou cuisiner. Or la consommation de ces eaux, microbiologiquement très riches (virus, bactéries et parasites), étaient à l'origine de nombreuses maladies et décès, notamment chez les jeunes enfants. Ainsi, sous l'impulsion du gouvernement, des milliers de puits ont été creusés dans les années 70 pour avoir accès à une eau propre à la consommation humaine. Cependant, personne ne suspecta la présence d'une grande quantité d'As dans ces eaux souterraines que le forage des puits avait permis de libérer. S'il est établi que l'As des eaux souterraines provient des sédiments hôtes, plusieurs mécanismes peuvent expliquer sa libération. Le premier concerne l'entrée massive d'oxygène suite à la baisse du niveau de la nappe par pompage qui entraînerait l'oxydation des sulfures contenus dans les sédiments d'aquifère et donc la libération de l'As associé (via l'oxydation d'arsénopyrite, FeAsS). Un deuxième mécanisme concerne la dissolution réductive d'oxyhydroxydes de fer porteurs de l'As contenu dans les sédiments de l'aquifère par des bactéries ferri-réductrices. Les oxydes de Fe sont présents dans les sédiments des aquifères issus de l'altération par exemple de la chaîne himalayenne. Cette étape de réduction nécessite un apport de matière organique (MO) biodégradable, qui est utilisée soit comme source de carbone nécessaire à la croissance bactérienne soit comme source d'énergie où les oxydes de fer jouent le rôle d'accepteur d'électrons. Le Fe(III) solide est réduit en Fe(II) soluble, libérant en solution sa charge en métaux et métalloïdes, tels que l'As (Davranche et al., 2011; Dia et al., 2015; Grybos et al., 2007; Olivié-Lauquet et al., 2001). La MO introduite dans le système peut avoir plusieurs origines. Elle peut provenir de couches de tourbes intercalées dans le sédiment dont la solubilisation est induite par l'augmentation des flux hydriques dus au pompage (McArthur et al., 2004) ou de la surface en conséquence de l'irrigation intensive (Harvey et al., 2006).

Dans le delta du Mékong, un autre mécanisme de contamination des eaux souterraines mettant en jeu les plaines d'inondation a été mis en évidence (Kocar et al., 2008; Polizzotto et al., 2008). L'altération de roches de l'Himalaya produit une grande quantité de sédiments riches en oxydes de fer porteurs d'As. Ces sédiments sont transportés par le Mékong. Lors des crues du fleuve, ils sont déposés dans les plaines d'inondation et les zones humides adjacentes. Ces zones sont très riches en MO et sont soumises à des alternances des conditions d'oxydo-réduction. En période de crues, le milieu est saturé en eau et devient

anoxique. Les bactéries ferri-réductrices réduisent les oxydes de fer, libérant en solution l'As associé qui est par la suite réduit en As(III). Celui-ci aurait alors la possibilité de transiter jusqu'aux aquifères sous-jacents (Kocar et al., 2008; Polizzotto et al., 2008; Fendorf, 2010).

I.2 Les zones humides (ZH)

Une caractéristique clé de la mobilité de l'As, et de son impact sur la santé humaine, est donc l'instauration de conditions anoxiques dans un substrat riche en Fe. Cette anoxie peut être provoquée par l'entrée massive de MO de surface (région du Bengladesh) ou par une saturation en eau (plaines du Mékong). Dans ce travail, je me suis plus particulièrement intéressée au rôle des zones humides qui peuvent être réduites ou connaître des alternances des conditions d'oxydo-réduction et sont riches en MO, en Fe mais aussi, pour certaines, en As (Kalbitz and Wennrich, 1998; Anawar et al., 2003).

Les ZH sont présentes sous tous les climats et couvrent environ 6% des surfaces terrestres dans le monde ce qui équivaut à 800 millions d'ha. Elles sont localisées à l'interface des systèmes terrestres et aquatiques (e.g. lacs, rivières, estuaires ou océans) ou dans des bassins isolés dans lesquels le battement de la nappe souterraine est très important. De par leur localisation, les ZH contrôlent les flux de nutriments en provenance des terres vers le système aquatique et servent donc de zone tampon. Elles peuvent alors servir de source, de piège ou de transformateur des contaminants. Par conséquent, ces milieux extrêmement dynamiques sont d'une importance capitale dans la régulation des cycles biogéochimiques des éléments majeurs et traces. (Mitsch and Gosselink, 2000).

Parmi ces zones humides, on peut distinguer les zones humides adjacentes aux cours d'eau, lacs ou rivières, communément appelées zones humides ripariennes. Elles constituent un groupe particulier au regard des fortes variations des conditions hydrologiques qu'elles subissent. La présence d'eau peut y être pérenne, intermittente ou éphémère. En plus des précipitations, les sources d'eau des ZH ripariennes sont de trois origines : i) l'écoulement des eaux souterraines, ii) les flux de sub-surface des zones en amont et iii) les flux provenant des masses d'eau adjacentes (Mitsch and Gosselink, 2000) (Figure I.4). Ces zones ont une nappe d'eau souterraine proche de la surface et subissent un ennoiement saisonnier ou périodique. La

végétation s'est adaptée à ces conditions et est composée généralement de macrophytes, de graminées et d'arbres.

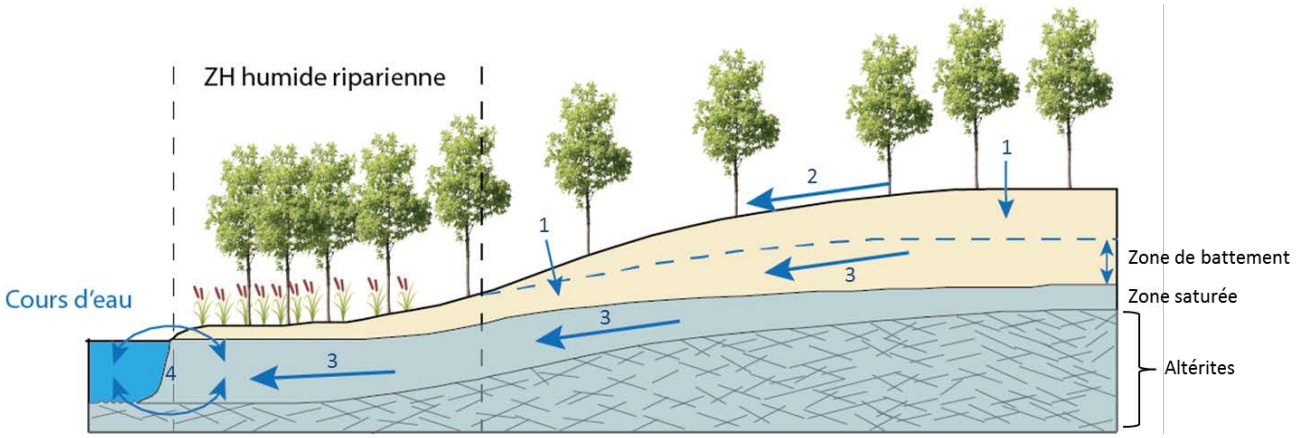

Figure I. 5 Schéma du fonctionnement hydrologique d'une zone humide riparienne, 1 : infiltration, 2 : ruissellements de surface, 3 : ruissellements de sub-surface, 4 : échanges nappe/rivière/zone humide

Le sol des ZH ripariennes est défini comme un sol minéral alluvial dont l'horizon organique subit des périodes de saturation en eau suffisamment longues pour induire le développement de conditions anaérobies (Mitsch and Gosselink, 2000). Ainsi, les quinze premiers centimètres du sol correspondent à l'horizon du sol où les cycles biogéochimiques et l'activité biologique sont les plus importants. Lorsque l'eau sature le sol, les échanges gazeux avec l'atmosphère deviennent limités et la quantité d'O_2 disponible pour la respiration des bactéries du sol diminue drastiquement. Ces dernières doivent donc utiliser d'autres accepteurs d'électrons pour consommer/minéraliser la MO (Figure I.6). Les premiers éléments chimiques à être réduits sont les nitrates, NO_3. Lorsque ceux-ci ont été consommés, les oxydes de manganèse MnO_2 sont réduits, ce qui se traduit par l'augmentation de la teneur en Mn^{2+} en solution puis les oxydes de fer, FeOOH, et les sulfates, SO_4^{2-}, ce qui se traduit par une augmentation du Fe^{2+} puis de HS^- en solution. Lorsque l'anaérobie devient très forte, la méthanogénèse peut avoir lieu. Cette succession d'accepteurs d'électrons se traduit par une diminution du potentiel d'oxydo-réduction (Eh) et une augmentation du pH (Figure I.6).

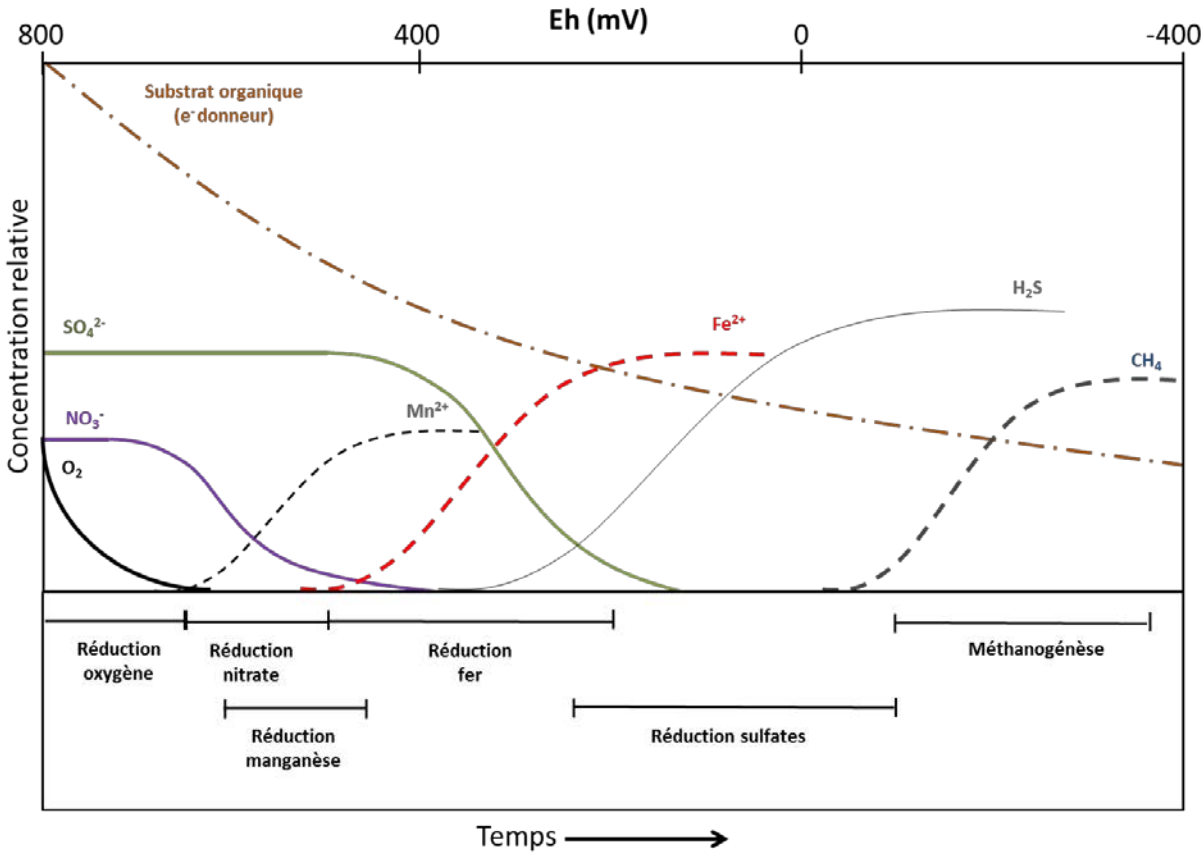

Figure I. 6 Séquence des transformations des éléments dans le sol en fonction du temps après saturation en eau (Reddy and Delaune, 2008).

Dans ce travail, nous nous sommes intéressés à la zone humide riparienne de Kervidy localisée dans le bassin versant de Naizin Kervidy dans le département du Morbihan (48°N, 3°W) (Figure I.7). Ce bassin correspond à la partie nord du bassin versant du Coët-Dan. Des études réalisées sur cette ZH ont pu mettre en évidence la présence d'As dans le sol et dans les eaux (Davranche et al., 2013; Al Sid Cheikh et al., 2015). Le socle de cette ZH est constitué de schistes du briovérien qui, en s'érodant, ont libéré des minéraux porteurs d'As. Cette zone est donc un parfait cas d'étude du comportement de l'As au cours des variations d'oxydo-réduction en ZH. Cette ZH a le second avantage de faire partie d'un Observatoire de Recherche en Environnement (ORE) appelé AgrHys. Des suivis géochimiques des eaux souterraines et des solutions de sols sont réalisés depuis plusieurs décennies et ont permis de bien comprendre le fonctionnement pédo-hydo-climato-géochimique du bassin versant dans laquelle se trouve notre zone d'étude. La superficie de ce bassin

est de 5 km². Le climat de cette zone est tempéré sous influence océanique avec une température annuelle moyenne de 11°C pour la période 2000-2012. Le cumul des précipitations moyennes est de 818 mm an^{-1}.

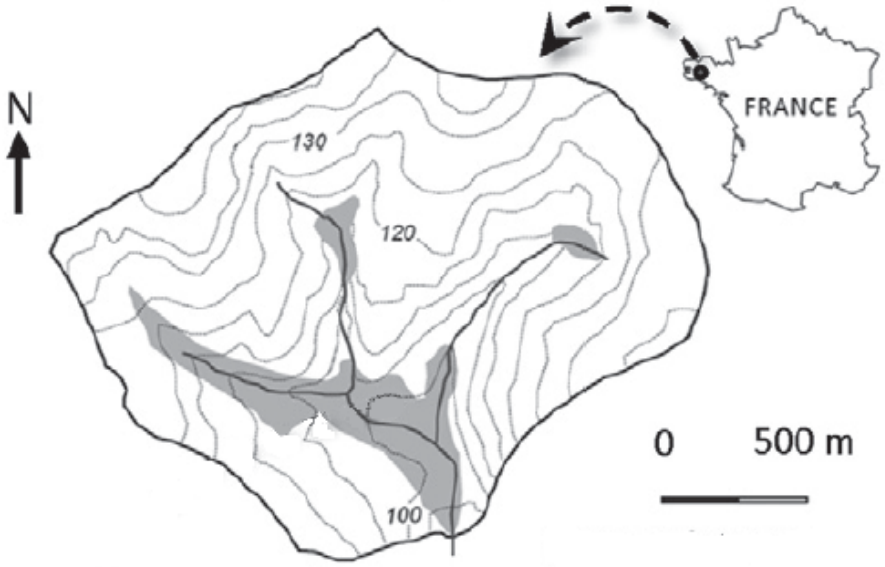

-Figure I. 7 Localisation du bassin versant de Naizin-Kervidy (Bretagne, France). La zone grisée correspond à l'étendue maximale de la zone humide (Dia et al., 2000).

I.3 Interactions entre l'arsenic, le fer et la matière organique.

Comme je l'ai montré précédemment, le cycle biogéochimique de l'As est en étroite interaction avec celui du Fe et du C. Il convient donc de faire un état des lieux des connaissances sur les interactions possibles entre ces 3 éléments chimiques.

I.3.1 Arsenic et matière organique

I.3.1.1 Les processus de complexation

La matière organique, et plus spécifiquement sa fraction la plus réactive représentée par les acides humiques et fulviques, possède une grande quantité de groupements fonctionnels complexants (i.e. carboxyliques, phénoliques, thiols, amines etc.). Dans les conditions de pH des eaux naturelles, ces groupements se déprotonent et confèrent à la MO une charge globalement négative (Sposito and Weber, 1986; Kim et al., 1990; Tipping et al., 2002). L'As, quant à lui, est présent sous forme d'oxyanion qui peut être neutre ou chargé négativement lorsqu'il est en solution. Ainsi, les interactions entre l'As et la matière

organique globalement négative ne semblent pas favorisées de prime abord. Cependant, plusieurs études ont montré que l'As était capable de se lier à la MO (Thanabalasingam and Pickering, 1986; Lenoble et al., 2005; Warwick et al., 2005; Buschmann et al., 2006; Kappeler et al. 2006; Liu and Cai, 2010).

Buschmann et al., (2006) et Lenoble et al. (2005) suggèrent que la complexation de l'As(III, V) peut se faire via les groupements carboxyliques et phénoliques qui sont les sites les plus abondants au sein de la MO. Ces deux types de groupements fonctionnels sont reconnus comme étant capables de complexer de nombreux métaux (Tipping, 1998; Gustafsson, 2001; Tipping et al., 2002; Ritchie and Perdue, 2003). Buschmann et al. (2006) proposent que la complexation de l'As(III) sur les groupements phénoliques (sites forts mais moins abondants) peut se faire par perte d'un des OH^- de l'$As(OH)_3$ (Figure I.8). Les groupements carboxyliques, plus abondants mais moins réactifs, ne peuvent vraisemblablement pas entraîner la perte d'un groupement OH^- mais, la présence d'un oxygène (C=O) dans l'environnement de l'As peut stabiliser le complexe par la formation d'une liaison hydrogène (Figure I.9).

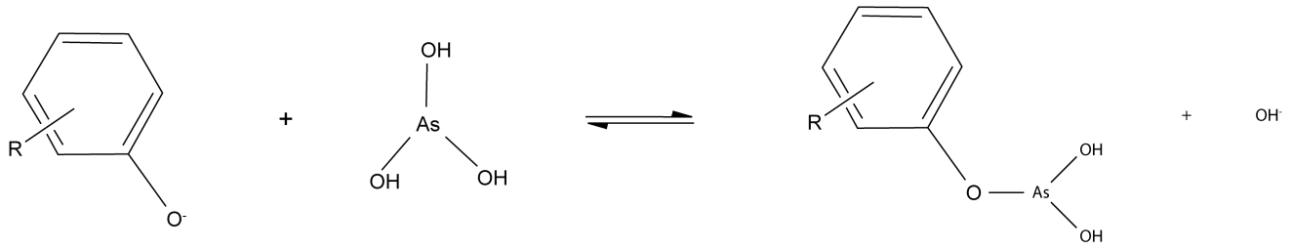

Figure I. 8 Complexation de l'As(III) sur un groupement phénolique de la MO (Buschmann et al. 2006).

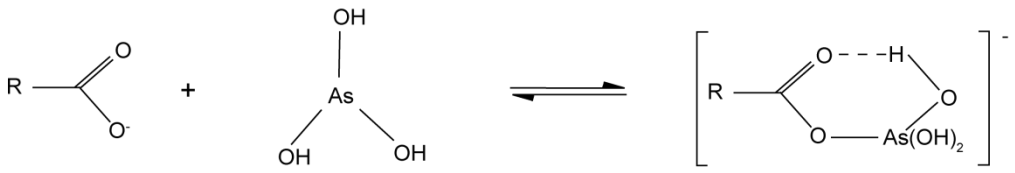

Figure I. 9 Complexation de l'As(III) sur un groupement carboxylique de la MO (Buschmann et al. 2006).

L'As(III), sous sa forme $As(OH)_3$, aurait également la capacité de se complexer aux sites thiols (SH) présents à la surface de la MO naturelle (Langner et al., 2011; Hoffmann et al., 2012). L'$As(OH)_3$ se lie au soufre et perd un ou plusieurs groupements OH^- en fonction de la denticité du complexe. Ces derniers

forment une ou plusieurs molécule(s) H_2O avec le H^+ des groupements SH de la MO (Shen et al., 2013; Catrouillet et al., 2016) (Figure I.10). De tels complexes ont été observés dans des tourbières enrichies en As, telle que la tourbière de Gola di Lago en Suisse (Hoffmann et al., 2013). Dans ces environnements naturellement très riches en As, les êtres vivants (bactéries ou végétaux), s'adaptent en développant des systèmes de détoxification ou de protection. L'As peut se lier sous forme de complexes tridentates sur des acides aminés (de type cystéine) des protéines et des peptides (Shen et al., 2013). La biomasse produite est donc riche en As. Une fois, cette biomasse transformée, par exemple en tourbe, il semblerait que les complexes formés soient conservés. Ce genre de complexation est cependant observé dans des environnements très enrichis en soufre où les conditions anoxiques sont permanentes sur la très grande majorité de la hauteur de tourbe. Cependant, Catrouillet et al. (2015) et Langner et al., (2011) ont montré que les acides humiques en fonction de leur teneur en sites thiols SH pouvaient également former des complexes monodentate avec l'As(III) (Figure I.10). Si les teneurs en Fe sont faibles et ne permettent pas la formation d'oxydes, ce type de complexes semble d'ailleurs favorisé (Catrouillet et al., 2016; Langner et al., 2011).

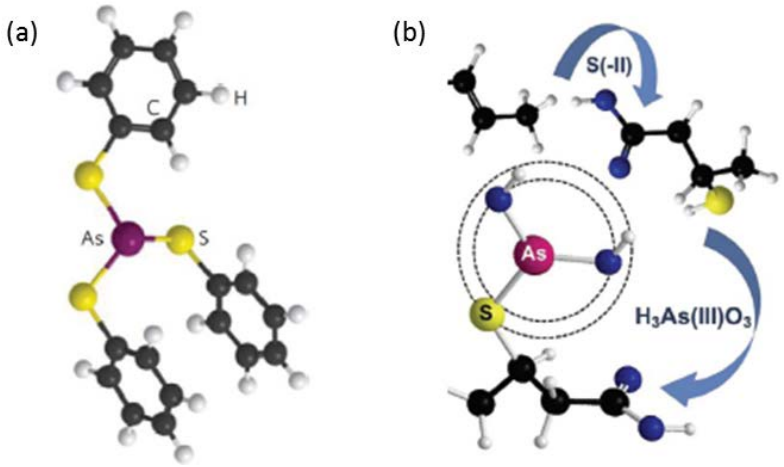

Figure I. 10 Complexation de l'As par (a) trois groupements thiols ou (b) un groupement thiol de la MO (Langner et al., 2011)

L'As(V) étant chargé négativement en solution lorsque le pH est supérieur à 2, la complexation entre l'As(V) et la MO (chargée négativement) semble être encore moins favorable qu'avec l'As(III). Cependant,

Buschmann et al. (2006) ont montré qu'une complexation était possible et même en proportion plus importante que pour l'As(III). L'explication avancée par ces auteurs est la présence d'une charge formelle au centre de l'As(V) (Figure I.11) et/ou une chélation additionnelle ayant un effet de stabilisation.

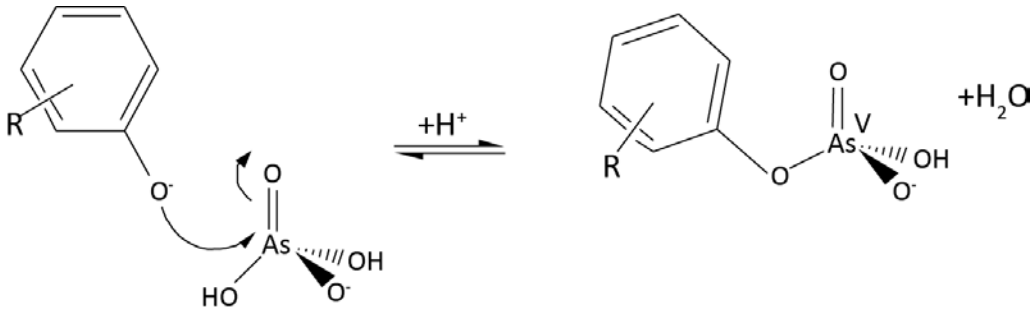

Figure I. 11 Exemple de complexation de l'As(V) sur un groupement phénolique de la MO (Buschmann et al. 2006). L'ajout d'un phénol sur l'arséniate, dont la charge formelle est +V, entraîne la déprotonation puis la libération d'une molécule d'eau.

I.3.1.2 Les formes organiques de l'arsenic

Comme l'azote et le phosphore, l'As possède de nombreuses formes organiques dans laquelle il se lie à des ligands organiques avec des géométries variables. Ces espèces sont retrouvées dans l'environnement via des processus de biométhylation ou d'autres voies biosynthétiques (Cullen and Reimer, 1989). Les espèces les plus courantes de l'As organique sont les formes méthylées (i.e. DMA, MMA) où les groupements hydroxyles (-OH) de l'As(III) ou de l'As(V) sont remplacés par des groupements méthyles ($-CH_3$) (Figure I.3). Un ou plusieurs des groupements hydroxyles ou méthyles peuvent également être remplacés par d'autres ligands ou composés organiques tels que des sucres, des lipides ou des groupements cycliques pour former des composés organiques plus complexes (e.g. arsénobétaine, arsénocholine, arséno-sucre, etc.). Ces derniers ont été largement observés dans des animaux marins mais également dans des organismes terrestres tels que des petits invertébrés et plantes (Dembitsky and Rezanka, 2003; Geiszinger et al., 2002, 1998; Stolpe and Hassellöv, 2007) et dans les sols (Pongratz, 1998; Huang et al., 2007). Ces composés plus complexes (arséno-lipide et arséno-sucres) sont connus pour être des produits finaux de processus de détoxification de l'As par des micro-organismes et des invertébrés (Dembitsky and Rezanka, 2003; Francesconi and Kuehnelt, 2002). Les différentes étapes de ces processus seraient une réduction de

l'As(V) inorganique en As(III) puis un transfert enzymatique d'un groupement méthyle d'un atome donneur à l'As(III) inorganique.

I.3.2 Arsenic et fer

Les oxydes de Fe jouent un rôle majeur dans le cycle biogéochimique de l'As. Ils constituent un système de piégeage efficace de l'As dans de nombreux environnements comme les sédiments (Belzile et al., 1989) et les sols (Morin et al., 2002; Cancès et al., 2005). Les oxydes de Fe hydratés (HFO), comme la ferrihydrite, sont les composants du sol les plus réactifs vis-à-vis de l'adsorption de l'As(III, V) (Goldberg, 2002; Wilkie and Hering, 1996). L'adsorption de l'As(III, V) par les oxydes de fer(III) est très largement documentée (Waychunas et al., 1993; Manceau, 1995; Wilkie and Hering, 1996; Ona-Nguema et al., 2005; Foster and Kim, 2014; Morin et al., 2002; Manning et al., 2002; Fendorf et al., 1997). L'As(III, V) forme des complexes de sphère interne avec la surface des oxydes dont le type varie en fonction de l'état d'oxydation de l'As et du type d'oxyde.

Les modes de complexation de l'As(III) sur quatre phases minérales différentes (goethite, ferrihydrite, lépidocrocite et hématite) ont été mis en évidence par Ona-Nguema et al. (2005) (Figure I.12). En utilisant la spectroscopie d'absorption des rayons X (RX), ils ont montré que l'As(III) forme des complexes bidentates mononucléaires sur une arête d'un octaèdre de Fe, appelé « edge-sharing » (^{2}E), uniquement pour l'hématite et la ferrihydrite (Figure I.12a,c). La distance interatomique entre le Fe et l'As(III) pour ce complexe est d'environ 2.9 Å. Un deuxième complexe entre l'As(III) et le Fe à une distance plus longue est possible, et ce, pour les quatre oxydes de Fe(III) considérés. L'As(III) se lie cette fois-ci en bidentate binucléaire à deux sommets de deux octaèdres dont une arête est commune, ces complexes sont appelés « corner-sharing » (^{2}C). La distance entre l'As(III) et le Fe est de 3.3-3.4 Å. Un troisième complexe, se traduisant par une contribution mineure dans les spectres EXAFS, peut aussi exister à une distance As-Fe de 3.5-3.6 Å. Dans ce complexe, l'As(III) se lie sur un sommet en monodentate mononucléaire (^{1}V) dans la structure de la lépidocrocite et de la goethite (Figure 12.b,d). Cependant, ce complexe est thermodynamiquement et cinétiquement moins favorable que le ^{2}C, ce qui explique sa faible contribution, et n'a pu être observé que dans les cas de faible recouvrement de surface pour la goethite (Manning et al.,

2002; Ona-Nguema et al., 2005) et la lépidocrocite (Ona-Nguema et al., 2005). D'autre études (Farquhar et al., 2002; Manning et al., 2002) ont montré que l'As(III) pouvait également s'adsorber en complexe ^{2}E, en plus des ^{2}C, sur la lépidocrocite en fonction des taux de recouvrement de surface. En effet, à très faibles ratios As/Fe, les complexes ^{2}E seront favorisés par rapport aux ^{2}C. Dans la lépidocrocite, comme dans la goethite, le nombre de sites disponibles pour l'adsorption sur des arêtes (^{2}E) est limité par rapport à ceux situés en sommets (^{2}C). Ainsi, lorsque le recouvrement de surface augmente, les sites en ^{2}E sont saturés rapidement et sont masqués par les ^{2}C (Ona-Nguema et al., 2005). Concernant la ferrihydrite, le nombre de complexes en ^{2}C est toujours supérieur aux complexes en ^{2}E, et ce, quel que soit le recouvrement de surface. Ceci s'explique par la présence des lacunes d'octaèdres de Fe dans la ferrihydrite

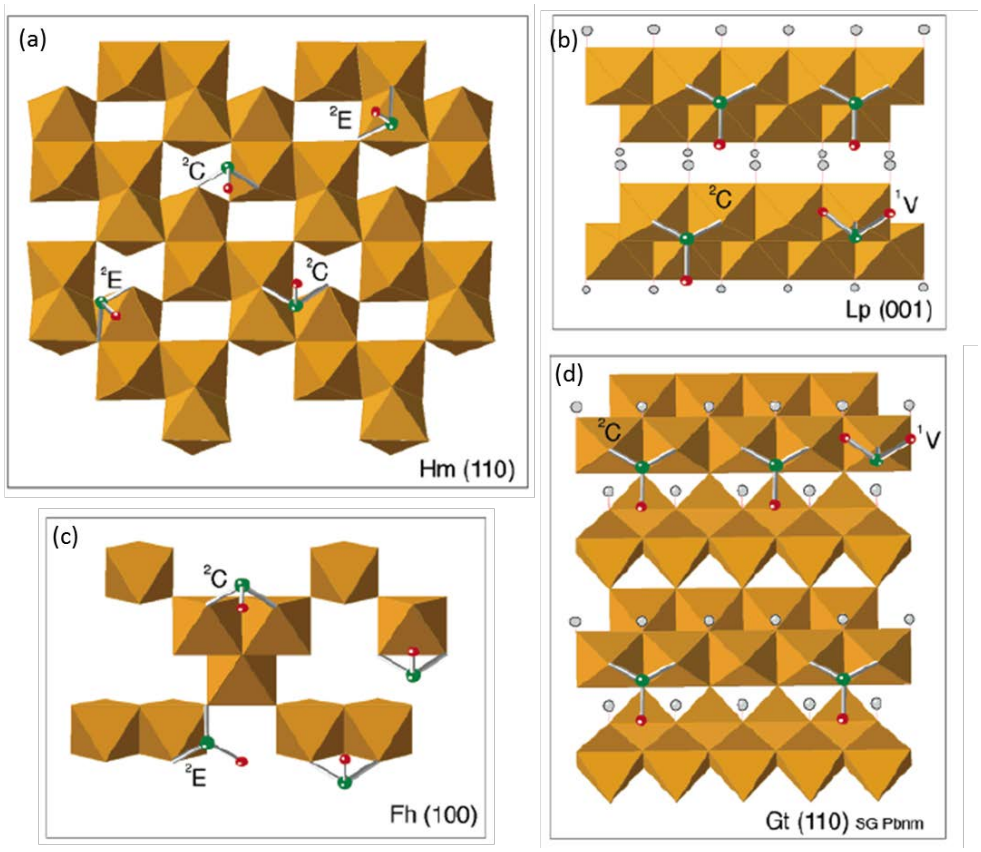

Figure I. 12 Modèles structuraux de l'adsorption de l'As(III) sur (a) l'hématite (Hm), (b) la lépidocrocite (Lp), (c) la ferrihydrite (Fh) et (d) la goethite (Gt) (Ona-Nguema et al., 2005). L'As(III) peut se lier en bidentate mononucléaire (^{2}E), en bidentate binucléaire (^{2}C) et en monodentate mononucléaire (^{1}V).

Durant plusieurs années, la controverse a persisté pour la complexation de l'As(V) sur les oxydes de Fe. Plusieurs auteurs, tels que Fendorf et al. (1997) et Waychunas et al. (1993) ont considéré la formation de 2 complexes : l'un à une distance As(V)-Fe de 2.85 Å attribuée à un complexe en « edge-sharing » (^{2}E) et l'autre à une distance à 3.24 Å attribuée à un complexe en « corner-sharing » (^{2}C). Cependant, des études récentes ont montré que la distance correspondant à un complexe ^{2}E, était en réalité un signal de diffusion multiple (Manning et al., 2002; Sherman and Randall, 2003). Ainsi, l'As(V) ne peut se lier sur les oxydes de Fe que via deux sommets de deux octaèdres adjacents. Une complexation en monodentate ^{1}V à une distance As(V)-Fe de 3.60 Å a été envisagée (Waychunas et al., 1993) mais écartée par Manceau (1995) qui l'a attribuée à un décalage de phase. La distance entre l'As(V) et le Fe adsorbant varie légèrement en fonction de l'oxyde considéré. Manning et al. (2002) ont obtenu des distances de 3.36 Å, 3.34 Å et 3.38 Å pour la goethite, la lépidocrocite et la maghémite, respectivement. Morin et al. (2002) ont étudié l'adsorption de l'As sur de la pharmacosidérite (un arséniate de Fe secondaire) et ont mis en évidence une distance As(V)-Fe de 3.26 Å.

I.3.3 Fer et matière organique

De nombreux auteurs ont montré que la MO était capable de complexer le Fe (Pokrovsky et al., 2005; Dahlqvist et al., 2007; Karlsson and Persson, 2010; Elisabeth Neubauer et al., 2013a). Cette complexation par la MO contrôle la polymérisation des oxydes de fer en inhibant leur croissance (Cornell and Schwertmann, 2003; Pédrot et al., 2011a). Ainsi dans un environnement riche en MO, les oxydes de Fe particulaires sont peu nombreux voire inexistants. Le Fe(III) peut être présent sous trois formes : des nano-oxydes, des petits clusters ou des monomères de Fe liés à la MO. Ces petits agrégats de taille colloïdale ont été identifiés dans plusieurs types d'environnements comme dans les zones humides, formés lors des cycles rédox (Pokrovsky et al., 2005; Dahlqvist et al., 2007; Pédrot et al., 2011a) ou lors du dégel du permafrost (Pokrovsky et al., 2011), dans les sol hawaïens (Thompson et al., 2006) ou dans le fleuve amazone (Allard et al., 2004). La proportion de chaque phase de Fe varie en fonction du pH et du ratio Fe/MO (Buffle et al., 1998; Mikutta and Kretzschmar, 2011; Karlsson and Persson, 2012). Ainsi, Karlsson and Persson (2012) en étudiant l'hydrolyse du Fe(III) en solution en présence d'acide humique, ont montré qu'à faible

concentration de Fe (5-10 mg g^{-1}) et dans une gamme de pH de 3.0-7.2, les complexes de Fe(III) mononucléaire-MO étaient majoritaires et formaient des structures penta-chélatées en anneau. Pour de plus fortes concentrations en Fe (environ 50 mg g^{-1}) et à pH 4.2-6.9, ils ont montré qu'à la première phase monomérique de Fe s'ajoutaient des oxydes de Fe polymériques dont la proportion augmentait avec le pH.

En complément de ces preuves spectroscopiques, des agrégats organo-minéraux colloïdaux ont également été détectés directement sur le terrain par des techniques de filtration couplées à des analyses chimiques par ICP-MS ou par SEC-ICP-MS (Guo et al., 2011; Elisabeth Neubauer et al., 2013a; Majumder et al., 2014; Regelink et al., 2014).

I.3.4 Arsenic, fer et matière organique

La présence de cations métalliques comme le Fe sous forme Fe(III) ionique ou d'oxydes augmente la complexation de l'As(III, V) par la MO. En effet, Redman et al. (2002) et Bauer et Blodau (2006) ont montré que la concentration en As(V) complexé à la MO était fonction de la concentration en Fe. Dans ces associations, le Fe joue le rôle de pont entre la MO et l'As, soit sous forme ionique, de cluster ou d'oxydes de Fe formant ainsi des complexes ternaires (Ritter et al., 2006; Mikutta and Kretzschmar, 2011). Mikutta et Kretzschmar (2011) ont réalisé une expérience de complexation entre de l'As(V), la MO (acides humiques et fulviques) et le Fe(III). Ils ont montré que 25 à 70% de l'As(V) se lient via des complexes de sphère interne au Fe(III) dont 70% sont sous forme Fe(III)-MO, prouvant ainsi l'existence de complexes ternaires. Dans ces complexes, l'As(V) est complexé sous forme de bidentates binucléaires sur deux sommets de deux octaèdres voisins (Figure I.13a); ce qui est en accord avec les données spectroscopiques de complexation de l'As(V) sur des oxyhydroxides de Fe(III). Des complexes mononucléaires stabilisés par une liaison hydrogène avec un groupe OH d'un octaèdre de Fe adjacent ont également été observés dans ces échantillons, comme ils avaient été proposé pour la complexation de l'As(V) sur la goethite (Fendorf et al., 1997; Waychunas et al., 1993) (Figure I.13b).

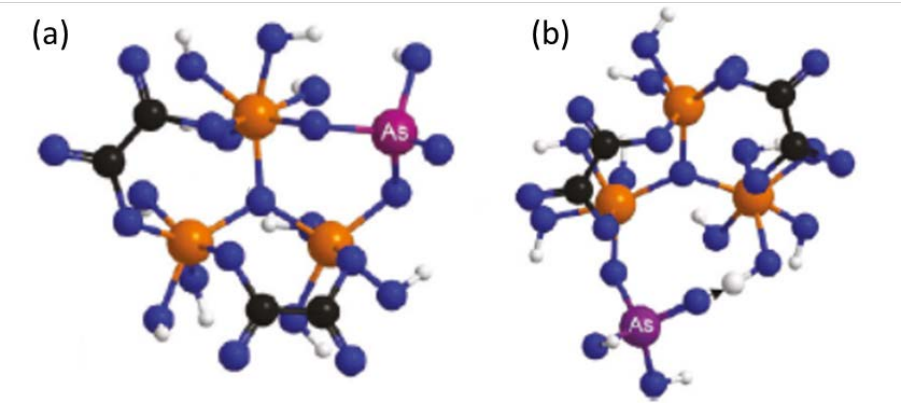

Figure I. 13 Représentation schématique des complexes ternaires entre l'As(V) (violet), Fe(III) (orange) et des ligands organiques (noirs). L'As(V) se lie au Fe en bidentate binucléaire ^{2}C (a) et, en faible quantité, en monodendate monucléaire 1V (b) (Hoffman et al., 2013).

Des études de terrain ont permis de mettre en évidence la présence de complexes ternaires entre le Fe, l'As et la MO dans des cours d'eau boréals riches en MO (Elisabeth Neubauer et al., 2013a). Les auteurs ont utilisé la technique de fractionnement d'écoulement de champs (FlowFFF) pour étudier les associations entre les éléments. Ils ont mis en évidence qu'entre 70 et 75 % de l'As était associé à la MO dans la fraction comprise entre 1 kDa et 0.2 µm, ce qui est très supérieur aux valeurs avancées par Buschmann et al. (2006) pour une simple adsorption As-MO. Ils ont interprété ces résultats par la formation de complexes ternaires par des ponts cationiques de Fe.

Plusieurs études ont montré que la complexation de l'As(III) sous forme de complexes ternaires As-Fe-MO était possible. Hoffmann et al. (2013) ont montré que l'As(III) était capable de former des complexes ternaires avec de la tourbe via du Fe(III) sous forme ionique. L'As(III) y est complexé sous forme de complexes bidentates mononucléaires avec le Fe(III) pour de faibles concentrations en Fe(III) (Figure I.14a) et de bidentates mononucléaires et bidentates binucléaires pour de fortes concentrations en Fe(III) (Figure I.14b). Ils ont cependant calculé que les constantes de stabilité de ces complexes étaient plus faibles que celles des complexes formés entre l'As(III) et les sites thiols de la même tourbe. Catrouillet et al. (2016) ont cependant montrés que pour un rapport Fe/MO proches de celui de Hoffmann et al. (2013) mais des concentrations en Fe et MO correspondant à des conditions naturelles (très inférieures à celles requises par

la spectroscopie), la présence de Fe(III) ne favorisait pas la sorption de l'As(III) qui était préférentiellement adsorbé sur les sites thiols de la MO.

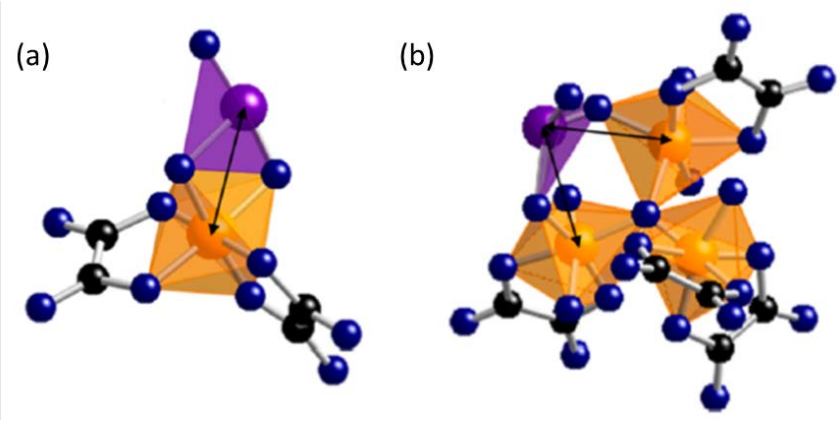

Figure I. 14 Représentation schématique de complexes ternaires entre As(III) (violet), Fe(III) (orange) et des ligands organiques (noirs). L'As(III) se lie au Fe en (a) bidentate mononucléaire ou en (b) bidentate binucléaire (Hoffmann et al., 2013).

Par voix analytique, à l'aide d'un couplage SEC (chromatographie d'exclusion stérique)-UV-ICP-MS, Liu et al. (2011) ont mis en évidence l'existence de complexes ternaires entre l'As(III), le Fe(III), probablement sous forme de ferrihydrite, et la MO (Figure I.15).

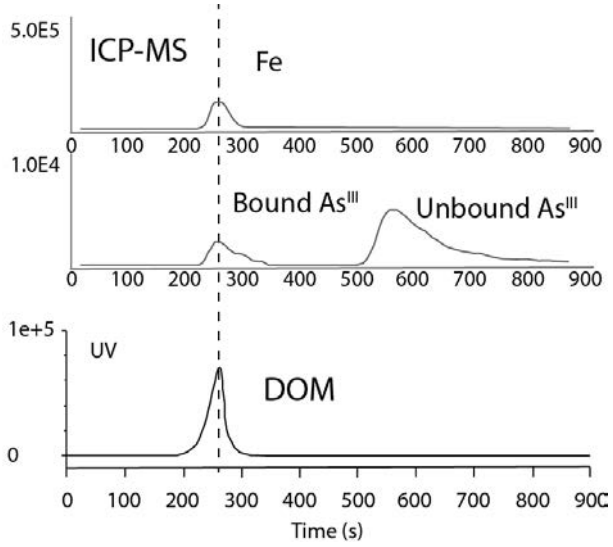

Figure I. 15 Co-élution de l'As(III), du Fe et de la MO par technique de SEC-UV-ICP-MS, mettant en évidence la formation de complexes ternaires (Liu et al., 2011).

Dans un environnement riche en MO et en Fe comme le sont les zones humides, la formation d'agrégats organo-minéraux semble avoir une importance capitale dans l'adsorption et donc dans la mobilité de l'As. L'étude de ces composés parait donc essentielle pour mieux appréhender le devenir de l'As dans les zones humides.

I.4 Objectifs de la thèse

Considérant l'ampleur de la pollution en As dans le monde et son impact sur la santé humaine, il est important de mieux comprendre les processus responsables de sa dynamique, notamment dans les zones riches en MO et en fer comme les ZH. Comme la biodisponibilité et la toxicité de l'As dépendent de sa spéciation, il apparaît essentiel d'identifier les phases porteuses de l'As ainsi que les interactions entre le Fe, la MO et l'As. La contamination en As via les zones humides ripariennes a été très peu étudiée alors que ces zones occupent une place stratégique dans le paysage et vis-à-vis des échanges avec les rivières et les nappes d'eau souterraines.

L'objectif de ce travail de thèse a donc été de mieux comprendre le comportement de l'As vis-à-vis de la MO et du Fe dans un environnement soumis à des variations d'oxydoréduction périodiques afin de répondre à plusieurs questionnements tels que l'impact de la réoxydation, produite par la baisse du niveau de l'eau dans la ZH, sur la mobilité de l'As, la nature et la pérennité des produits de réoxydation piégeurs de l'As et enfin le rôle de piège ou de source d'As des zones humides.

Pour répondre à cette problématique de recherche, trois volets ont été abordés :

- **La compréhension du rôle de la MO sur l'oxydation de l'As et la nature des phases potentiellement porteuses d'As.**

L'objectif de cette partie a été d'identifier le contrôle exercé par la MO sur la spéciation de l'As et sur la nature des solides formés, potentiellement piégeurs d'As lors de la période de réoxydation d'une zone humide. Dans cette partie, nous avons analysé des produits de réoxydation, collectés directement dans un sol d'une zone humide. La spéciation de l'As et du Fe a été étudiée par micro-spectroscopie d'absorption des rayons-X (XAS).

- **L'étude de la variabilité de la spéciation de l'As dans les produits d'oxydation d'une solution de sol de ZH.**

Les produits de réoxydation solides prélevés sur le terrain sont issus d'une suspension de colloïdes et/ou particules qui via les processus d'évaporation et de baisse du niveau de la nappe peuvent se déposer dans la porosité du sol. Pour mieux appréhender les processus de piégeage et la spéciation de l'As dans les zones humides, il est donc essentiel d'étudier en détails ces colloïdes et ou particules avant leur agglomération et/ou dépôt. Pour cela, nous avons réalisé un fractionnement en taille et poids moléculaire d'une suspension de sol produite par réoxydation d'une solution d'incubation anaérobie de sol de zone humide. Dans chaque fraction, la spéciation de l'As et du Fe ainsi que la composition de la MO ont été caractérisées via des techniques de spectroscopie et de couplages chromatographiques.

- **La détermination de l'influence de la structure des agrégats Fe-MO sur l'adsorption de l'As.**

Que ce soit dans la littérature ou dans ce travail de thèse, les associations colloïdales (ou petits agrégats) Fe-MO semblent être des acteurs majeurs de contrôle de la mobilité de l'As. Or, l'organisation entre le Fe et la MO et la structure de ces associations, via par exemple, la variation de la surface spécifique ou la densité de sites de complexation, peuvent influencer les processus de piégeage de l'As. Dans cette partie, en utilisant l'expérimentation (synthèse d'agrégats modèles et expérience d'adsorption) couplée à la diffusion de neutrons et de rayons-X aux petits angles couplées à l'absorption des rayons-X, je me suis efforcée de mieux appréhender les relations entre structure et capacité d'adsorption de ces associations colloïdales Fe-MO vis-à-vis de l'As.

Enfin, une partie conclusion clôt ce manuscrit. Les principaux résultats y sont repris et mis en perspectives vis-à-vis de la dynamique de l'As dans les zones humides.

Chapitre II. Contrôle de la matière organique sur l'oxydation de l'As par les oxydes de fer dans les zones humides ripariennes

Ce chapitre correspond à un article publié dans la revue "Chemical Geology": Evidence of organic matter control on As oxidation by iron oxides in riparian wetlands, Hélène Guénet, Mélanie Davranche, Delphine Vantelon, Mathieu Pédrot, Maya Al-Sid-Cheikh, Aline Dia, Jacques Jestin (Chemical Geology, Elsevier, 2016, 439, pp 161-172, doi:10.1016/j.chemgeo.2016.06.023)

Evidence of organic matter control on As oxidation by iron oxides in riparian wetlands

RESUME

Les zones humides bordant les rivières et les fleuves connaissent des variations importantes de leur régime hydrologique. Elles peuvent être saturées en eaux en période de hautes eaux ou désaturées voir asséchées en période de basses eaux. La saturation en eaux des sols de zones humides induit la mise en place de conditions réductrices à l'origine de la dissolution réductrice des oxyhydroxides de Fe(III) du sol et des éléments qui leur sont associés. Lorsque le niveau de l'eau diminue, les sols de zones humides sont progressivement réoxydés et le Fe précipite piégeant potentiellement un certain nombre d'éléments chimiques. L'arsenic fait partie du groupe des éléments dont le cycle biogéochimique est fortement associé à celui du Fe. Or, si l'impact des conditions réductrices sur la mobilité de l'As dans les zones humides est bien compris et documenté, il existe un manque important d'informations sur son comportement en période d'oxydation.

Nous avons donc étudié la spéciation de l'As dans les produits d'oxydation collectés dans un sol de zone humide (Naizin-Kervidy, France). Les solides oxydés ont été étudiés par analyses géochimiques, NanoSIMS et par spectroscopie d'absorption des Rayons X (XAS) au seuil K du Fe et de l'As. Les analyses ont

montré qu'ils étaient enrichis en carbone organique (CO), Fe et As par rapport au sol et à la solution du sol. L'analyse NanoSIMS a montré une colocalisation de l'As et du Fe, mais aussi révélée la présence de 'hotspots' d'As où l'As est soit colocalisé avec le Fe soit colocalisé avec le CO. L'analyse XAS par le biais de 'linear combinaison fitting' (LCF) de spectres XANES au seuil K de l'As ont montré que l'As était partiellement oxydé (65 à 100% d'As (V), selon les points d'analyse). L'extrapolation des spectres EXAFS a montré que l'As formait avec le Fe des complexes bidendates mononucléaires 2E (distance As-Fe = 2,74 à 2,95 Å) et binucléaires 2C (distance As-Fe = 3.28-3.43 Å). La persistance de l'As(III) a été expliquée par le contrôle exercé par la MO sur les phases porteuses de l'As qui sont, dans ce système, responsables de son oxydation. Les fortes concentrations en MO contraignent la formation de nano-lépidocrocite piégée dans la matrice organique et de petits polymères, voire de monomères de Fe, complexés aux molécules organiques. La taille nanométrique des particules de Fe et la présence de polymères de Fe conduisent à une augmentation de la complexation de l'As sous forme de complexes bidentates mononucléaires 2F par rapport aux complexes binucléaires 2C dont les sites ont été identifiés comme étant les sites actifs dans l'oxydation de l'As(III). Dans les zones humides, la nature et la structure des produits d'oxydation riches en Fe sont donc fortement contraintes par la MO qui limite indirectement la réoxydation de l'As(III) et promeut ainsi sa persistance dans les sols.

ABSTRACT

Soils in riparian wetlands are periodically flooded, resulting in the establishment of reducing conditions and the solubilization of As, subsequently to the reductive dissolution of Fe(III)-oxyhydroxides. When the water level decreases, the wetlands are reoxidized. However, although the behavior of As under the reducing period is well documented, there is a lack of information regarding its behavior during the oxidizing period.

In this study, we investigated As speciation in oxidation products from an initially reduced wetland soil solution recovered from the Naizin-Kervidy riparian wetland (France). The oxidation products were studied using NanoSIMS analysis and synchrotron X-ray techniques. These products were enriched in organic

carbon, Fe and As compared with the soil and soil solution. The NanoSIMS analysis showed a colocalization of As and Fe but also revealed the presence of As hotspots where As was either associated with Fe or organic matter (OM). X-ray absorption spectroscopy (XAS) showed that As was sorbed to Fe(III)-oxyhydroxides. The linear combination fitting (LCF) of the As K-edge XANES revealed that As was not totally oxidized (i.e. between 65 and 100% of As(V)). Shell-by-shell fits of the As K-edge EXAFS showed that As formed binuclear edge-sharing ^{2}E (R_{As-Fe} = 2.74-2.95 Å) and corner-sharing ^{2}C (R_{As-Fe} = 3.28-3.43 Å) complexes with Fe.

In addition to study of natural samples, oxidized reference samples were analyzed and demonstrated the role of OM on As speciation. The persistence of As(III) was explained by OM control on the As carrying phase during the oxidation, via the formation of nano-lepidocrocite and small Fe-clusters bound to OM. The small size of the Fe phase led to an increased capacity for As adsorption and an increase in ^{2}E sites compared to ^{2}C active sites for As(III) oxidation.

II.1 Introduction

Among wetlands, riparian wetlands are of major importance for contaminant (organics, metals, metalloids, etc.) mobility in the environment. In wetlands during high water levels, reducing conditions are established and favor the reductive dissolution of Fe(III)-oxyhydroxides. The biogeochemical cycle of arsenic is strongly dependent on Fe(III)-oxyhydroxides. Their reductive dissolution leads to the release of As(V) along with Fe(II) and organic matter (OM) in the solution (Davranche et al., 2011; Dia et al., 2015; Grybos et al., 2009, 2007; Olivié-Lauquet et al., 2001). Following its solubilization, As(V) is reduced to As(III), generally by autochthonous bacteria (through detoxification or metabolism processes; Dia et al., 2015). Recent studies have shown that, under such reducing conditions, As(III) might be bound to colloidal or particulate OM via thiol (-SH) groups and/or form ternary complexes, OM-Fe(II)-As, with Fe(II) as cationic bridges (Langner et al., 2011; Mikutta and Kretzschmar, 2011, Catrouillet et al., 2014). In the Mekong flood plain (Cambodia), several studies have demonstrated that subsequently to its release and reduction, As(III) is mobile and contaminates the underlying groundwater; these wetlands are thus considered to be a source of As (Fendorf, 2010; Kocar et al., 2008; Polizzotto et al., 2008). However, in riparian wetlands, when the water

level decreases, consequently to the decrease in the precipitation volumes and increase in evaporation, the redox conditions become progressively oxidative, and the fate and behavior of As(III) can be questioned. Two possible mechanisms may occur: either As remains bound to OM via thiol groups or metallic bridges or is bound to the newly formed particulate or colloidal Fe(III) minerals. Its oxidation state must be questioned as well; As(III) could be completely or only partially oxidized as As(V). However, few studies have been performed on oxidation products derived from the wetland soil solution to understand their impact on the As speciation. ThomasArrigo et al. (2014) investigated oxidation products from a peatland surface solution. They revealed that As was adsorbed onto poorly crystalline Fe(III)-oxyhydroxides as As(V) and As(III). They linked the presence of As(III) to the reduction of As(V) by freshwater green algae present in the Fe(III)-oxyhydroxides flocs. Peatlands and riparian wetlands have different water regimes. Peatlands are generally permanently flooded (i.e. reducing condition) while riparian wetlands are subjected to seasonal flooding (i.e. alternating redox). These discrepancies are of major importance in terms of the OM qualities (i.e. mostly humate for riparian wetlands versus fulvate for peatlands) and properties, mineral reduction/oxidation rates, element fluxes, etc. Al-Sid-Cheikh et al. (2015) showed that oxidation products from riparian wetlands are Fe- and organic-rich and are able to concentrate high amounts of As. Through the statistical treatment of NanoSims images and XANES records, they revealed that the As distribution was correlated to the Fe distribution and they highlighted the presence of hot spots highly enriched in As, OM and S but depleted in Fe. They suggested possible interactions between OM, As and S via OM thiol groups. Because the NanoSIMS analysis only shows colocalizations of the elements, detailed spectroscopic investigations are needed to infer the oxidation state and the local coordination environment of As. Because the amount of OM is high in reoxidation compounds (Al-Sid-Cheikh et al., 2015), it should influence the Fe(III)-oxyhydroxide structure and the As oxidation state and speciation.

The purpose of this study was thus dedicated to identify the fate of As when the riparian wetland became oxidized, namely to identify the distribution of the As speciation in oxidation compounds from a naturally poorly As-enriched riparian wetland (Naizin-Kervidy, France). *In-situ* scavenging devices were used to collect the oxidation products subsequent to the water level decrease in the wetland soil (Al-Sid-Cheikh et

al., 2015; Belzile et al., 1989). The bulk and microscale distribution and speciation of As and Fe were investigated by coupling NanoSIMS to XAS experiments (μXANES and μEXAFS).

II.2 Experimental Method

II.2.1 Field site description and sample collection

Natural samples were recovered from the Mercy riparian wetland of Kervidy-Naizin located in Brittany in western France at 48°00'42.4'' N and -2°50'20.2'' E (decimal degrees). This sub-catchment has been monitored since 1991 to investigate the effects of intensive agriculture (corn culture and livestock) on water quality. The hydrological, pedological and geochemical contexts are therefore well documented (Bourrié et al., 1999; Dia et al., 2000; Gruau et al., 2004; Olivié-Lauquet et al., 2001). The maritime temperate climate is characterized by an annual temperature and precipitation of 10.7 °C and 814 mm $days^{-1}$, respectively. The adjacent stream is ephemeral and does not often flow from the end of August to October. The upper soil horizon was defined as the organo-mineral horizon (Ah) of a planosol (according to the WRB international classification) which contained (wt%; anhydrous basis) OM (15%), clay (42%), quartz (30%) and Fe(III)-oxyhydroxides (3.5%) (Grybos et al., 2007). The samples were collected using the method described in Al-Sid-Cheikh et al. (2015) with a collecting device inspired from Belzile et al. (1989). Polytetrafluoroethylene (PTFE) sheets (10 x 18 cm, 1.5-mm-thick), wrapped in nylon filters for protection (size pore, 67μm), were inserted into the upper horizon of the wetland soil during the water-saturation period (i.e. when the soil solution was reduced). This material was selected because of its inert characteristic and resistance toward aging (Belzile et al., 1989; Teasdale et al., 1998). Under these reducing conditions, soil Fe(III)-oxyhydroxides were reductively dissolved by autochthonous bacteria in the soil (Dia et al., 2015), which subsequently induced the solubilization of a large amount of Fe(II) and other elements, primarily associated with the Fe(III)-oxyhydroxides, such as metals or metalloids. The increase in pH due to H^+ consumption by the reductive reactions induced the desorption of a large amount of OM from the mineral surfaces (Grybos et al., 2009). The PTFE sheets were inserted under these reduced conditions. When the water table decreased, the soil was progressively water-desaturated. All of the redox-sensitive elements of the reduced soil solution

were potentially oxidized, especially Fe(II) which precipitates in the presence of elevated level of OM to produce Fe(III)-OM solids (Al-Sid-Cheikh et al., 2015; Pédrot et al., 2011a). The PTFE sheets mimicked the hydrophobic soil porosity and the oxidation compounds therefore coated their surface. The sheet scavenger method was validated by Al-Sid-Cheikh et al. (2015), who clearly demonstrated that the coated compounds originated from the soil solution. The precipitates on the PTFE device showed an identical rare earth elements (REE) pattern with the wetland soil solution. The REE are strongly adsorbed on OM and Fe(III)oxyhydroxides and allow these compounds to be traced in the environment (Davranche et al., 2011; Grybos et al., 2007; Tang and Johannesson, 2003). An identical REE pattern between the reduced soil solution and oxidation products demonstrated that precipitated solids on the PTFE device originated from the oxidation of the reduced soil solution without any selection which would have induced a fractionation of REE and a modification of the REE pattern. Moreover the concentrations of Si and Al (indicating the presence of clays) of the precipitates are low and similar to those in the reduced soil solution (Table II. 2) confirming that the precipitates originated from the soil solution and not from the soil. In the present study, the sheet scavengers were removed from the soil after five hydrological cycles (i.e. five years) which allows us to study the result of all processes occurring during oxidation/reduction cycles in the wetland. Processes including precipitation of diagenetic solids, As adsorption and Fe(III)-oxyhydroxide maturation occurring within the wetland soil are integrated by the sampling method used in this study.

II.2.2 Chemical analyses

The collected soil samples were dried at 30°C for 72 h, and then sieved to 2 mm. The samples were digested by alkaline fusion using lithium metaborate ($LiBO_2$) flux and analyzed for major and trace elements at the SARM facility (Service d'Analyse des Roches et des Minéraux, Nancy, France). Dissolved organic carbon (DOC) concentrations were measured using an organic carbon analyzer (Shimmadzu TOC-V CSH). The accuracy of the DOC measurements was estimated to be at ± 5% by using a standard solution of potassium

hydrogen phthalate. The iron and As concentrations were determined by ICP-MS using an Agilent technologies 7700x at the University of Rennes 1. The samples were pre-digested twice with 14.6 N HNO_3 at 90°C, evaporated to complete dryness and then resolubilized with HNO_3 at 0.37 mol L^{-1} to avoid any interference with the DOC during the analysis. A flux of He was injected in a collision cell to remove interferences from $^{40}Ar^{35}Cl/^{75}As$ and $^{40}Ar^{16}O/^{56}Fe$. Quantitative analyses were performed using a conventional external calibration procedure (seven external standard multi-element solutions, Inorganic Venture, USA). Rhodium-rhenium was added on-line as an internal standard at a concentration level of 300 mg L^{-1} to correct for instrumental drift and possible matrix effects. Calibration curves were calculated from the intensity ratios of the internal standard and the analyzed elements. The international geostandard SLRS-4 was used to control the accuracy and reproducibility of the measurement procedure. The instrumental error on the As and Fe analysis was below 3%. The chemical As and Fe blanks were lower than the detection limits (respectively 0.003 and 0.07 µg L^{-1}) and were thus negligible.

II.2.3 NanoSIMS sample preparation and data acquisition

Adhesive carbon tapes were used to recover the coated solid layer from the sheet scavengers. The carbon tapes were analyzed without any other NanoSIMS preparation. Measurements were performed with the Cameca NanoSIMS 50 at the facility at the University of Rennes 1 (France). By using a primary cesium beam (Cs^+; beam current ~15 pA), secondary ions of Fe (as $^{56}Fe^{16}O^-$), carbon (measured as the $^{12}C/^{14}N^-$ ratio to distinguish the carbon of the sample from the one on the scotch tape), and As (as $^{75}As^-$) were sputtered from the sample surface and detected simultaneously (multicollection mode) in electron multipliers at a mass-resolving power of ~4000 (M/ΔM). The primary beam was focused to a spot size of 100 nm and scanned in a raster pattern on the surface sample. The chemical maps were determined by image processing using the ImageJ software (1.38x version) and the NRIMS ImageJ analysis module. The colocalization analyses were performed under JACoP, a plug-in for ImageJ developed by Bolte and Cordelieres (2006). Pearson's coefficient (PC) was calculated to determine the dependency of the pixels in the dual-channel images. PC is a coefficient where 1 and –1 represent a perfect colocalization and perfect exclusion, respectively, and where 0 represents a random colocalization. Manders' coefficients (M1 and M2) were also

used for the colocalization studies and can be used to determine the proportion of overlap of each channel with the other. In this case, 1 represents a perfect colocalization and 0 represents no colocalization (Manders et al., 1993). M1 and M2 are insensitive to the intensity of the overlapping pixels, which is convenient when the intensities in both channels have very different values between them, like between Fe and As.

II.2.4 Reference samples for X-ray absorption spectroscopy

All of the aqueous solutions were prepared with analytical grade Milli-Q water (Millipore). The Fe(II) stock solutions were prepared with iron chloride tetrahydrate ($FeCl_2.4H_2O$) from Acros Organics. The As(III) stock solutions were prepared with a sodium arsenite solution (Na_2AsO_2) from Fluka Analytical. The As(V) stock solution was prepared with arsenate oxide (As_2O_5) from Inorganic Ventures. The synthesis of the organic As-Fe reference compounds was performed at Geosciences Rennes. The OM used was a humic acid (HA) corresponding to Leonardite humic acid (IHSS). The composition of HA was (as a mass fraction): C = 63.81%, O = 31.27%, H = 3.70%, N = 1.23%. The DOC/As and DOC/Fe ratios of the synthesized reference compounds were representative of the natural reduced soil solution ratios from the studied wetland (Dia et al., 2000; Olivié-Lauquet et al., 2001). The anoxic synthesis of the references was performed inside a Jacomex isolator glove box (< 10 mg L^{-1} of O_2). The pH of the references synthesized from humic acid was set to 6.5 and the ionic strength to 5 10^{-3} mol L^{-1} with NaCl as the electrolyte. A summary of the reference materials and their synthesis is presented in Table II. 1 HA-As(III)*oxic* was synthesized inside the glovebox from 30 mL of a 648.7 mg L^{-1} Leonardite suspension to which 0.2 mL of a 83 mg L^{-1} Na_2AsO_2 stock solution was added. The concentration of As was 0.55 mg L^{-1}. The suspension was stirred for 24 hours to allow elemental diffusion and prevent decantation (Catrouillet et al., 2015; Hoffmann et al., 2012), and then oxidized outside the glovebox at room temperature until dryness was obtained (approximately one week before analysis). For HA-Fe-As(III)*oxic*, 638 mg L^{-1} HA suspension was deoxygenated in a Jacomex isolator glove box (< 10 ppm of O_2) for 24 hours. In 50 mL of this suspension, 0.3 mL of a 83 mg L^{-1} Na_2AsO_2 stock solution and 6.7 mL of a 950 mg L^{-1} Fe(II) stock solution were added. The final concentrations of DOC, Fe and As were respectively 562.4, 112.5 and 0.49 mg L^{-1}. The suspension was continuously stirred for 24 hours to

reach equilibrium and then oxidized outside the glove box and dried at room temperature (approximately two weeks before analysis). The obtained powder was subsequently impregnated under high vacuum (800 Mbar) with an epoxy resin (Araldite® 502, Sigma-Aldrich). HA-Fe-As(V)*oxic* was synthesized from 20 mL of a 797 mg L^{-1} Leonardite suspension in which 1.4 mL of a 9.94 mg L^{-1} As(V) stock solution and 2 mL of a 1.38 g L^{-1} Fe(II) stock solution were added. The concentrations of DOC, Fe and As were 680.6, 117.8 and 0.60 mg L^{-1} respectively. The sample was dried at room temperature. Fh-As(III)*oxic* was prepared using the following procedure (Wilkie and Hering, 1996). A 0.1 M KOH stock solution was added dropwise with stirring to 500 mL of 0.05 mol L^{-1} $Fe(NO_3).9H_2O$. The pH reached a value of approximately 8 with the addition of 350 mL of 0.1 M KOH to ensure total Fe hydrolysis (Wilkie and Hering, 1996). A volume of 0.6 mL of a 0.05 M Na_2AsO_2 stock solution was added to obtain the desired concentration of 2 g L^{-1} and 11 mg L^{-1} for Fe and As respectively.

Table II. 1 References used for XAS analysis at the As and Fe K-edge

Sample	Binding method	As/Fe ratio	As/DOC ratio	Reference
As K-edge references				
Fh-As(III)*anoxic*	adsorption	0.012	-	(a)
Fh-As(III)*oxic*	coprecipitation	0.005	-	this study
Fh-As(V)*oxic*	coprecipitation	0.007	-	this study
HA-As(III)*oxic*	coprecipitation	-	$8.5\ 10^{-4}$	this study
HA-Fe-As(V)*oxic*	coprecipitation	0.005	$8.8\ 10^{-4}$	this study
HA-Fe-As(III)*oxic*	coprecipitation	0.004	$8.7\ 10^{-4}$	this study
Fe K-edge references				
Fh-As(V)*oxic*	coprecipitation	0.007	-	this study
Lp-As(V)*oxic*	coprecipitation	0.005	-	(b)
HA-Fe-As(III)*oxic*	coprecipitation	0.004	$8.7\ 10^{-4}$	this study

(a) Ona-Nguema et al, 2005
(b) Dia et al, 2015

The Fh-As(III)*oxic* suspension was aged for at least 24 hours with stirring. Then the suspension was washed three times with deionized water using centrifugation and dialyzed with 12-14 KDa cellulose membrane during 48 hours. The sample was dried at room temperature (approximately two weeks before analysis). Fh-As(V)*oxic* was synthesized with the same protocol as Fh-As(III)*oxic*, using As(V) stock solution, with a target

As/Fe ratio of 0.007. The lepidocrocite sample (Lp-As(V)*oxic*) was synthesized in the presence of As(V) according to the protocol given by Schwertmann and Cornell (1991) with an As/Fe mass ratio of 0.005 and was provided by A. Dia (Dia et al., 2015). The Lp-As(V)*oxic* was confirmed to be lepidocrocite using XRD analyses performed on a Siemens D500 diffractometer at the Chemical Sciences Department at the University of Rennes 1. Fh-As(III)*anoxic* was prepared by the adsorption of As(III) onto 2-line ferrihydrite synthesized according to Schwertmann and Cornell's protocol (1991) with an As/Fe ratio of 0.012. The As K-edge EXAFS spectra were provided by G. Ona-Nguema (Ona-Nguema et al., 2005). All of the obtained powders were pressed into 6 mm pellets for the Fe K-edge XAS analyses.

II.2.5 X-ray Absorption Spectroscopy (XAS)

II.2.5.1 Data collection

Arsenic K-edge spectra were collected on both the I18 beamline (Mosselmans et al., 2009) of the Diamond Light Source (DLS, Didcot, UK) and the 10.3.2 beamline (Marcus et al., 2004) of the Advanced Light Source (ALS, Berkeley, USA). Iron K-edge spectra were recorded on the LUCIA beamline (Flank et al., 2006) of the SOLEIL Synchrotron (SOLEIL, St Aubin, France). The monochromators used were Si(111) crystals. They were calibrated setting the first inflection point of the L-edge absorption spectrum of an Au foil to 11.918 KeV on I18, of a Na_2HAsO_4 standard to 11.875 KeV on 10.3.2 and of the K-edge of an Fe foil to 7.112 KeV on LUCIA. Spectra were collected in fluorescence mode using a 4-element Ge solid state detector on I18, a 7-element Ge solid state detector on 10.3.2 and a 4-element Silicon Drift Diode Detector on LUCIA. The beamsize on the sample was 2 x 3 µm on I18, 6 x 3 µm on 10.3.2 and 3 x 3 µm on LUCIA. To prevent beam-induced redox changes, samples were maintained under vacuum and at 150K using a liquid nitrogen cryostat on I18 and LUCIA. In the natural sample, prior to XAS acquisition, the spatial distribution of the elements in the sample was mapped by micro-X-ray fluorescence (µ-XRF). Based on the resulting maps, different types of spots were selected for the XAS analysis according to their As/Fe ratio as well as the As and Fe content. Fe K-edge XAS reference spectra were collected with a beamsize set to 2 x 2 mm in transmission mode using a silicon diode for Fh-As(V)*oxic* and Lp-As(V)*oxic,* and in fluorescence mode for HA-Fe-As(III)*oxic*.

II.2.5.2 XAS data analysis

Arsenic and Fe XAS spectra were extracted using the Athena software (Ravel and Newville, 2005) including the Autbk algorithm (Rbkb = 1, k-weight = 3). Normalized spectra were obtained by fitting the pre-edge region with a linear function and the post-edge region with a quadratic polynomial function. The Fourier transform of the k^3-weighted EXAFS spectra were calculated over a range of 2-10.5 $Å^{-1}$ for As and 2-11 $Å^{-1}$ for Fe using an Hanning apodization window (window parameter = 1). Back Fourier filters were extracted over the 1.15-3.45 Å (1.15-3.85 Å for HA-Fe-As(III)*oxic*) and 1-3.8 Å R-range for As and Fe, respectively, using the same apodization window shape.

The relative proportions of As(III) and As(V) in the samples were determined by linear combination fitting (LCF) of the XANES spectra within the energy range of 11840-11940 eV using relevant As(III) and As(V) model compounds (i.e. As(III) and As(V) adsorbed onto ferrihydrite, the XANES white line position for As adsorbed on ferrihydrite being identical to that of As adsorbed on lepidocrocite (Ona-Nguema et al., 2005). The weighting factors were forced to be between 0 and 1 and the sum weights were not constrained in order to make sure that the references were suitable. All of the As(V) percents were recalculated to a component sum of 100%.

EXAFS data were analyzed by shell fitting using the software code Artemis (Ravel and Newville, 2005). Theoretical back scattering paths for the fits were calculated from different crystal structures using FEFF6. Scorodite (Kitahama et al., 1975) and tooeleite (Morin et al., 2007) structures were used to extract paths from backscatters of As(V) and As(III), respectively. Goethite (Hazemann et al., 1991), lepidocrocite (Zhukhlistov, 2001) and Fe-carboxylate (Horcajada et al., 2007) structures were used to obtain the backscattering paths for Fe. Shell-fit analyses were performed within the 1.15-3.5 Å and 1.15-3.85 Å R-range for As and 1-3.8 Å for Fe. The best fit was chosen by minimizing the reduced χ^2 which depends on the number of independent parameters, the number of fitted parameters and the uncertainty of the data points. For As, the addition of multiple scattering tends to improve the quality of the fit (Morin et al., 2002; Voegelin et al., 2007). Here, the triangular As-O-O (MS1, degeneracy = 12), the collinear As-O-As-O (MS2 degeneracy = 4) and the non-collinear As-O-As-O (MS3, degeneracy = 12) paths were added for the fit of the $As^{(V)}O_4$-

tetraedron. The MS1 path was constrained by an interatomic distance set to $(1 + (2/3)^{(1/2)})$ x $R_{As\text{-}O}$ and a Debye-Waller parameter of $\sigma^2_{As\text{-}O}$. The MS2 path was constrained by an interatomic distance of $2R_{As\text{-}O}$ and its Debye-Waller parameter was calculated as $\sigma^2_{MS2} = 4 \times \sigma^2_{As-O}$. The interatomic distance of MS3 was defined as 2x $R_{As\text{-}O}$ and its Debye-Waller parameter as $2 \times \sigma^2_{As-O}$ (Voegelin et al., 2007).

II.3 Results

II.3.1 Chemical analysis of the oxidation compound on the PTFE collector

The oxidation products collected on the PTFE scavengers were analyzed for major and trace elements. The concentrations obtained are given in Table II. 2 and compared with the soil horizon (A) and soil solution (SW). The origin in the soil solution of the oxidation products collected on the PTFE devices was previously determined by Al-Sid-Cheikh et al. (2015) following the rare earth element patterns of the soil solution and oxidation products. The Si and Al concentrations decreased from 30.4% and 30.0% in the soil to 1.1% and 0.5%, respectively, on the PTFE scavengers; which demonstrated the depletion of clay minerals and feldspars in the oxidation products compared to the soil organo mineral horizon. Conversely, the oxidation products were enriched in Fe and organic carbon (OC) with 8.5% of Fe and 75% of OC versus 1.1% of Fe, and 9% of OC in the soil. The As concentration increased from 7.39 mg Kg^{-1} in the soil to 239.31 mg Kg^{-1} on the PTFE scavenger surface. In the soil horizon and solution, the As/Fe ratio (wt/wt) was within the same order of magnitude, while this ratio increased by two orders of magnitude in the oxidation products. Thus, the oxidation products exhibited a strong enrichment in Fe, OC and furthermore in As.

Table II. 2 Major elements and As content of a wetland soil sample, surface water and oxidation products precipitated on PTFE scavengers

	Si	Al	Fe	K	Mg	Na	Ca	OC	As
	%								mg.Kg^{-1}
A[a]	30.4	30.0	1.1	0.8	0.3	0.1	0.2	9	7.4
PTFE scavenger[b]	1.1	0.5	8.5	0.1	0.2	0.1	0.6	75	239.3
	mg.Kg^{-1}								
SW[c]	4.49	0.28	1.29	0.77	10.83	13.41	6.01	38.0	5.5E-04

a: Organo-mineral horizon (0-15 cm)
b: Oxidation compounds precipitate on the PTFE scavengers
c: Surface water

II.3.2 NanoSIMS results

To investigate the distribution of As, the oxidation products were analyzed using a NanoSIMS probe. The ion distribution images for the $^{12}C^{14}N$, $^{56}Fe^{16}O$ and ^{75}As data are displayed in Figure II. 1. They highlight the heterogeneous distribution of the elements. The distribution of OM (as $^{12}C^{14}N$) and As (as ^{75}As) was anticorrelated, while the As distribution followed that of Fe. Arsenic-enriched hotspots (i.e. red squares 1 and 2 in Figure II. 1) were also observed. The distribution of As thus followed two trends: i) it was diffused in the matrix and ii) concentrated in hotspots in which the colocalizations of the elements varied. In hotspot 1, high As counts were associated with high Fe and low OM counts whereas in hotspot 2, high As counts were associated with high OM and low Fe counts.

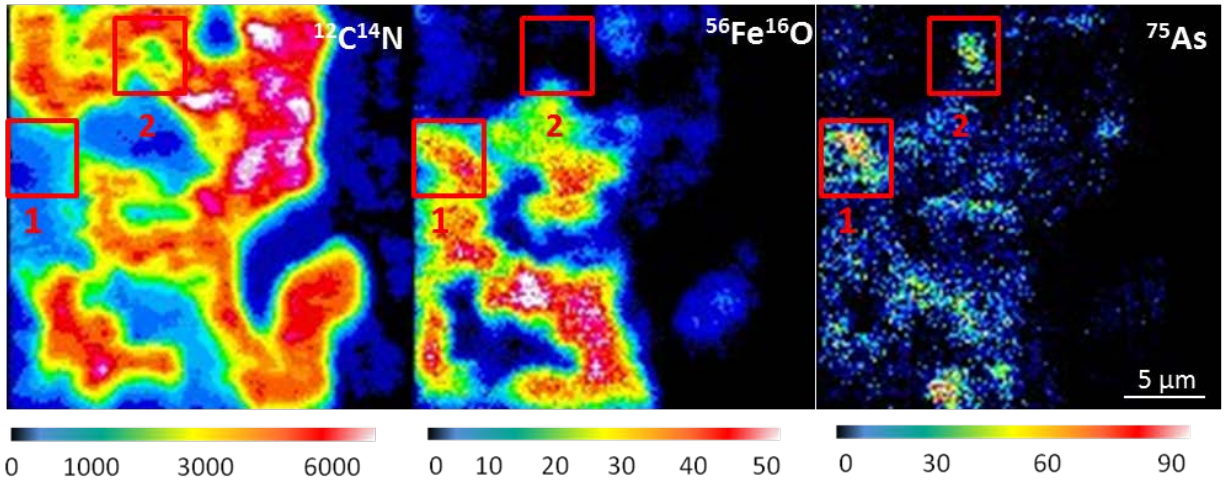

Figure II. 1 NanoSIMS images of the distribution of organic matter ($^{12}C^{14}N$), iron ($^{56}Fe^{16}O$) and arsenic (^{75}As) in the oxidation products. The red squares correspond to two As hotspots.

Pearson's coefficients (PC) were calculated to determine a statistic spatial distribution of the elements. However, using PCs alone may introduce ambiguity as PCs are highly dependent on signal intensity variations and on the heterogeneous colocalization relationships throughout the sample (Bolte and Cordelieres, 2006). Therefore, Mander's coefficients were calculated and taken into account when a positive colocalization was observed. The calculated Pearson's and Mander's statistic coefficients to determine the colocalizations in the entire image are displayed in Figure II. 2. The best correlation was observed for $^{56}Fe^{16}O/^{75}As$ with a PC value above 0.6 suggesting that the As distribution was intensively correlated to the one of Fe, as illustrated by hotspot 1. The determination of Manders' coefficients revealed that M1 and

M2 were similar, thereby indicating that the As and Fe distributions were linked. When $^{56}Fe^{16}O$ was present, ^{75}As was also present in more than 60% of the cases and when ^{75}As was present, $^{56}Fe^{16}O$ was present in more than 65% of the cases. A positive Pearson's coefficient value close to 0.1 was calculated for $^{12}C^{14}N$ and ^{75}As indicating that there was no correlation in the entire image. However, a M2 value around 0.4 showed that a fraction of the ^{75}As pixels was associated with the $^{12}C^{14}N$ pixels; which was evidenced by hotspot 2.

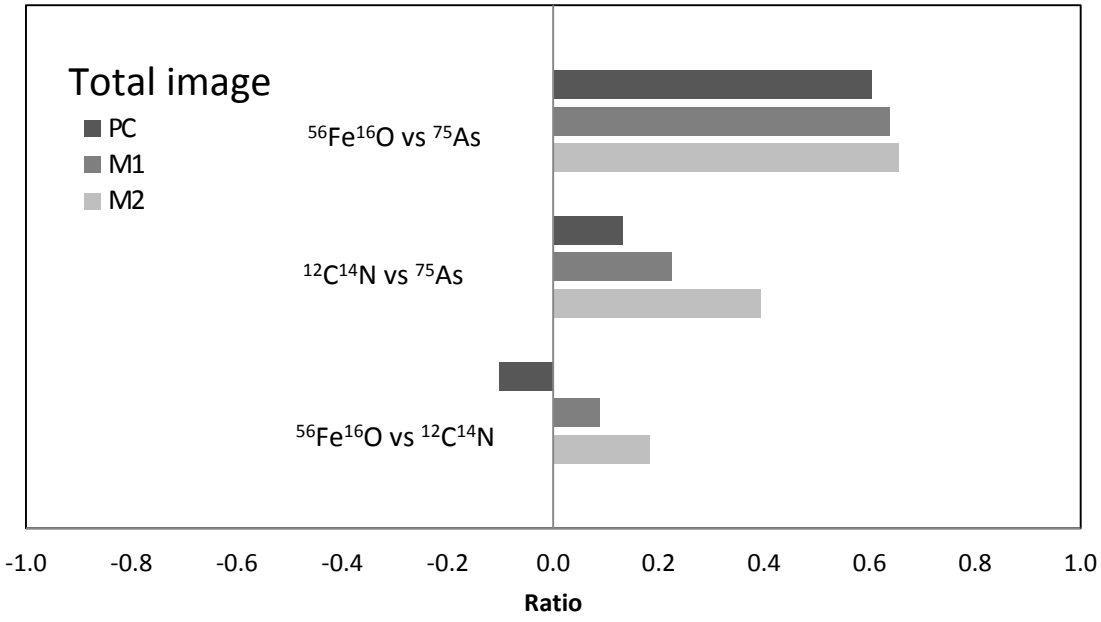

Figure II. 2 Colocalization of $^{56}Fe^{16}O$, ^{75}As and $^{12}C^{14}N$ using Pearson's (PC) and Manders' (M1 and M2) coefficients within the entire image

II.3.3 Arsenic X-ray Absorption Spectroscopy

II.3.3.1 As oxidation state

The oxidation state of As in the natural sample was determined collecting the XANES spectra in 13 different spots and in the bulk. The spectra are reported in Figure II. 3 with the As(V) and As(III) synthesized references. The normalized spectra exhibit various shapes. Arsenic (III) bound to ferrihydrite under anoxic conditions and As (V) bound to ferrihydrite under oxic conditions were used as references for the As(III) and As(V) spectra, respectively, and for the LCF. They exhibited a white line maximum at 11871.2 eV and 11874.5

eV, respectively. With regards to the synthesized samples of As(III) transferred into oxidizing conditions, As(III) associated with humic acid (HA-As(III)*oxic*) has a unique peak maximum at 11871.2 eV revealing no oxidation of As(III). In contrast, As(III) bound to ferrihydrite (Fh-As(III)*oxic*) exhibited a peak maximum at 11874.5 eV and did not show any shoulder at the low energy in the edge, suggesting that all of the As was entirely oxidized to As(V). The XANES spectrum of As(III) bound to Fe and HA (HA-Fe-As(III)*oxic*) exhibited two peaks at 11871.4 eV and 11874.8 eV, respectively, revealing the presence of both As(III) and As(V) with a proportion of 60% As(V) as determined by the LCF.

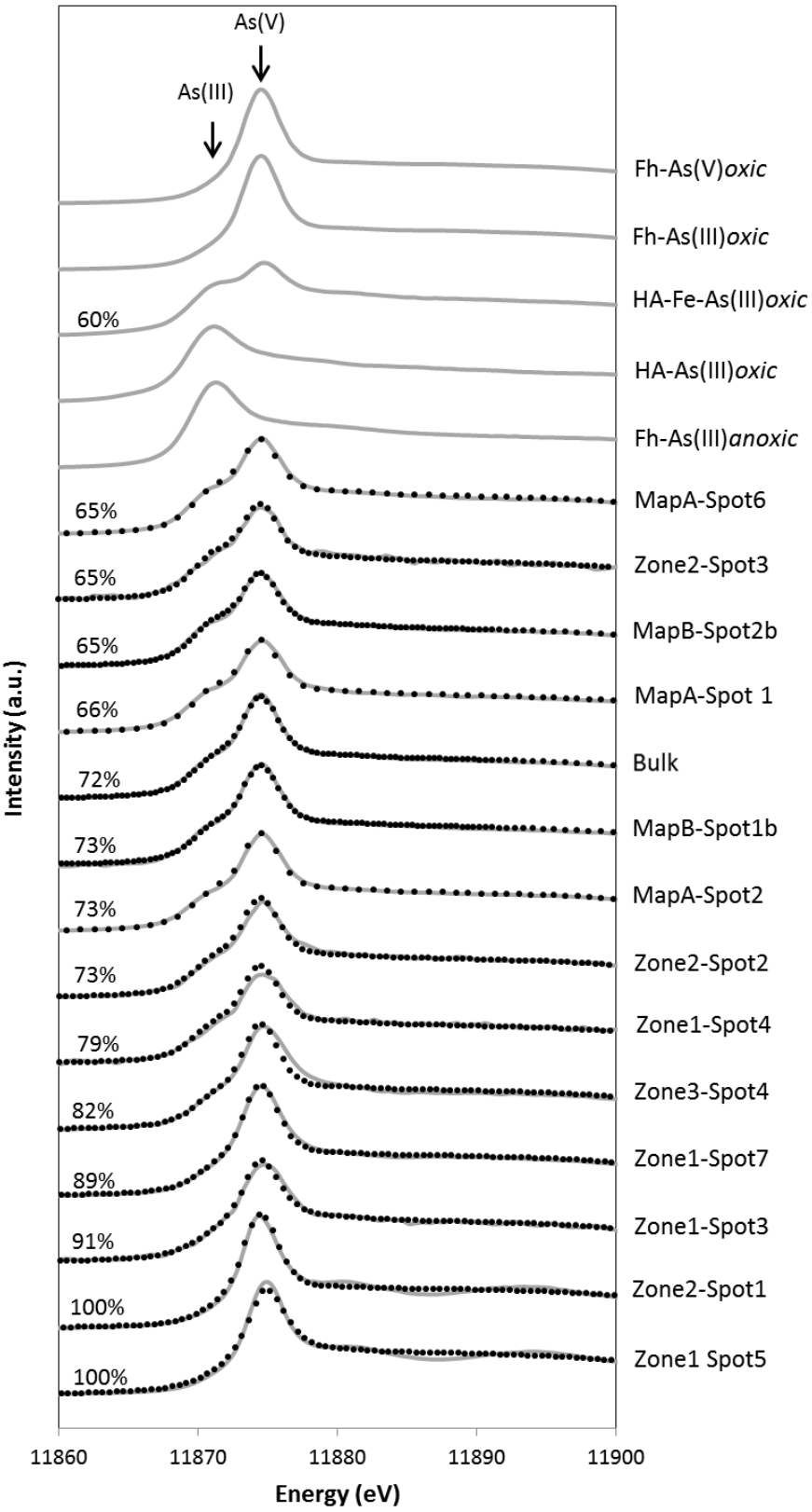

Figure II. 3 As K-edge X-ray absorption near-edge structure (XANES) spectra for different spots and the bulk of the natural sample along with the references. Solid lines correspond to experimental data and dashed lines are the linear combination fitting results. The calculation of the As(III) and As(V) contribution (expressed with As(V) percentage) to the natural sample derived from the LCF results are shown above each spectrum.

All of the natural sample spectra except two (i.e. Zone2-Spot1 and Zone1-Spot5) exhibited a shoulder at 11871.2 eV and a white line maximum at 11874.5 eV. The variations in intensity of the shoulder provide evidence of the presence of As(III) and As(V) at various proportions and heterogeneously distributed in the sample. The results of the LCF show that the As(V)/As(total) ratio ranged from 65% to 100%, depending on the studied spot. The bulk analysis showed 72% As(V), which corresponded to the average value of the measured ratios in the different spots. Both 100% As(V) spots (Zone2-Spot1 and Zone1-Spot5) exhibited features of a more crystallized structure revealed by the more pronounced oscillations in the post-edge region (Figure II. 3), possibly explained by a crystallized arsenate phase.

II.3.3.2 Nature and distance of the As neighbors

Despite the fact that our As concentration was rather low (i.e. 230 ppm in the digenetic precipitate) as compared to generally studied contaminated sites or As-enriched synthetic samples, it was possible to collect the EXAFS spectra in the bulk and in several spots. However, the low concentration explained the poorer signal/noise ratio quality compared to literature studies on samples artificially doped in As.

The As K-edge EXAFS data and the corresponding Fourier-Transform of the references and some spots collected in the natural sample are reported in Figure II. 4. Except for the HA-As(III)*oxic* reference, all of the EXAFS spectra exhibited a similar shape and oscillation positions. The second oscillation of the EXAFS spectra was characterized by a slight double-hump feature at approximately 6.7 and 7.4 $Å^{-1}$. The amplitude of the second hump was larger for the 100% As(V) spots and references, while the shoulder at 6.7 $Å^{-1}$ increased with the As(III) proportion. Additionally, the intensity of the oscillation at 8.3 $Å^{-1}$ decreased compared to the one at 6.0 $Å^{-1}$ when a mixture of As(III)/As(V) occurred. The main peak in the Fourier transform was located at R + ΔR ~1.3 Å and corresponded to the first neighboring shell. The natural sample spots, bulk and references, except HA-As(III)*oxic*, exhibited one or two additional small peaks at R + ΔR ~2.3 Å and ~3.0 Å accounted for the second coordination shell neighbors. To explore the local coordination of As, fits were performed in the 1-3.5 Å R-range. The results are reported in Figure II. 4. The fitted parameters and constraints for the references and the natural sample bulk and spots are reported in Table II. 3.

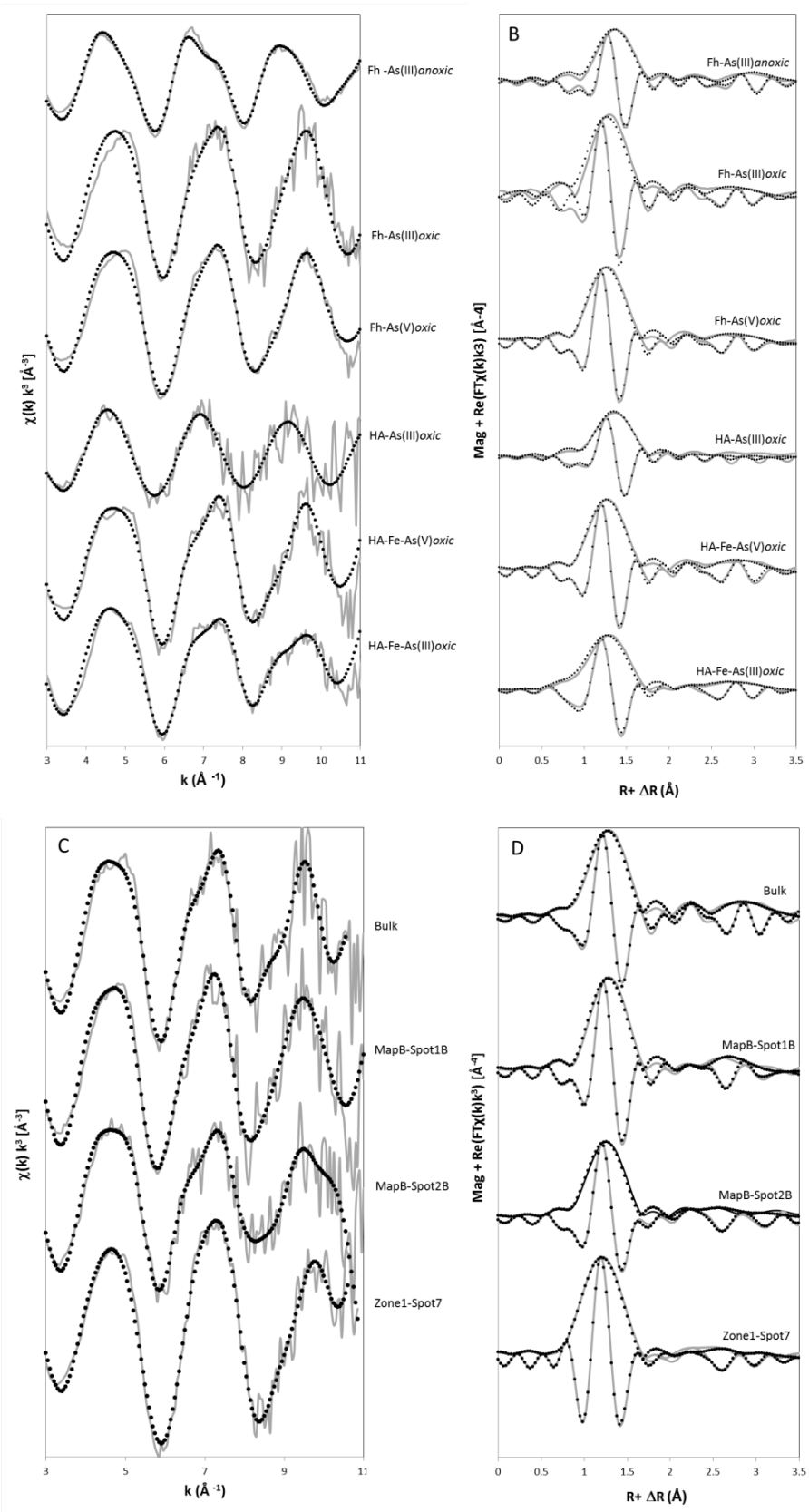

Figure II. 4 Arsenic K-edge EXAFS spectra and magnitude and imaginary part of the Fourier transform (uncorrected from the phase shift) of references A) and B) respectively, and of the natural sample bulk and three spots, C) and D) respectively. The fit results, given as dotted lines, are superimposed onto the data in solid grey lines.

Table II. 3 Shell-Fit parameters determined from the As K-edge EXAFS spectra of four spots and the bulk of the natural sample compared to the references

		As-O			As-Fe1			As-Fe2				
Sample	**% As(V)**	**R[a]**	**N[b]**	**σ^{2} [c]**	**R[a]**	**N[b]**	**σ^{2} [c]**	**R[a]**	**N[b]**	**σ^{2} [c]**	**ΔE(eV)[d]**	**R factor[e]**
Fh-As(III) *anoxic*	0	1.77 (1)	3.0 (3)	0.003	2.88 (4)	0.7 (4)	0.007	3.37 (4)	1.0 (7)	0.007	9.0 (7)	0.015
Fh-As(III) *oxic*	100	1.70 (1)	4.1 (3)	0.002				3.31 (5)	1.3 (9)	0.007	9.6 (7)	0.030
Fh-As(V) *oxic*	100	1.70 (1)	4.1 (6)	0.003				3.32 (4)	1.2 (9)	0.007	6.7 (15)	0.016
HA-As(III) *oxic*	0	1.76 (1)	2.7 (1)	0.003							9.1 (9)	0.029
HA-Fe-As(III) *oxic*	57	1.71 (4)	3.4 (3)	0.003	2.90 (9)	0.4 (5)	0.007	3.30 (4)	1.0 (10)	0.007	9.4 (9)	0.032
HA-Fe-As(V) *oxic*	100	1.70 (1)	3.9 (2)	0.003				3.33 (2)	1.7 (6)	0.007	7.3 (10)	0.016
Bulk	70	1.71 (1)	3.4 (10)	0.003	2.82 (25)	0.1 (4)	0.007	3.37 (2)	1.7 (6)	0.007	7.1 (12)	0.019
MapB Spot 1B	73	1.72 (1)	3.6 (6)	0.003	2.95 (4)	0.7 (3)	0.007	3.43 (6)	0.8 (4)	0.007	7.2 (14)	0.013
MapB Spot 2B	65	1.71 (1)	3.3 (3)	0.004	2.88 (5)	0.4 (5)	0.007	3.40 (3)	1.1 (14)	0.007	6.3 (8)	0.026
Zone1 Spot 7	89	1.70 (1)	4.1 (6)	0.003				3.28 (4)	0.6 (10)	0.005	2.8 (7)	0.032

The amplitude reduction factor, S_o^2, was set to 1. [a]R(Å), interatomic distance; [b]N path degeneracy (coordination number); [c]The Debye-Weller parameters were homogenized around a mean value; [d]Energy-shift parameter; [e]R-factor =$\Sigma i(data_i\text{-}fit_i)^2/\Sigma idata$. The Debye-Weller for the Fe-Fe paths are covaried with σ^2As-Fe_1= σ^2As-Fe_2. The reported errors are determined by the fitting procedure. Multiple scattering MS1, MS2 and MS3 were included in As(V) predominant samples: MS1 = triangular As-O-O MS path, R = 1.8165 x $R_{As\text{-}O}$, $\sigma^2 = \sigma^2_{As\text{-}O}$; MS2 = collinear As-O-As-O MS path, R = 2 x $R_{As\text{-}O}$, σ^2 = 4 x $R_{As\text{-}O}$, $\sigma^2 = \sigma^2_{As\text{-}O}$, MS3 = non-collinear As-O-As-O MS path, R = 2 x $R_{As\text{-}O}$, σ^2 = 2 x $\sigma^2_{As\text{-}O}$. Parameter uncertainties are presented for the last significant figure and determined by the fitting.

***First Oxygen shell*.** All of the first coordination shells could be fitted with oxygen neighbors. With regards to the As(V) references, in Fh-As(V)*oxic* and HA-Fe-As(V)*oxic*, the number of O neighbors is close to 4 (3.9 and 4.1 respectively) at a distance of 1.70 Å. On the contrary, in the As(III) reference (i.e. Fh-As(III)*anoxic*), only 3.0 O were detected at a longer distance, 1.77 Å. These results are in accordance with previous studies on As(V) (Manning et al., 2002; Morin et al., 2008) and As(III) (Ona-Nguema et al., 2005; Thoral et al., 2005) adsorbed onto Fe(III)-oxyhydroxides. The reference materials submitted to an oxidation process, in HA-As(III)*oxic*, the XANES LCF showed no As(III) oxidation which was supported by the number and distance of the O neighbors, respectively 2.7, close to 3, and 1.76 Å. In contrast, As(III) coprecipitated with Fh (Fh-As(III)*oxic*), had 4.1 O at the same distance as Fh-As(V)*oxic*, 1.70 Å, confirming the XANES LCF calculation which revealed that all of the As(III) was fully oxidized to As(V). Because of the partial oxidation of As(III) into As(V) revealed by the XANES spectra for the HA-Fe-As(III)*oxic* reference as well as for the spots collected in the natural sample and for the bulk, in all of these samples, the first coordination shell fit gave intermediary results with 3.4 to 4.0 O at 1.70-1.71 Å. The number of calculated oxygen neighbors was in agreement with the As(V) content in the mixture of As(III) and As(V).

Second coordination shell. Except in HA-As(III)oxic, in which no path could be added to improve the fit performed with the oxygen backscattering path, two As-Fe distances were used to fit the second coordination shell. The longer one, referred to as the As-Fe_2 path, was included in all of the fits with 0.6 to 1.7 Fe at an As-Fe interatomic distance of 3.28-3.43 Å. These distances are in agreement with those reported for As(III) and As(V) monodentate binuclear corner-sharing complexes ^{2}C (Manceau, 1995; Ona-Nguema et al., 2005; Waychunas et al., 1993) where As(III) and/or As(V) were bound to the apical oxygen atoms of two edge-sharing FeO_6 octahedra. The shorter distances (i.e. 3.28-3.33 Å) correspond to the references and samples that contain As(V) only, while the longer distances (i.e. (3.30)3.37-3.43 Å) correspond to the references and samples that contain As(III). These variations in the distances are in agreement with those reported by Farquhar et al. (2002) who additionally provided evidence of variations in the As-Fe distances as a function of the As-bearing Fe phase (namely As-Fe_2 distances are longer for As(III) binding to lepidocrocite than for As(III) binding to goethite). In the case of the references (Fh-As(III)*anoxic* and HA-Fe-As(III)*oxic*) and

the natural samples containing enough As(III) (> 11%), a shorter As-Fe_1 path had to be added with 0.4 to 0.7 Fe at a distance of 2.82 to 2.95 Å. These Fe neighbor backscatterers are reported in the literature as being due to the formation of As(III) bidentate mononuclear edge-sharing complexes, ^2E (Manceau, 1995; Ona-Nguema et al., 2005; Waychunas et al., 1993). In spot 7, in which the As(III) concentration was low (i.e. 11%), this last As-Fe interatomic distance could not be added. Because our studied wetland was not enriched in As (close to 200 mg Kg^{-1} in the oxidation solids and only 7 mg Kg^{-1} in the soil) the data quality was surprisingly good considering the use of a microbeam for the XAS analysis.

II.3.4 Iron X-ray absorption spectroscopy

After µXRF elemental mapping of the natural sample, Fe K-edge XANES analyses were performed on six spots containing various levels of Fe enrichment in order to characterize the As carrier phases. All of the XANES spectra were fairly similar. The edge position at 7125 eV associated with a tiny pre-edge at 7114.2 eV and a broad shoulder at 7148 eV reflect octahedrally coordinated Fe(III) species in a poorly crystalline phase (data not shown). The EXAFS spectra and the corresponding Fourier transforms (magnitude and imaginary part) of the bulk and two spots along with the references (i.e. Fh-As(V)*oxic*, Lp-As(V)*oxic* and HA-Fe-As(III)*oxic*) are reported in Figure II. 5. The EXAFS spectra line shape of both the spots and bulk were similar. They were different from the references. Similarly to HA-Fe-As(III)*oxic* and in contrast to Fh-As(V)*oxic* and Lp-As(V)*oxic,* they did not exhibit any shoulder in the oscillation at 5.2 $Å^{-1}$. However, they exhibited a shoulder peak at 7.6 $Å^{-1}$, the intensity of which varied according to the spectrum. This peak existed in both Fe(III)-oxyhydroxides but shifted to the low k at 7.3 $Å^{-1}$. Two peaks dominated the Fourier transform of the natural sample and the references, except HA-Fe-As(III)*oxic*. The first peak, located at approximately 1.5 Å (R+ΔR), corresponded to the first shell of the neighboring atoms within the FeO_6 octahedra. The second peak at approximatively 2.6 Å (R+ΔR) arose from the scattering of the Fe neighbors from the second coordination shell.

Shell fits were performed on the 1-3.8 A range of the Fourier transformed k^3-weighted spectra over a k-range 2-11 Å and displayed in Figure II. 5. The resulting EXAFS parameters of the fits are reported in TableII.4.

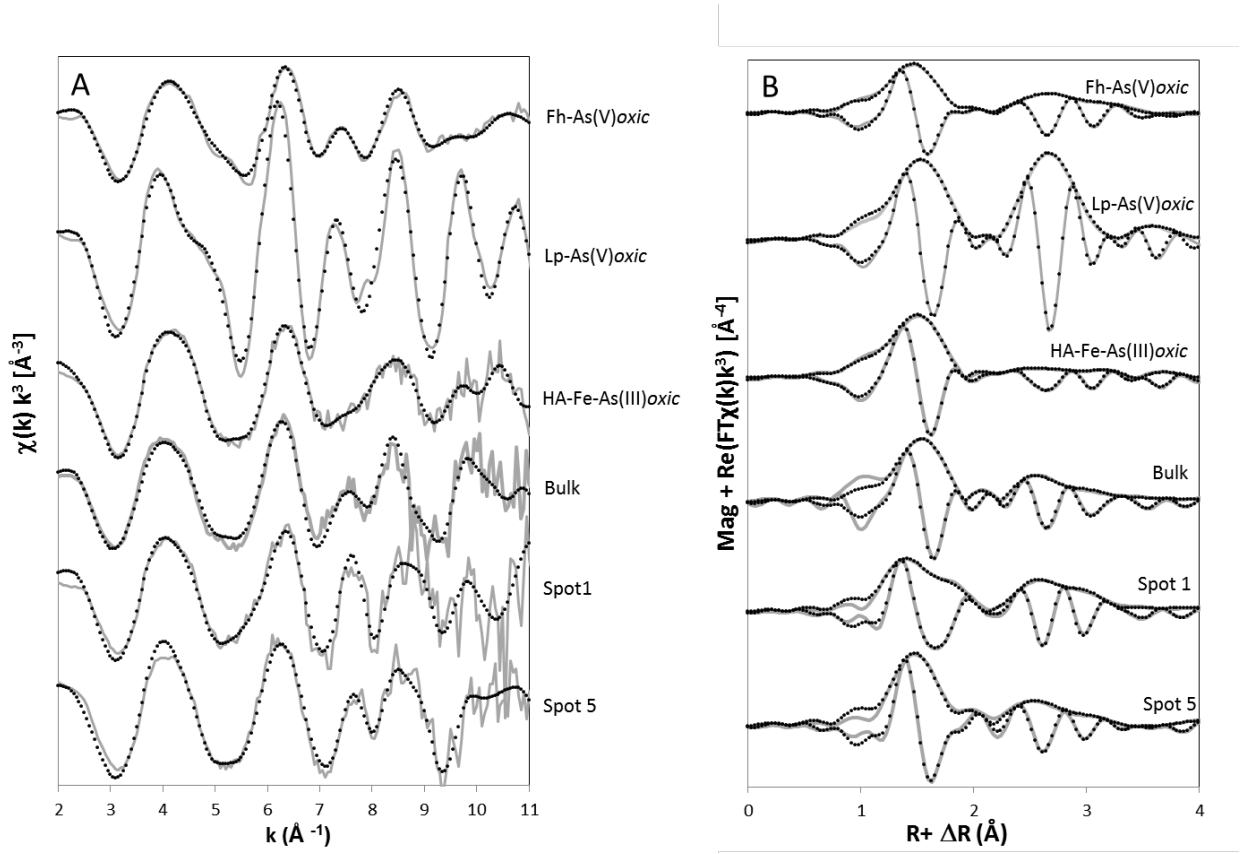

Figure II. 5 A) Iron K-edge EXAFS spectra of the references and two spots and the bulk of the naturel sample and synthetic references (Fh: ferrihydrite, Lp: lepidocrocite) and B) magnitude and imaginary part of the associated Fourier transform (uncorrected for the phase shift). Solid lines are experimental data and dotted lines are the fit results.

First coordination shell. For the references and the natural sample, two Fe-O paths were required to accurately reproduce the first O shell, with Fe-O distances at 1.93-1.97 Å and 2.06-2.15 Å. These distances corresponded to the Fe-O distances for the octahedra in the Fe(III)-oxyhydroxides (Waychunas et al., 1993). The sum of the coordination numbers (N) of the Fe-O_1 and Fe-O_2 paths ranged from 4.3 to 6.7. Values lower than 6 ± 10% could be explained by partially destructive interferences for the individual scattering waves produced by the multiple Fe-O distances within the octahedron (Manceau and Gates, 1997; Voegelin et al., 2010).

Table II. 4 Fe K-edge EXAFS fits for Fh, Lp and the HA-Fe-As complex along with the bulk and two spots of the natural sample.

Sample	Fe-O1			Fe-O2			Fe-C			Fe-Fe1			Fe-Fe2			Fe-O_{distal}			Fe-Fe3				
	R^a	N^b	σ^{2c}	R^a	N^b	σ^{2c}	R^a	N^b	σ^{2c}	R^a	N^b	σ^{2c}	R^a	N^b	σ^{2c}	R^a	N^b	σ^{2c}	R^a	N^b	σ^{2c}	$\Delta E(eV)^d$	R $fact^e$
Fh-As(V)*oxic*	1.93 (1)	2.7 (1)	0.003	2.09 (1)	1.6 (2)	0.003				3.03 (2)	1.8 (10)	0.010	3.49 (2)	2.7 (11)	0.010	3.60 (4)	4.2 (16)	0.010				0.9 (1)	0.004
Lp-As(V)*oxic*	1.95 (1)	3.4 (5)	0.002	2.08 (1)	3.1 (5)	0.002				3.07 (1)	6.5 (11)	0.006				3.56 (4)	2.3 (13)	0.006	4.02 (2)	1.7 (6)	0.006	1.1 (2)	0.002
HA-Fe-As(III) *oxic*	1.94 (3)	3.1 (16)	0.004	2.06 (5)	2.2 (15)	0.004	2.97 (2)	1.8 (6)	0.003	3.11 (5)	0.2 (8)	0.003	3.44 (2)	1.0 (14)	0.003	3.57 (1)	1.4 (2)	0.003				0.8 (4)	0.011
Bulk	1.94 (1)	2.2 (1)	0.002	2.06 (1)	2.5 (1)	0.002	2.77 (4)	1.6 (8)	0.007	3.04 (2)	2.4 (3)	0.007				3.82 (5)	2.8 (17)	0.007	3.91 (9)	0.4 (7)	0.007	0.7 (4)	0.012
Spot 1	1.94 (1)	3.1 (3)	0.002	2.12 (1)	3.2 (3)	0.002				3.01 (1)	1.5 (6)	0.003				3.76 (4)	2.8 (17)	0.003	3.90 (5)	0.3 (7)	0.003	1.3 (4)	0.012
Spot 5	1.97 (2)	4.1 (3)	0.002	2.15 (1)	2.6 (2)	0.002				3.02 (2)	1.6 (8)	0.005				3.69 (7)	1.3 (12)	0.005	3.86 (7)	0.2 (5)	0.005	1.3 (5)	0.018

[a]R(Å), interatomic distance; [b]N, path degeneracy (coordination number); [c]σ^2(Å), Debye-Waller factor; [d]Energy-shift parameter; [e]R-factor =$\Sigma i(data_i\text{-}fit_i)^2/\Sigma idata$. The amplitude reduction factor, $S0^2$, was set to 0.75 from Fh fit. The reported errors are determined by the fitting procedure. Parameters were covaried as follows: $\sigma^2Fe\text{-}O_1 = \sigma^2Fe\text{-}O_2$ and $\sigma^2Fe\text{-}Fe_{1\text{-}2\text{-}3} = \sigma^2Fe\text{-}C = \sigma^2Fe\text{-}O_{distal}$. Parameter uncertainties are presented for the last significant figure and determined by the fitting.

***Second coordination shell*.** The second peak at approximately 2.6 Å in the Fourier transforms (Figure II. 5) has a major contribution from the Fe neighbors. All of the spectra displayed a Fe-Fe_1 distance at 3.01-3.11 Å. This distance was characteristic of edge-sharing FeO_6 octahedra (Manceau and Combes, 1988; Manceau and Drits, 1993). The Fh-As(V)*oxic* and HA-Fe-As(III)*oxic* fit determined a Fe-Fe_2 distance at 3.44 and 3.49 Å respectively, specific to double corner-sharing as previously reported (Bottero et al., 1994; Manceau and Combes, 1988; Waychunas et al., 1993). The smaller number of Fe neighbors in HA-Fe-As(III)*oxic* than in Fh-As(V)*oxic* reflected the lower polymerization in the first reference. As in lepidocrocite, this distance did not exist in the natural sample spots and bulk while a longer Fe-Fe distance was determined at 3.84-4.02 Å, interpreted as a single corner-sharing octahedron, characteristic of a lepidocrocite structure (Manceau and Drits, 1993; Zhukhlistov, 2001). The absence of the 3.40 Å distance and the presence of the distance at approximately 3.90 Å in the natural sample, as in the lepidocrocite, therefore suggested that the Fe(III)-oxyhydroxides in the sample were lepidocrocite-like material. Lepidocrocite is commonly found in environments subject to oxic and anoxic fluctuations such as riparian wetlands (Schwertmann and Taylor, 1979). The coordination numbers for the Fe-Fe distances in the natural sample were much lower than in Lp-As(V)*oxic* suggesting the existence of nano-lepidocrocite in the natural sample. In HA-Fe-As(III)*oxic* as well as in the bulk sample, the addition of an Fe-C path at 2.97 and 2.77 Å, respectively, improved the fit by 33% based on the R factor. To evaluate the relevance of adding Fe-C scattering path, we used a F-test adapted for EXAFS fitting by Downward et al. (2006). The results from the F-test demonstrated that the addition of an Fe-C path improved the fit at a confidence level of 89% which is higher than the required 67% (Downward et al., 2006). Karlsson and Persson (2010) obtained a similar Fe-C path in Fe bound to peat humic acid. They interpreted this result as the formation of small polynuclear Fe(III)-NOM complexes. The lack of the Fe-C distance in the natural sample spots could be explained by the fact that we have focused on Fe-enriched zones. The Fe-bearing phase appeared to be heterogeneous with nano-lepidocrocite hotspots and more diffuse Fe as small Fe-clusters bound to organic matter.

II.4 Discussion

II.4.1 Parameters controlling As(III) speciation

In the studied natural sample corresponding to the oxidation products of a riparian wetland solution As(III) was at least partially oxidized, with a As(V) proportion varying between 65 and 100% relative to the analyzed spots. These results were in agreement with previous observations in peatlands (ThomasArrigo et al., 2014), floodplains (Parsons et al., 2013) and paddy soils (Yamaguchi et al., 2014), which reported incomplete As(III) oxidation in oxidizing conditions.

Several studies have reported that the oxidation kinetics of As(III) by O_2 is slow in the natural environment (Lowry and Lowry, 2002; Thoral et al., 2005). In freshwater, Eary and Schramke (1990) reported a half-life ($t_{1/2}$) of several months to one year for As(III) oxidation by O_2. The XAS analysis performed on the synthesized references highlighted the notion that the presence of Fe(III)-oxyhydroxides drastically influenced the As oxidation process. In the Fh-As(III)*oxic* reference (without OM), the edge position together with the lack of an observable shoulder at low energy in the XANES spectrum and the number and distance of the oxygen neighbors showed a total oxidation of As(III) into As(V). This complete As(III) oxidation induced by the presence of Fe(III) have been previously reported by Greenleaf et al. (2003). Two mechanisms has been proposed to explain the As(III) oxidation on the surface of the Fe(III)-oxyhydroxides. In the first hypothesis, dissolved O_2 was the oxidant of As(III) and the Fe(III)-oxyhydroxides acted as a catalyst (Auffan et al., 2008; Scott and Morgan, 1995; Zhao et al., 2011). This catalytic oxidation required an initial step of As(III) adsorption on Fe(III)-oxyhydroxides (Zhao et al., 2011). In the second hypothesis, Fe(III)-oxyhydroxides directly oxidized the adsorbed As(III) and released Fe(II) into the solution along with As(V). This latter species was possibly readsorbed onto the Fe(III)-oxyhydroxides (Greenleaf et al., 2003; Scott and Morgan, 1995). A portion of the Fe(II) is readsorbed onto the Fe(III)-oxyhydroxides (Greenleaf et al., 2003; Hiemstra and van Riemsdijk, 2007; Larese-Casanova and Scherer, 2007); however, Hiemstra and van Riemsdijk (2007) showed that at a pH below 7, as encountered in the studied wetland, readsorbed Fe remained as Fe(II). Note that no Fe(II) was detected from the XANES record at the Fe K-edge in any of

our samples (references or natural sample) suggesting that the readsorption processes did not occur or were not significant. Finally, Ona-Nguema et al., 2005 demonstrated that lepidocrocite alone could not oxidize As(III). All of these arguments suggest that the Fe(III)-oxyhydroxide catalysis was the most likely prevailing mechanism for As(III) oxidation in the studied wetland, (i.e. dissolved O_2 was the oxidant of As(III) and the Fe(III)-oxyhydroxides acted as a catalyst).

The possibility of As(III) oxidation by autotrophic bacteria containing the aioA gene (Engel et al., 2013; Jiang et al., 2014; Sanyal et al., 2016) can be rejected. This is because with the large quantities of Fe(III)-oxyhydroxides present in our sample, that the oxidation of As(III) by such bacteria should be minor.

However, the persistence of As(III) in our natural sample suggested that an additional parameter influenced the As(III) oxidation process. Organic matter plays a significant role: addition of OM to the As(III)/Fe(III)-oxyhydroxide system tended to slow down the As(III) oxidation process, as shown by the LCF calculations on the XANES spectrum for the HA-Fe-As(III)*oxic* reference (with OM and Fe), which showed that 60% of As occurred as As(V). Furthermore, in the HA-As(III)*oxic* reference (without Fe), no oxidation of As(III) occurred, based on the edge shape and position in the XANES spectrum and the As-O distances at 1.76 Å (corresponding to the As(III)-O distance). The presence of OM in an As(III) solution stored under an oxidizing condition thus seemed to prevent As(III) oxidation or slow down the oxidation kinetics compared to the reference material with Fe added. Two hypothesis can thus be considered: i) OM exerted a direct control on the reaction through As(III) binding onto its reduced surface groups, such as thiol (Catrouillet et al., 2014; Hoffmann et al., 2012; Langner et al., 2012); or ii) OM exerted an indirect control on the reaction by controlling the As binding phases.

The NanoSIMS analyses showed heterogeneity in the distribution of Fe, As and DOC. In addition to the diffused As in the sample matrix, As also appeared to be distributed in hotspots, mostly in Fe-enriched spots but also in several OM-enriched and Fe-depleted spots. Prior studies have provided evidence of the ability of OM to bind As via organosulfurs such as thiol groups (R-S-H)

(Couture et al., 2013; Hoffmann et al., 2014; Langner et al., 2012). In a previous study on the same material as ours, a colocalization of As and S was observed by the nanoSIMS analysis (Al-Sid-Cheikh et al., 2015). The correlation of the As and OM distribution observed from the NanoSIMS images could be explained by the formation of such As-OM complexes. Despite the observed As-OM colocalization in some spots, the EXAFS data did not show evidence of the direct coordination of As with OM (no As-C or As-S distances) while the Fe neighbors were always present, even in the spots containing the highest proportion of As(III). These results could be explained by the different scales of investigation provided by each technique. NanoSims probes the nanoscale while μXAS probes the microscale. Because a maximum of 40% of As(III) was observed and if the formation of As-S-OM monodendate complexes were hypothesized (Catrouillet et al., 2014; Hoffmann et al., 2014), 12% of the first neighbors around As would be S, which is at the detection limit of the EXAFS measurements. Consequently, the EXAFS fitting of our samples did not show any S neighbors. Note that the studies in which As binding to OM via thiol was evidenced by EXAFS spectroscopy concern either thiol enriched synthetic samples (Hoffmann et al. 2014) or natural samples formed in strongly enriched As systems (Langner et al., 2012). Therefore, the hypothesis regarding a direct control of OM on As(III) oxidation could neither be confirmed or invalidated here.

The second hypothesis considered that OM exerted a control on the As carrier phases and thus had an indirect influence on the As(III) oxidation process. The EXAFS data collected at the Fe K-edge revealed a lepidocrocite structure (Manceau and Drits, 1993; Pinakidou et al., 2015; Zhukhlistov, 2001). In a peatland area characterized by permanent flooding, ThomasArrigo et al. (2014) revealed that OM-enriched flocs contained both ferrihydrite and lepidocrocite. The difference in water saturation between peatlands and riparian wetlands is of major importance for the properties of OM and influences the formation process for Fe(III)-oxyhydroxides. Moreover, the formation of lepidocrocite (more crystallized than ferrihydrite) could be favored by several consecutive redox cycles as evidenced by Thompson et al. (2006) and shown by our samples. Yamaguchi et al. (2014), who studied As speciation in a paddy soil, observed under an oxic condition

the persistence of As(III) associated with lepidocrocite in the outer rim of the roots and As(V) associated with goethite and ferrihydrite in the inner rim. They interpreted this difference as the result of a slow oxidation rate allowing the formation of lepidocrocite as compared to the permanent supply of O_2 by the root channel inducing a faster oxidation and the formation of goethite and ferrihydrite. The coordination numbers for the second coordination shell were much lower than for the lepidocrocite reference (Lp-As(V)*oxic*) revealing the nanometric size of the studied natural lepidocrocite. This low degree of polymerization could be explained by the high OM concentration (75%). In the field, at the beginning of the oxidation period (water level decrease), the DOC concentration could reach 38 mg L^{-1} (Table II. 2). Dissolved organic carbon, which is strongly heterogeneous and may be composed of various organic molecules such as humic substances, could impair crystal growth and the aggregation of Fe(III)-oxyhydroxides (Cornell and Schwertmann, 2003; Pédrot et al., 2011). Under the oxidation period, in the present OM-enriched wetland, As(III) was therefore mainly adsorbed onto nano-lepidocrocite, and As(III) oxidation should have been catalyzed by Fe. Auffan et al. (2008) suggested that not all of the binding sites were active during the catalysis of the As(III) oxidation by the Fe(III)-oxyhydroxides. They localized the active sites in a six-membered FeO_6 octahedral ring on the maghemite surface onto which As was bound as a ^2C corner-sharing complex. Ona-Nguema et al. (2005) reported that As(III) was bound onto particulate lepidocrocite only via ^2C corner-sharing complexes. However, in the present natural sample, the As-Fe interatomic distance detected, close to 2.8 Å, demonstrated the possibility that an ^2E edge-sharing complex between As(III) and the identified nano-lepidocrocite is formed. Ona-Nguema et al. (2005) explained this discrepancy with the results of Manning et al. (2002) and Farquhar et al. (2002) by differences in the surface coverage. The number of ^2E sites in the lepidocrocite particles was limited compared to the ^2C sites. Therefore, when the surface coverage was higher, as in Ona-Nguema et al. (2005), ^2E would be masked by the increasing amount of ^2C. We calculated a concentration of 13.7 mg of As per g of Fe in Ona-Nguema et al. (2005) and 12 µg of As per g in Farquhar et al. (2002). This value is closer to the concentration of 2.81 µg of As per g of Fe in our study. The formation of nano-lepidocrocite

leads to a different $^{2}C/^{2}E$ ratio value, compared to particulate lepidocrocite, with an increase in the ^{2}E edge-sharing sites compared to the ^{2}C corner-sharing sites. The Fe K-edge EXAFS analysis of the bulk indicated the existence of a Fe-C distance , suggesting to a lesser extent the presence of Fe(III) as monomers or Fe-polymers in the OM matrix. Karlsson and Persson (2010) suggested that this distance could be attributed to five-membered chelate rings between Fe and OM, but they did not determine the size of these structures. Mikutta and Kretzschmar (2011) and Hoffmann et al. (2013) suggested the presence of mononuclear Fe(III) species or small Fe(III) clusters depending on the Fe(III) concentration. In the natural sample, the only possibility for As(III) to be bound to these Fe(III) monomers or small clusters was as ^{2}E edge-sharing complexes. The formation of ^{2}C corner-sharing complexes of As on two adjacent Fe(III) monomers is impossible due to geometrical constraints. Therefore, ^{2}E complexes were favored with the formation of nano-lepidocrocite and Fe(III) monomers. These hypotheses were supported by the variation in the coordination numbers for the ^{2}E and ^{2}C complexes between the bulk and the spots. In the spots, where the OM content varied compared to the bulk of the sample, the number of ^{2}E complexes increased whereas the ^{2}C complexes decreased. Arsenic(III) in ^{2}E edge-sharing complexes with nano-lepidocrocite and Fe monomers therefore helped to stabilize a fraction of As(III).

II.4.2 Involved mechanisms and environmental implication

In wetlands, under high water levels, when wetland soil saturation occurs, reducing conditions are developed. Soil and dissolved OM act as a source of C for Fe-reducing bacteria such as *Geobacter* (Dia et al., 2015). Subsequently, Fe(III)-oxyhydroxides are reductively dissolved and all of the associated elements (OM, metals, metalloids) are expected to be solubilized concomitantly. Under such high OM concentration conditions, OM prevents the formation of secondary Fe(II) minerals able to trap As by binding to Fe(II), and As is therefore maintained in solution mainly as labile species (Davranche et al., 2013; Catrouillet et al., 2014). When the water level decreases and evapotranspiration increases, oxidized conditions are restored; Fe(II) is expected to aggregate first as amorphous Fe(III)-oxyhydroxides and then to evolve to nano-lepidocrocite stabilized by the high OM

amount or is trapped as Fe(III) monomers or small clusters in the OM matrices. Such lepidocrocite stabilization has been previously observed by Chen et al., 2015. This oxidation/precipitation and trapping of Fe(III) probably first occurs through the formation of Fe/OM mixed colloids which, in a second time, progressively agglomerate and are deposited in the soil pores with the extent of the soil water disappearance. These associations are able to bind As(III). The size of the Fe phase results in a high capacity for As adsorption and thus an accumulation of As in the top level of the soil. In addition, the presence of OM partly prevents the oxidation of As(III) into As(V), thus preserving a certain quantity of the more toxic As species (i.e. As(III)) in the environment.

Based on this hypothesis, As mobility is entirely controlled by the transfer properties of their precursor colloidal form of the Fe/OM aggregates. This transfer ability is controlled by i) the size of the colloids, which controls their transport through the soil pores, as large colloids are rapidly eliminated with the water flow as shown in stormflow events (Neubauer et al., 2013) whereas small size colloids are retained for longer periods in the soil pores, ii) the soil porosity and permeability, and iii) the hydrophobicity and ionization capacity of the colloids, which controls their ability to be sorbed to the soil particles.

For a second time, after the aggregation and deposition of these Fe/OM associations in soil, As is immobilized with its carrying phase. In this situation, wetlands can be considered as retention or storage areas and not as the source of As as demonstrated by several authors, notably for the wetland and flooding plains along the Mekong (Fendorf, 2010; Kocar et al., 2008). However, the long term retention of As in riparian wetlands depends on the ability of such Fe/OM associations to persist in the wetland even under reducing conditions. Pédrot et al. (2011) demonstrated that Fe/OM associations are less stable with regards to bioreduction than the corresponding particulate Fe(III)-oxyhydroxides. However, Parsons et al. (2013) provided evidence that the repetitive redox cycle decreased As mobility and increased the As(V) proportion in the soil solid phase during the reduced half-cycle. They correlated this As(V) sequestration with the decreased dissolution of the Fe(III)-oxyhydroxides due to a finite DOC stock. In riparian wetlands, the supply of OM is theoretically not

limited but a poor quality of DOC (not enough metabolizable organic C) could have the same influence on the preservation of Fe(III)-oxyhydroxides in the system.

II.5 Conclusion

In this study we investigated the behavior of As and the role of OM during the reoxidation of a riparian wetland soil solution. PTFE scavengers were efficient devices to recover oxidation compounds directly from the soil.

The NanoSIMS results highlighted the heterogeneous repartitioning of As, Fe and OM within the sample as well as different colocalizations between the elements. A strong correlation existed between Fe and As distribution but several As and OM-enriched hotspots depleted in Fe were also observed. The assumption that these hotspots revealed direct binding between As and OM via the thiol groups was made, however we were not able to confirm this direct control by OM on As speciation using the XAS measurements. In our study, As was adsorbed onto Fe(III)-oxyhydroxides as As(III) and As(V). The presence of As(III) under such oxidizing conditions was explained by a partial oxidation of As(III) indirectly controlled by the presence of high quantities of OM. First, the presence of a large amount of OM in our wetland results in the formation of i) nano-lepidocrocite with a high specific surface area and of ii) small-Fe clusters bound to OM. The formation of both structures promoted As binding as ^{2}E complexes which are not able to oxidize As(III) (compared to ^{2}C corner-sharing complexes). This process resulted in the retention of a significant proportion of As(III) in the samples , even under oxidizing conditions.

In our studied riparian wetland, the soil seems to act as a retention area for As and not as the source of As, as already proposed by several authors.

Chapitre III. Variabilité de la spéciation de l'As dans les zones humides : un nouvel aperçu des mécanismes de contrôle de la dynamique de l'As

Dans la première partie de ce travail, j'ai montré que, dans les produits d'oxydation des zones humides, l'As était lié sous forme d'As(III) et d'As(V) à des polymères et des nano-oxydes de Fe dont la nature et la distribution sont contrôlées par la MO. Cependant, bien que j'ai pu observer par NanoSIMS, dans quelques 'hospots' micrométriques, des colocalisations entre As et carbone organique, ce travail n'a pas permis de mettre en évidence et de caractériser ces associations.

Les produits d'oxydation des sols de zones humides sont formés à partir de l'oxydation de la solution de sol produite en période de hautes eaux, lorsque le sol est saturé en eau. Cette solution réduite est enrichie en MO, en Fe(II) soluble, en As(III) (Ponnamperuma, 1972; Olivié-Lauquet et al., 2001; Grybos et al., 2007; Davranche et al., 2013; Al-Sid-Cheikh et al., 2015). Lorsque les précipitations diminuent et que l'évapotranspiration augmente, le sol est progressivement désaturé et l'oxygène pénètre petit à petit dans le système. Une des conséquences majeures est la réoxydation du Fe et sa précipitation en présence de fortes quantités de MO qui, comme je l'ai démontré, favorise la formation de nano-objets. Seulement, dans ces conditions, les solides formés sont en suspension dans la solution de sol et non agglomérés comme dans mon étude précédente lorsque le sol est asséché. Or, par le biais de séparations physiques (filtration/ultrafiltration), il est possible de séparer en fractions de différentes tailles cette suspension et d'en étudier les composants particulaires, colloïdaux, polymériques et solubles ainsi que les éléments chimiques associés. C'est ce que je me suis attaché à faire dans cette deuxième étude, avec pour objectif d'obtenir de plus amples informations sur les éventuelles associations As-MO identifiées par NanoSIMS.

Ce chapitre correspond à un article qui sera soumis prochainement dans Geochimica Cosmochimica Acta : Highlighting the large variability of As speciation in wetlands: a new insight in As dynamic control, Hélène Guénet, Mélanie Davranche, Delphine Vantelon, Martine Bouhnik-Le Coz, Emilie Jardé, Anne-Catherine Pierson-Wickmann, Vincent Dorcet, Jacques Jestin

Highlighting the large variability of As speciation in wetlands: a new insight in As dynamic control

RESUME

Plusieurs processus ont été identifiés pour expliquer la contamination des eaux souterraines par l'As. L'une d'elle concerne les zones humides bordant les fleuves et les conditions réductrices qui s'y développent. Si la saturation en eau des zones humides et les conditions réductrices qui les accompagnent provoquent la solubilisation de l'As qu'en est-il de la réoxydation, lorsque les zones humides s'assèchent ? Dans cette étude, nous nous sommes intéressés à la spéciation de l'As dans les différentes fractions en taille d'une suspension de produits d'oxydation d'une solution de sol de zone humide. Une solution réduite a préalablement été obtenue par incubation anoxique d'un sol prélevé dans la zone humide de Naizin Kervidy (France). Après filtration à 5 µm, la solution de sol a été réoxydée à l'air libre. La suspension obtenue a ensuite subi une série de séparations physiques par filtration et ultrafiltration (5 µm, 3 µm, 0,2 µm, 30 kDa et 5 kDa). La distribution de l'As, du Fe et du carbone organique (OC) a été déterminée dans chaque fraction par analyse géochimique. La spéciation du Fe et de l'As ont été étudiées par spectroscopie des RX (XAS) aux seuils K du Fe et de l'As et par chromatographie haute performance et d'exclusion stérique couplées à l'ICP-MS (HPLC et SEC-ICP-MS). La MO a été caractérisée par spectroscopie de fluorescence et spectrométrie de masse (GC-MS). Les résultats ont montré que l'As est présent sous forme d'As(V) mais qu'une quantité plus

faible d'As(III) est conservée en dépit des conditions oxydantes. Dans les fractions > 0.2 µm, les analyses XAS ont montré la présence de Fe et de C dans la seconde sphère de coordination de l'As (distances As-Fe = 3.35 Å et As-C = 2,90 Å). L'As est donc complexé sous forme de bidendates binucléaires ^{2}C au Fe et présent sous une forme organique. Pour les fractions <30 kDa, l'As est lié au C dans sa première sphère de coordination (As-C = 1,96 Å) indiquant l'apparition d'espèces organiques probablement méthylées. Dans la seconde sphère, une distance As-Fe à 3.35 Å indique que l'As est cependant encore complexé au Fe. Dans ces fractions, la MO est plus dégradée et présente un caractère plus humique qui lui permet d'avoir une plus grande capacité de complexation vis-à-vis des cations et notamment du Fe et donc de contraindre sa spéciation. Une quantité non négligeable d'As(V) est sous forme d'espèces organiques méthylées et cela, dans toutes les fractions. Ces espèces organiques sont produites par voies biologiques (faunes, flores et bactéries) via des processus de détoxification. Comme le suggère, la distribution en taille de ces espèces et les analyses SEC-ICP-MS, ces formes méthylées ne sont pas solubles mais liées aux phases nanométriques Fe-MO ou intégrées dans les résidus d'organismes vivants. Un bilan de masse des différentes fractions a montré que 90% de l'As se trouve dans les fractions particulaires et donc sous formes très faiblement mobiles. Cette étude montre que si les zones humides ont été identifiées comme source potentielle d'As pour le système hydrographique de surface ou souterrain, un certain nombre de mécanismes biologiques et géochimiques permet cependant le piégeage d'une grande quantité d'As. Enfin, un dernier point important est le rôle que pourrait jouer dans la mobilité de l'As, la fraction comprise entre 0,2 µm et 30kDa. Cette fraction est composée de structures colloïdales nanométriques riches en As et potentiellement, elle-même, mobilisable.

ABSTRACT

Due to the importance of arsenic (As) speciation for its mobility from the groundwater to the aquifer, we investigated the behavior of As during the oxidation of an iron (Fe) and organic-rich wetland soil solution. A soil from the Naizin Kervidy wetland (France) was incubated in the laboratory

to obtain a reduced solution which was then oxidized and filtered through a progressively decreasing pore size (5 µm, 3 µm, 0.2 µm, 30 kDa and 5 kDa). The fractional distribution of As among the particulate, colloidal and truly dissolved phases was investigated and coupled to speciation study using XAS, HPLC and SEC-ICP-MS and organic matter characterization using GC-MS and fluorescence spectroscopy. The results showed that a majority of As was present as As(V) but a small amount of As(III) remained despite the advance oxidized conditions. In the fractions > 0.2µm, XAS analyses showed the presence of Fe and C in the second sphere of coordination of As (As-Fe = 3.35 Å and As-C = 2,90 Å distances). The As was complexed to Fe as bidentate binuclear ^{2}C and also as organic species. In the fractions <30kDa, the short distance As-C at 1.96 Å, in the first sphere of coordination, was detected suggesting the presence of methylated organic species. In the second sphere, a distance As-Fe at 3.35 Å indicated that As was still associated with Fe below 30 kDa. In these fractions, the OM was more degraded with a more humic nature that enables it to have a higher adsorption capacity for cations such as Fe, constraining its speciation. A significant amount of As(V) was present as methylated organic species in all the fractions. These species are biologically produced (plants, small animals, fungi, etc.) via detoxification processes and could be bound to Fe(III) phases, colloidal OM or integrated in organism structures as showed by SEC-ICP-MS and size distribution. Even if the As was more concentrated in the 0.2-30kDa fraction, by comparing the total dry masses of all fractions, we determined that about 90% of the As was contained in the particulate fractions and thus immobilized. Defined as source for the catchment area or the underground river systems (Kocar et al., 2008; Polizzotto et al., 2008; Fendorf, 2010), this study highlighted that wetlands could act as trap for As due to geochemical and biological mechanisms. However the bioavailability of these As compounds and their potential remobilization during the reduced period need to be assess.

III.1 Introduction

Arsenic is a toxic element whose sources of contamination have been identified to be groundwater (Smedley and Kinniburgh, 2002). Several mechanisms were proposed to explain the As contamination of aquifers. Among them, riparian wetlands and floodplains appeared to be potential actors in the As solubilization process (Fendorf, 2010; Kocar et al., 2008). Arsenic enrichment was thereby identified in many wetland soils (e.g. Anawar et al., 2003; Du Laing et al., 2009). Riparian wetlands and floodplains are organic matter (OM)-enriched zones, adjacent to streams or rivers and characterized by seasonal flooding. They receive water from three different sources: i) the groundwater discharge, ii) the subsurface flow and iii) the flow from adjacent surface water body (Lewis, 1995). During the high water level subsequent to flooding, anaerobic conditions are established and promote the reductive dissolution of wetland soil Fe(III)-oxyhydroxides and associated elements such as As and OM (Davranche et al., 2011; Dia et al., 2015; Grybos et al., 2007, 2009; Olivié-Lauquet et al., 2001). Following its solubilization, As(V) is reduced to As(III), generally by autochthonous bacteria through detoxification or metabolism processes (Dia et al., 2015). When the water table decreases, the soil solution is reoxidized and newly formed Fe(III)-oxyhydroxides associated with OM precipitate as colloidal aggregates able to trap As (Aström and Corin, 2000; Bauer and Blodau, 2009; Sharma et al., 2011; ThomasArrigo et al., 2014). In such aggregates, colloidal or ionic Fe was demonstrated to act as a bridge between As and OM, thus forming ternary complexes (Ritter et al., 2006; Mikutta and Kretzschmar, 2011). These colloidal aggregates represent a first step in the agglomeration process resulting in solids deposition in soil porosity subsequently to evapotranspiration increase and water level decrease. Al-Sid-Cheikh et al. (2015) and Guénet et al. (2016) studied similar agglomerates collected directly in a wetland soil matrix (Naizin Kervidy, France). They demonstrated that As was heterogeneously distributed in both Fe-enriched zones and OM-enriched and Fe depleted zones. Al-Sid-Cheikh et al. (2015) suggested through NanoSIMS observations that As in OM enriched but Fe depleted zone could be associated to OM via thiol (SH) binding sites. However, X-rays absorption records displayed that As was mainly bound to OM via

Fe(III)-oxyhydroxides, Fe monomers or small clusters occurring as bridges in the ternary system. The speciation of As in OM enriched but Fe depleted zones remains, thereby, unresolved. However, to identify the control exerted by wetlands on As solubilization and dynamic, it is essential to understand and explain all the processes able to solubilize or trap As in such environment.

Natural oxidized solids, collected in wetland soil porosity, result from colloidal aggregates agglomeration. The objective of the present study was therefore to access the As speciation in such entities. For sampling simplicity and analysis quantification, colloidal aggregates were produced in laboratory subsequently to wetland soil anoxic incubations. After soil solution sampling and oxidation, the formed aggregates were size-fractionated using filtration and ultra-filtration. A study of As, Fe and OM distribution in each fraction was combined with the investigation of As and Fe speciation and OM characterization through multiple techniques. The OM was characterized using GC-MS and fluorescence spectroscopy, in each size fraction where As and Fe speciation were determined by K-edge XAS analysis. The smallest size fractions were investigated using size exclusion chromatography (SEC) combined with an inductive coupled plasma mass spectrometer (ICP-MS) and a high performance liquid chromatography (HPLC) combined with an ICP-MS. Finally, OM was characterized in each fraction using GC-MS and fluorescence spectroscopy.

III.2 Materials and Methods

III.2.1 Site description and soil sampling

The soil was recovered from the Mercy riparian wetland of Kervidy-Naizin located in Brittany in western France. This sub-catchment has been monitored since 1991 to investigate the effects of intensive agriculture (corn culture and livestock) on water quality. The hydrological, pedological and geochemical contexts are therefore well documented (Bourrié et al., 1999; Dia et al., 2000; Olivié-Lauquet et al., 2001; Gruau et al., 2004). The sampled uppermost soil horizon was defined as the organo-mineral horizon (Ah) of a planosol (according to the WRB international classification) which contained (wt%; anhydrous basis) OM (15%), clay (42%), quartz (30%) and Fe(III)-oxyhydroxides

(3.5%) (Grybos et al., 2007). Dissolved OM (DOM), Fe(II) and trace metal concentrations in soil solution were found to increase during flooding periods, from 0.83 to 2.5 mmol L^{-1} (DOM); from 0 to 0.21 mmol L^{-1} (Fe(II)) and from 0.01 to 0.025 µmol L^{-1} (As) (Dia et al., 2000; Grybos et al., 2007). Approximatively 5 kg of soil were collected in March 2015 from the surface layer, sieved at 2 mm and stored in the dark at 4°C to minimize latent biological activity.

III.2.2 Production of colloidal aggregates

To reproduce the reducing conditions observed in wetland soils, a soil suspension was set under anoxic condition in a Jacomex anaerobic chambers. The soil suspension was prepared in triplicate following the protocol from (Grybos et al., 2007). About 130 g of sieved soil were mixed with 1.8 L of a synthetic solution containing 0.48 mmol L^{-1} of $NaNO_3$ and NaCl, and 0.1 mmol L^{-1} of Na_2SO_4. The synthetic solution was adjusted to mimic the anionic composition of the soil solution during autumn (period of water table rise) in the Mercy wetland system. The experiments were performed in triplicate with an anhydrous soil/solution ratio of 1/20 (soil moisture = 44 wt%). The extend reduction was followed through the monitoring of the pH, Eh and Fe^{2+} and trace elements concentration increase subsequent to soil Fe-oxyhydroxides reductive dissolution. After one month under anoxic conditions, the pH, Eh and Fe^{2+} values reached 7.2, -130 mV and 29 mg L^{-1} respectively. The soil suspensions were thus filtrated using 5 µm cellulose nitrate filters (Sartorius). The three soil solutions were removed from the anaerobic chambers and set for oxidation at ambient air in the dark at room temperature during 2 weeks. Previous kinetic experiments (not published) revealed that equilibrium in elemental size distribution was reached after 2 weeks of oxidation. The triplicates were then size-fractionated using a series of filtration at 5, 3 and 0.2 µm and ultrafiltrations at 30 and 5 kDa. Firstly, two successive filtrations using cellulose nitrate membrane filters at 3 µm and 0.2 µm (from Sartorius) were performed. Then, the recovered fractions were ultrafiltrated using a Labscale TFF system equipped with two Pellicon XL membranes (PXC030C50 and PXC05C50).

III.2.3 As, Fe and OC concentration measurements

Organic carbon (OC) concentrations in the soil solutions were measured using an organic carbon analyzer (Shimmadzu TOC-V CSH). The accuracy of the dissolved organic carbon (DOC) measurements was estimated to be at ± 5% by using a standard solution of potassium hydrogen phthalate. The organic carbon (OC) content in freese-dried samples was determined at the INRA SAS laboratory in Rennes, France, using a dry combustion method with a CN Analyzer (Flash EA-1112). Concentration of Fe(II) from aliquots collected during the reduction of the soil solution were determined with the 1.10-phenantroline colorimetric method (AFNOR, 1982) at 510 nm using a UV-visible spectrometer (UV/VIS Spectrometer "Lambda 25" from Perkin Elmer). The Fe and As concentrations were determined by ICP-MS using an Agilent technologies 7700x at the University of Rennes 1. The samples were pre-digested twice with 14.6 N HNO_3 at 90°C, evaporated to complete dryness and then resolubilized with HNO_3 at 0.37 mol L^{-1} to avoid any interference with the DOC during the analysis. A flux of He was injected in a collision cell to remove interferences from $^{40}Ar^{35}Cl/^{75}As$ and $^{40}Ar^{16}O/^{56}Fe$. Quantitative analyses were performed using a conventional external calibration procedure (seven external standard multi-element solutions, Inorganic Venture, USA). Rhodium-Rhenium was added on-line as an internal standard at a concentration level of 300 mg L^{-1} to correct for instrumental drift and possible matrix effects. Calibration curves were calculated from the intensity ratios of the internal standard and the analyzed elements. The international geostandard SLRS-4 was used to control the accuracy and reproducibility of the measurement procedure. The instrumental error on the As and Fe analysis was below 3%. The chemical As and Fe blanks were below the detection limits (respectively 0.003 and 0.07 µg L-1), no correction was thus needed.

III.2.4 Transmission electron microscopy (TEM) observations

A drop of each fraction (i.e. 3-0.2µm, <0.2µm, <30KDa, <5KDa) was deposited on a 300 mesh copper grid coated with a lacey carbon film (Oxford Instruments, S166-3) and dry at room temperature. High Resolution Electron Microscopy (HREM) investigations were performed on a TEM

with a JEOL 100CXII instrument (voltage 100 kV) (THEMIS Analytical Facility at the University of Rennes 1). The elemental composition of the different structures was determined with a JEOL 2100F (voltage 200 kV) equipped with an X-ray energy dispersive spectroscopy (XEDS) detector (Kevex detector with an ultrathin window).

III.2.5 Organic matter characterization

III.2.5.1 THM-Gas chromatography-mass spectrometry (THM-GC-MS)

Approximatively 2 mg of each freeze-dried sample was introduced into an 80 µL aluminium reactor with an excess of solid tetramethylammonium hydroxide (TMAH – ca. 10 mg). The THM reaction was performed online using a vertical micro-furnace pyrolyser PZ-2020D (Frontier Laboratories, Japan) operating at 400° C for 1 min. The products of this reaction were injected into a gas chromatograph (GC) GC-2010 (Shimadzu, Japan) equipped with a SLB 5MS capillary column in the split mode (60m x 0.25mm ID, 0.25 µm film thickness). The split ratio was adapted according to the sample and ranged from 15 to 30. The temperature of the transfer line was 321 °C and the temperature of the injection port was 310 °C. The oven was programmed to maintain an initial temperature of 50 °C for 2 min, then rise to 150 °C at 15 °C min^{-1} and then rise to 310 °C at 3 °C min^{-1}, where it stayed for 14 min. Helium was used as the carrier gas, with a flow rate of 1.0 mL min^{-1}. Compounds were detected using a QP2010+ mass spectrometer (MS) (Shimadzu, Japan) operating in the full-scan mode. The temperature of the transfer line was set at 280 °C, the ionization source at 200 °C and molecules were ionized by electron impact using an energy of 70 eV. Compounds were identified on the basis of their full-scan mass spectra by comparison with the NIST library and with published data (Nierop and Verstraten, 2004; Nierop et al., 2005). They were classified into three categories: lignin and tannin markers, carbohydrates and fatty acids. The peak area of the selected m/z for each compound was integrated and corrected by a mass spectra factor calculated as the reciprocal of the proportion of the fragment used for the integration and the entire fragmentogram provided by the NIST library. The proportion of each compound class was calculated by dividing the sum of the areas of the compounds in this class by the sum of the peak areas of all analysed

compounds expressed as a percentage. The presented data are an average of the triplicates. We also investigated the presence of organic As species using the arsenobetaine reference compound ($C_5H_{11}AsO_2$ (AB) from Sigma Aldrich).

III.2.5.2 Fluorescence spectral analysis

At each fractionation step, we collected filtrate suspensions. The fractions below 5 µm, 3 µm, 30 kDa and 5 kDa and between 0.2 µm and 30 kDa were analyzed using a spectrofluorometer Perkin-Elmer LS 45 in a 10 mm quartz cuvette (at Ecole de Chimie de Rennes, France). The three dimensional excitation-emission fluorescence spectra were acquired by collecting individual emission spectra (290 - 600 nm) over a range of excitation ranging from 240 to 550 nm, with an increment of 5 nm, at a scan speed of 1500 nm/min. The slits set to 5 nm for both excitation and emission monochromators. The spectra obtained using this technique were treated using the mathematical method known as parallel factor analysis (PARAFAC) (Luciani et al., 2008). We calculated three indexes allowing the OM characterization. The fluorescence index (FI) (McKnight et al., 2001) is the ratio of the emission intensity at λEm 450 nm to that of λEm 500 nm using a fixed excitation at λEx 370 nm. The Biological index (BIX) (Huguet et al., 2009) is calculated from the ratio of emission intensities at λEm 380 nm and λEm 430 nm using a fixed excitation λEx 310 nm. Finally, the Fluorescence Humification index (HIX) (Zsolnay et al., 1999) is calculated as the ration of λ_{Em} 435-480 nm divided by λ_{Em} 300-345 nm at 254 nm at a fixed excitation of 254 nm.

III.2.6 XAS analysis

III.2.6.1 Data collection

All fractions were freeze-dried. The obtained powders were pressed into 6 or 7 mm pellets and fixed to the support using double-sided adhesive. Arsenic K-edge spectra were collected on the DiffAbs beamline and Fe K-edge spectra on the LUCIA beamline (Flank et al., 2006) of the SOLEIL Synchrotron (SOLEIL, St Aubin, France). On both beamlines, the monochromators were Si(111) double crystals. The 2nd on was bendable on DiffAbs for sagittal focusing. The beam size used for As K-edge on the sample was 286 x 228 µm. The beam size for Fe K-edge was 2 x 2 mm. Spectra were

collected in fluorescence mode using a 4-element silicon drift diode detector. To prevent beam-induced redox changes, samples were maintained under vacuum at 70K using a liquid nitrogen cryostat.

III.2.6.2 XAS data analysis

Arsenic and iron XAS spectra were extracted using the Athena software (Ravel and Newville, 2005) including the Autbk algorithm (Rbkb = 1, k-weight = 3). Normalized spectra were obtained by fitting the pre-edge region with a linear function and the post-edge region with a quadratic polynomial function. The Fourier transform of the k^3-weighted EXAFS spectra were calculated over a range of 2-10.5 $Å^{-1}$ using a Hanning apodization window (window parameter = 1). Back Fourier filters were extracted over the 1-3.5 Å R-range, using the same apodization window shape.

EXAFS data were analyzed by shell fitting using the software code Artemis (Ravel and Newville, 2005). Theoretical back scattering paths for the fits were calculated from different crystal structures using FEFF6. Scorodite (Kitahama et al., 1975), tooeleite (Morin et al., 2007) and 4-Hydroxy-3-nitrobenzenearsonic acid (Nuttall and Hunter, 1995) structures were used to extract paths from backscatters of As(V), As(III) and organic As species, respectively. Goethite (Hazemann et al., 1991) and Fe-carboxylate (Horcajada et al., 2007) structures were used to obtain the backscattering paths for Fe. Shell-fit analyses were performed within the 1-3.5 Å R-range for As and 1.1-3.5 Å for Fe. The best fit was chosen by minimizing the reduced χ^2 which depends on the number of independent parameters, the number of fitted parameters and the uncertainty of the data points. For As, the addition of multiple scattering tends to improve the quality of the fit (Morin et al., 2002; Voegelin et al., 2007). In the 5-3µm and 3-0.2µm fractions, the triangular As-O-O (MS1, degeneracy = 12), the collinear As-O-As-O (MS2 degeneracy = 4) and the non-collinear As-O-As-O (MS3, degeneracy = 12) paths were added for the fit of the $As^{(V)}O_4$-tetraedron. The MS1 path was constrained by an interatomic distance set to $(1 + (2/3)^{(1/2)}) \times R_{As-O}$ and a Debye-Waller parameter of σ^2_{As-O}. The MS2 path was constrained by an interatomic distance of $2R_{As-O}$ and its Debye-Waller parameter was

calculated as $\sigma^2_{MS2} = 4 \times \sigma^2_{\mathrm{As-O}}$. The interatomic distance of MS3 was defined as 2x $R_{As\text{-}O}$ and its Debye-Waller parameter as $2 \times \sigma^2_{\mathrm{As-O}}$ (Voegelin et al., 2007).

III.2.7 Arsenic in <30kDa and <5kDa fractions

III.2.7.1 SEC-ICP-MS

The distribution of Fe, OM and As in fractions below 30 kDa and 5 kDa was investigated using a separation method by SEC-ICP-MS technique. The separation was achieved using two online SEC NUCLEOSIL® 50 columns (250 mm x 4.6 mm) composed of unmodified spherical silica (50 Å pore size) from Macherey-Nagel, attached to an Agilent 1260 Infinity HPLC system (Agilent Technologies France) fitted with an autosampler. The columns were equipped with a prefilter/guard column (UltraShield UHPLC Trident Direct) with a cutoff of 0.45 µm (Restek Corporation). The mobile phase consisted of a sodium dodecyl sulfate (SDS, purity ≥98.5%), sodium nitrate ($NaNO_3$, purity ≥99.5%), and sodium citrate tribasic dehydrate (SC, purity ≥98%), with a pH of 6.5. The three products were purchased from Sigma-Aldrich. Stock solutions of 0.1 mol L^{-1} SDS, 0.1 mol L^{-1} $NaNO_3$ and 0.1 mol L^{-1} SC were prepared in ultrapure water (Milli-Q-water, Millipore system) and filtrated at 0.2 µm (with cellulose acetate filters from Sartorius, Germany). The mobile phase composition was obtained by mixing 5 % SDS, 10% $NaNO_3$ and 5% SC using an Agilent quaternary pumping system. The injection volume was 50 µL. The mobile phase flow rate was 0.9 mL min^{-1}, and the pressure was constant at around 235 bars. The SEC columns were followed by an Agilent UV detector from a 1260 Infinity system (excitation λ = 254 nm, emission λ = 410 nm) for organic molecules and an Agilent 7700 ICP-MS (Agilent Technologies, France) for other elements. A similar volume of 100 µL was injected for all samples. Before entering the ICP-MS, the effluent passed through an interface in which tellurium was mixed in as internal standard. This set-up allows the elemental composition to be determined as a function of particle size.

To investigate the dissolved As species potentially present, relevant As(III) and As(V) standards were used. They included i) two inorganic As species: sodium arsenite (Fluka Analytical) at 37 µg L^{-1} and sodium arsenate dibasic heptahydrate (Inorganic Ventures) at 28 µg L^{-1} and ii) three

organic methylated species at approximatively 18 µg L^{-1}: disodium methylarsenate hexahydrate, $CH_3AsNa_2O_3$ (MMA), dimethylarsenate, $C_2H_7AsO_4$ (DMA) and trimethylarsonio acetate or arsenobetaine, $C_5H_{11}AsO_2$ (AB) from Sigma Aldrich.

III.2.7.2 HPLC-ICP-MS

High performance liquid chromatography (HPLC) paired with inductively coupled plasma mass spectrometry (ICP-MS) has been used for characterization of As compounds in <30 kDa and <5 kDa fractions (Dobran and Zagury, 2006; Geiszinger et al., 2002; Huang and Matzner, 2007; Ronkart et al., 2007). The mobile phase consisted of NaH_2PO_4 (PBS, 2 mmol L^{-1}), $NaNO_3$ (3 mmol L^{-1}), CH_3COONa (10 mmol L^{-1}), EDTA-2Na (0.2 mmol L^{-1}) and CH_3OH (1%) (Sigma-Aldrich) at pH 11 and filtrated at 0.2 µm (using cellulose acetate filters from Sartorius, Germany). The injection volume was 50 µL with a mobile phase flow rate of 0.9 mL min^{-1}. An anionic column G3154A from Agilent Technologies 1100 Series (Tokyo, Japon) equipped with a guard column was used. The sample was injected with an autosampler (Agilent Technologies 1100 Series), using a 100 µL aliquot. In order to interpret the chromatograms, the same relevant reference materials previously used for SEC-ICP-MS experiment were analyzed with an injection volume of 30 µL.

III.3 Results

III.3.1 Chemical composition of the soil solution

The evolution of Fe, As and OC concentrations in the size fractions were plotted in Figure III. 1. In all fractions, OC was the most abundant varying between 102 and 129 mg g^{-1} in the first 3 fractions and increasing to 320 mg g^{-1} and 340 mg g^{-1} in 0.2µm-30kDa and <30kDa fractions, respectively. In <5 kDa fraction, OC decreased to 132 mg g^{-1}. Iron distribution varied as compared to OC. Iron concentrations increased from 23 mg g^{-1} in >5 µm fraction to 69 mg g^{-1} in 0.2µm-30kDa fraction. In the <30 kDa and <5 kDa fractions, Fe concentration significantly dropped to 13 mg g^{-1} and 1 mg g^{-1}, respectively. Most Fe was therefore present as particles (> 0.2 µm) and large size colloids

(between 0.2 µm and 30 kDa) where the Fe/OC was the highest. On the contrary, the smaller fractions (< 30 kDa) were Fe-depleted and OC-enriched and the Fe/OC was the lowest. Finally, the 0.2 µm-30 kDa fraction was the richest Fe and OM fraction; it seemed to correspond to Fe-OM-enriched colloids.

Above 30 kDa fraction, As distribution followed that of Fe. Arsenic concentration increased from 5 $\mu g.g^{-1}$ in < 5µm fraction, to 30 $\mu g.g^{-1}$ in the 0.2 µm -30kDa fraction, via a plateau at 15 mg g^{-1} in 5-3µm and 3-0.2µm fractions. About 20% of As was in <30 kDa fraction. Below this threshold, As decreased less drastically than Fe and their concentrations were weakly correlated indicating that small-size Fe species might not affect As partitioning. No apparent correlation was observed between As and OC distribution.

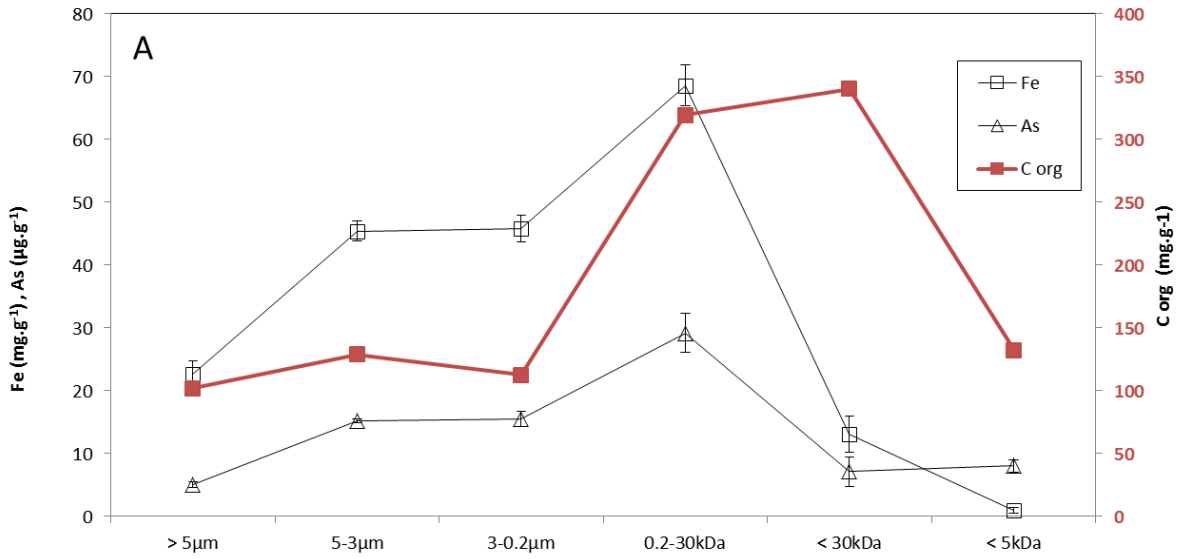

Figure III. 1 Evolution of Fe, OC and As concentrations in each fraction

The concentrations of As, Fe and OC were calculated relative to the total dry mass recovered for each fraction. The results were displayed in % in the Figure III. 2. The calculations showed that 88 % of the total As, 94 % of the total Fe and 92 % of the total OC were present in the >5 µm fraction since this fraction was the largest in mass. The second fraction in mass for the three elements was the 0.2µm-30kDa fraction composed by 6% of the total As and 4 % of total Fe and OC.

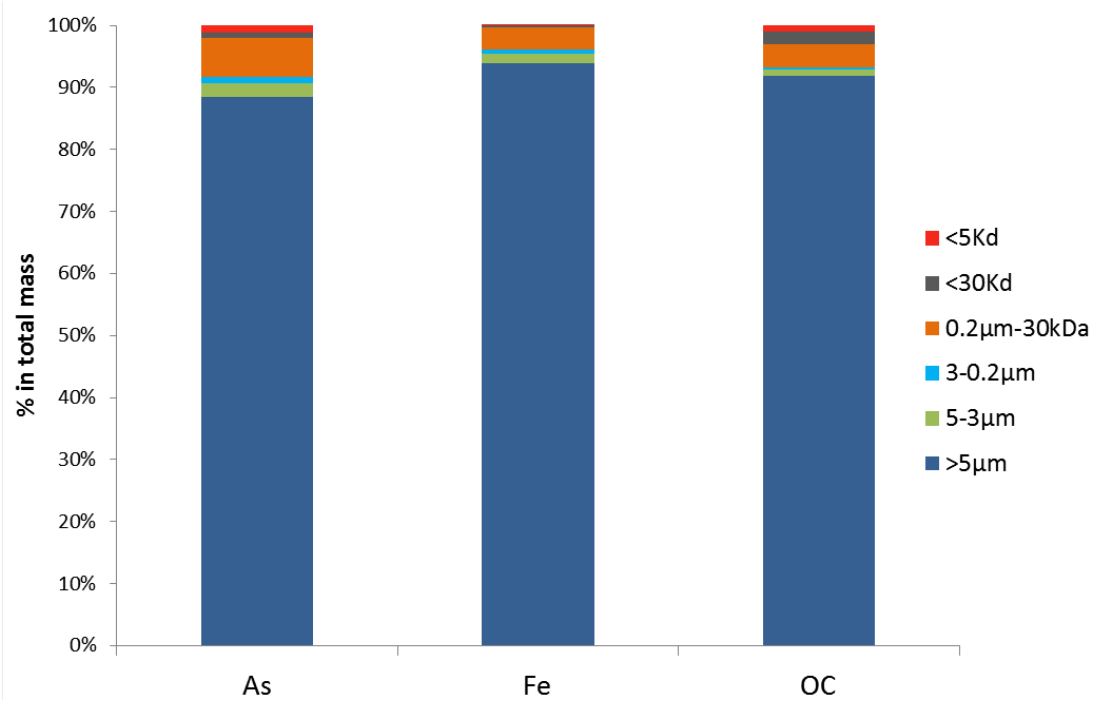

Figure III. 2 Repartition of the As, Fe and OC in the fraction considering the total dry mass recovered for each fraction

III.3.2 High resolution TEM observations of the different fractions

Representative transmission electron micrographs are presented for each fraction in Figure III. 3. The overall sample was heterogeneous as revealed by the micrographs of the largest fraction (Figure III. 3A). Micrometric organic compounds such as diatoms, and silicate plant (e.g. horsetail) remains were observed (Annexe I). The Fe phases were detected through their higher electron density and composition by EDS (Energy dispersive spectrometry) analysis. Goethite-like macro crystals (Annexe I) and Fe(III)-oxyhydroxides aggregates (red squares in Figure III. 2A and B) were observed. Figure III. 2B showed a close-up on a Fe(III)-oxyhydroxides aggregates constituted of numerous spheroid nanoparticles whose apparent size of around 4 nm was visible at high resolution (Figure III. 3C). With the increasing size fractionation, large compounds were removed and only dispersed Fe nanoparticles were observed for 0.2µm-30kDa fraction (Figure III. 2D). The analysis of the <30kDa fraction revealed the presence of very scarce small aggregates without any crystal lattice visible (Figure III. 2E). No aggregates were observed in the <5kDa fraction.

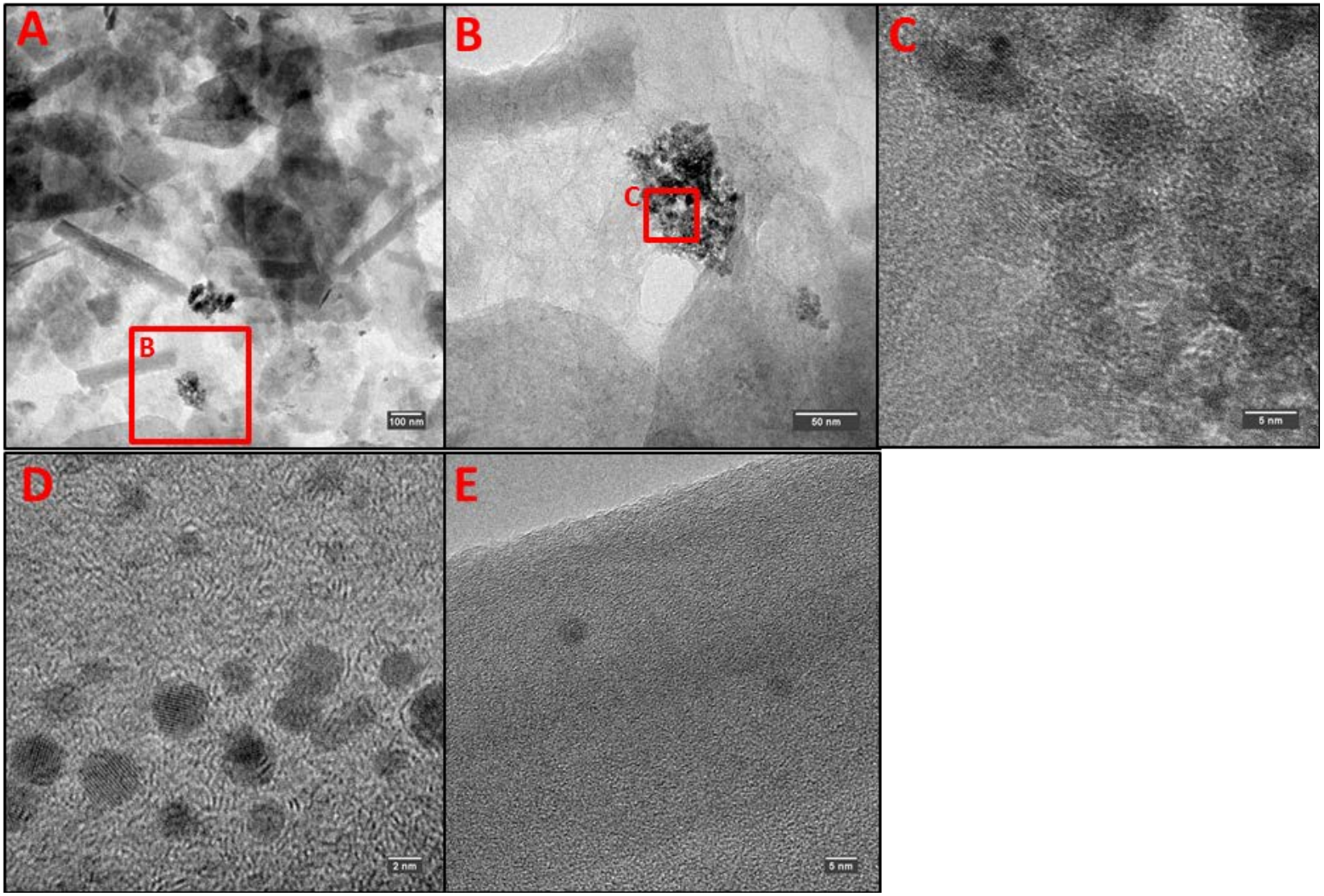

Figure III. 3 Representative TEM micrographs of different size fractions. A: large view of 3-0.2µm fraction. B: close-up on a Fe aggregate corresponding to the red square from micrograph A, C: high resolution micrograph of Fe nanoparticles from the red square of micrograph B, D: micrograph of 0.2µm-30kDa fraction and E: micrograph of <30kDa fraction.

III.3.3 Organic matter characterization

The molecular composition of each size fraction was investigated using THM-GC-MS. The different organic compounds, classified into fatty acids, lignin and tannin markers and carbohydrates, are presented in Figure III. 4. Among the size fractions, two groups with similar compositions could be distinguished according to their size: larger and smaller than 0.2µm. The larger size fractions were composed of more fatty acids than the small fractions (mean values of 61.1 *vs* 11.5 %) and contained less lignin and tannins makers (mean values of 27.4 *vs* 81.7 %). The increases of lignin and tannins markers were concomitants with the increase of OC concentration. Carbohydrates (or sugars) proportion decreased between the first (mean value of 11.5 %) and the second group (mean value of 6.9 %). Lignin and tannins markers were characteristic of OM derived from plant sources (Hedges and Parker, 1976), whereas carbohydrates and fatty acids were provided both by plant and microbial activities (Cranwell, 1974; Rumpel and Dignac, 2006). Low molecular weight (LMW) fatty acids are used as microbial indicators (Cranwell, 1974) while high molecular weight (HMW) fatty acids are used as plant indicators. The proportion of microbial fatty acids was calculated as the percentage of low molecular weight (LMW) fatty acids (<C19), by excluding C16:0 and C18:0, which can be either derived from plant or microbial input. In our samples, the proportion of high molecular weight (HMW) fatty acids in >0.2 µm fractions was greater (from 55 to 58%) than the proportions of LMW fatty acids (from 42 to 45%), whereas <0.2 µm fraction HMW fatty acids decreased and disappeared in <30 and <5 kDa fractions (Figure III. 4). A transition at the 0.2µm threshold between a plant-derived fraction and a microbial-derived one clearly appeared in our samples.

The fragmentograms of all fractions displayed the presence of As methylated species. The distinction between AB and DMA was not possible as the THM-GC-MS transformed the AB molecule into DMA. We calculated the repartition of these species in each fraction as a percentage of the total methylated As detected using the THM-GC-MS (red full line in Figure III. 4).

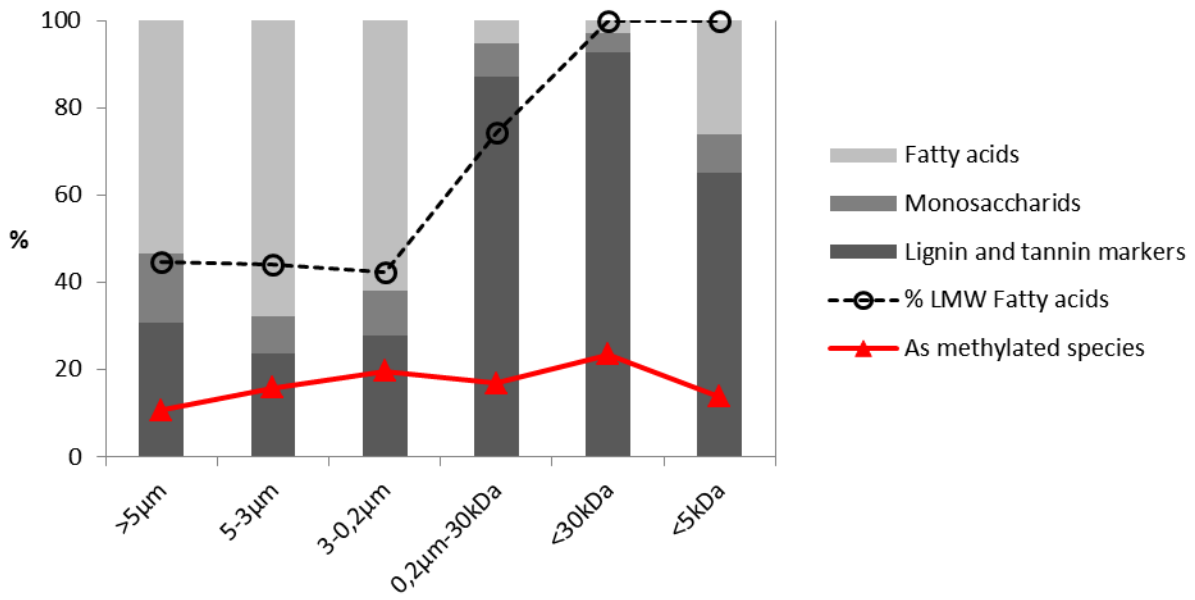

Figure III. 4 Histogram of the recalculate proportions of fatty acids, monosaccharides and the markers for the lignin and the tannin in each fraction. The superimposed dotted line represents the percentage of LMW of fatty acids and the full red line represents the repartition in % of the methylated arsenic species detected through GC analyses.

Indexes deduced from the fluorescence analysis are displayed in Figure III. 5. A mean value of 1.30 for the fluorescence index (FI) was calculated for >5 kDa fractions, indicating a terrestrial origin for OM. By contrast, the <5kDa fraction showed a more microbial derived OM with a FI of around 1.49. The Humification index (HIX) increased from 6.25 for the largest fraction to 22 and 30.11 for the 0.2µm-30 kDa and <30 kDa fractions, respectively. The HIX evolution showed that OM was more humified in the 0.2µm-30 kDa and <30 kDa fractions which corresponded also to the most OC-enriched fractions. The BIX index was constant with an average value of 0.4 indicating that OM was not freshly produced.

In summary, OM characterization suggested fractions > 0.2 µm were constituted of HMW organic molecules originated mainly from plant residue. By contrast, fractions< 0.2 µm were composed of soil humique molecules (such as humic acids). Organic compounds of the <5 kDa fraction were smaller and most probably sourced of bacterial activities.

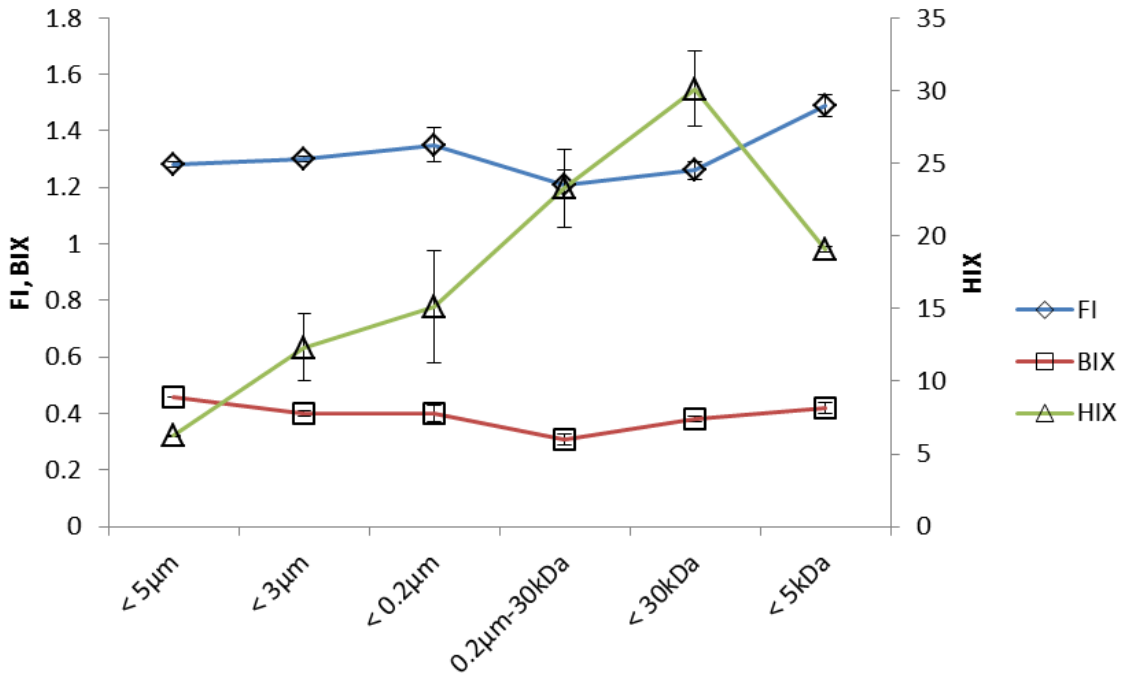

Figure III. 5 Evolution of the three characterization index. FI: fluorescence index; BIX: Biological index and HIX: Fluorescence humification index.

III.3.4 Characterisation of Fe phases using XAS

The Fe K-edge XANES analysis performed on each fraction were fairly similar. The edge position at 7125 eV associated with a tiny pre-edge at 7114.2 eV and a broad shoulder at 7148 eV reflected octahedral coordinated Fe(III) species in a poorly crystalline phase (data not shown). The EXAFS spectra and the corresponding Fourier transforms (magnitude and imaginary part) of each fraction as well as ferrihydrite (Fh) as reference were reported in Figure III. 6. The EXAFS spectra of the fractions were fairly similar with three peaks at 4.1 Å, 6.3 Å and about 8.4 Å. A small peak at around 7.5 Å was observed in the 5-3µm, 3-0.2µm and 0.2µm-30kDa fractions and reference Fh, but not in <30kDa and <5kDa fractions. Two peaks dominated the Fourier transform. The first peak, located at approximately 1.5 Å (R+ΔR), corresponded to the first shell of the neighboring atoms within the FeO_6 octahedra. The second peak at approximatively 2.6 Å (R+ΔR) arose from the scattering of the Fe neighbors from the second coordination shell. Shell fits were performed on the 1.1-3.5 A range of the Fourier transformed k^3-weighted spectra over a k-range 2-10.5 Å and displayed in Figure III. 6. The resulting EXAFS parameters of the fits are reported in Table III. 2.

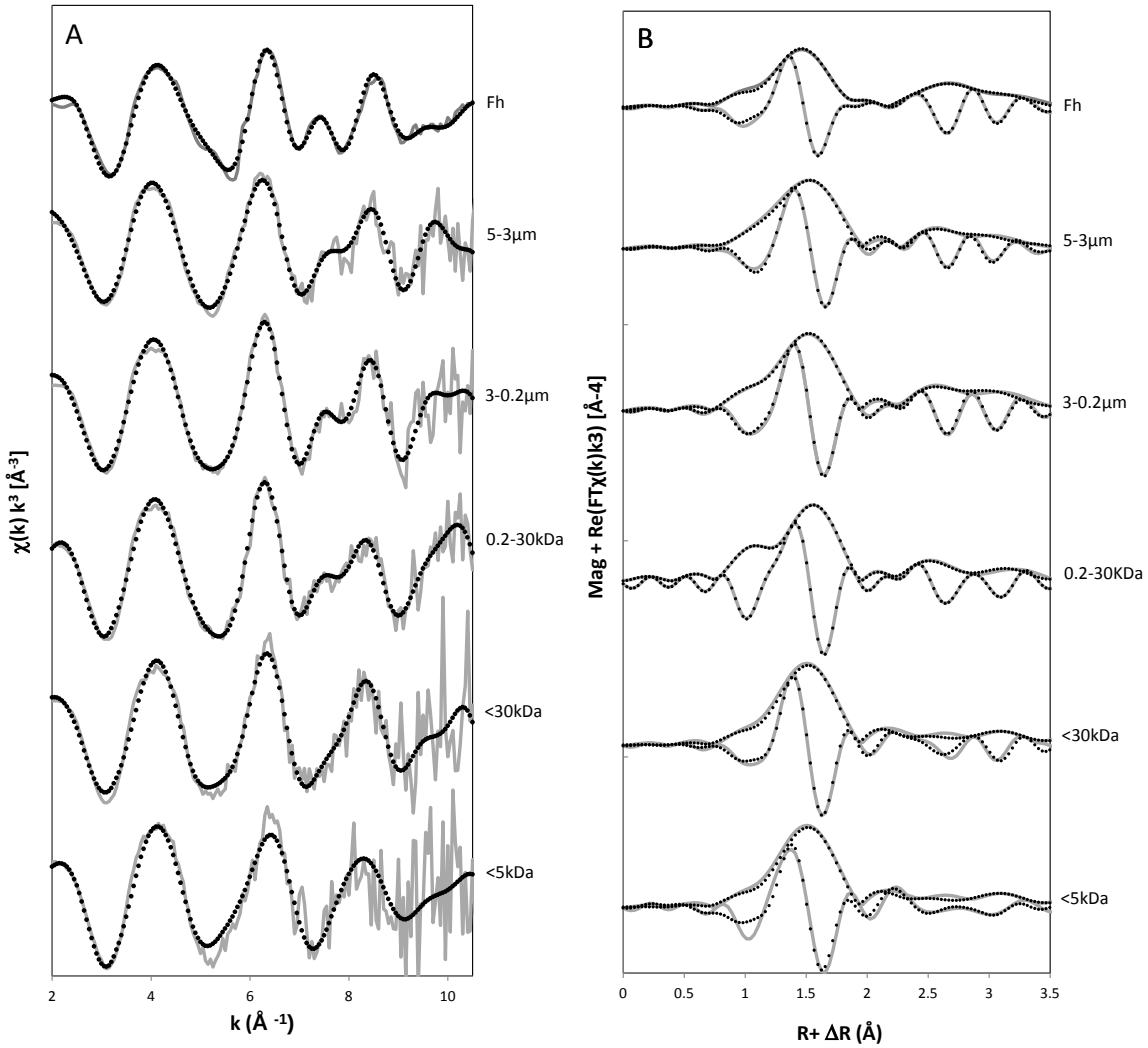

Figure III. 6 A) Iron K-edge EXAFS spectra of the different size fractions and ferrihydrite (Fh) and B) magnitude and imaginary part of the associated Fourier transform (uncorrected for the phase shift). Solid lines are experimental data and dotted lines are the fit results.

First coordination shell. The first O shell was fitted with about 6 O at a mean distance of 2.00 Å respectively. These distances corresponded to the Fe-O distances for the octahedra in the Fe(III)-oxyhydroxides (Waychunas et al., 1993). The number of O was later fixed to 6 to reduce parameter correlations.

Second coordination shell. The second peak at approximately 2.6 Å in the Fourier transforms (Figure III. 6) has a major contribution from the Fe neighbors. The 5-3µm, 3-0.2µm and 0.2µm-30kDa fractions spectra displayed a Fe-Fe_1 distance at 3.03-3.09 Å characteristic of edge-sharing FeO_6 octahedra (Manceau and Combes, 1988; Manceau and Drits, 1993). A second Fe-Fe_2 distance was determined in all fractions at 3.38-3.49 Å, specific to a double corner-sharing (Manceau and Combes,

1988; Combes et al., 1989; Waychunas et al., 1993; Bottero et al., 1994). In order to accurately model the spectra of the three smallest fractions, an Fe-C distance was added in the fit with 3.8 C at 2.95 Å for the 0.2µm-30kDa fraction, 2.4 C at 2.91 Å for the <30KDa fraction and 3.3 C at 2.86 Å for the <5kDa fraction. The highest OC/Fe concentration ratio was obtained for these three fractions explaining why the Fe-C distance was observable. Karlsson and Persson (2010) obtained a similar Fe-C path in Fe bound to peat humic acid. They interpreted this result as the formation of small polynuclear Fe(III)-OM complexes. The 0.2µm-30kDa fraction could be considered as an intermediate fraction containing the two Fe-Fe distances (Fe-Fe1 and Fe-Fe2) and Fe-C distance while the first Fe-Fe1 distance disappeared in the <30 kDa and <5 kDa fractions. In agreement with Hoffmann et al. (2013). These distances provided evidence of the presence of small Fe clusters and /or Fe(III)-oxyhydroxide nanoparticles in the 0.2µm-30kDa fraction although only small clusters such as dimer or trimer were formed in the <30 kDa and <5 kDa fractions.

III.3.5 Speciation of Arsenic by X-ray Absorption Spectroscopy

As K-edge XANES. The speciation of As in the different size fractions was determined by comparing the sample XANES with known references. Fractions and inorganic As(III) and As(V) references spectra were reported in Figure III. 7. The white line energies observed for arsenite (11872.4 eV) and arsenate (11875.5 eV) corresponded to the literature (Smith et al., 2005). White line peak positions were obtained from the point where the first derivative of the spectrum crossed zero. The fractions exhibited a peak maximum at 11875.6 eV for 5-3µm fraction, 11875.2 eV for 3-0.2µm fraction and 11874.8 eV for 0.2µm-30kDa fraction closed to the white line value of arsenate. They exhibited a shoulder at lower energy (around 11872.3 eV) which intensity increased with the size fractionation. The shoulder and white line positions corresponded to a mixture of inorganic As(III) and As(V) (Guénet et al., 2016). The spectra of <30kDa and <5kDa fractions exhibited a unique peak at 11874.0 and 11874.2 eV, respectively. Those values did not correspond to inorganic species. Prior studies investigating the white line positions for multiple As compounds revealed that As(V) organic compounds such as AB, DMA and MMA have intermediate white line position due to the

Table III. 1 Fe K-edge EXAFS fits for the different fractions and the ferrihydrite reference.

	Fe-O			Fe-C			Fe-Fe1			Fe-Fe2				
Sample	**N[a]**	**R[b] (Å)**	**σ^{2} [c]**	**N**	**R (Å)**	**σ^{2}**	**N**	**R (Å)**	**σ^{2}**	**N**	**R (Å)**	**σ^{2}**	**ΔE_0 [d]**	**R factor [e]**
Fh	2.7 (1)	1.93 (1)	0.003				1.8 (10)	3.03 (2)	0.010	2.7 (11)	3.49 (2)	0.010	0.9 (1)	0.004
	1.6 (2)	2.09 (1)	0.003											
5-3µm	6	2.01 (1)	0.009				2.4 (4)	3.07 (4)	0.013	0.9 (2)	3.38 (4)	0.005	-2.2 (9)	0.016
3-0.2µm	6	1.99 (1)	0.008				1.8 (3)	3.03 (2)	0.009	1.2 (3)	3.42 (2)	0.005	-2.2 (5)	0.010
0.2µm-30kDa	6	2.02 (1)	0.009	3.8 (4)	2.95 (2)	0.005	0.7 (1)	3.09 (8)	0.004	1.1 (1)	3.49 (2)	0.005	2.1 (14)	0.003
<30kDa	6	1.99 (1)	0.007	2.4 (9)	2.91 (6)	0.005				1.6 (6)	3.43 (3)	0.005	1.9 (8)	0.022
<5kDa	6	1.99 (2)	0.008	3.3 (19)	2.86 (9)	0.005				0.7 (9)	3.39 (2)	0.005	2.2 (23)	0.050

[a]N, path degeneracy (coordination number); [b]R(Å), interatomic distance;; [c]σ^2(Å), Debye-Waller factor; [d]Energy-shift parameter; [e]R-factor =$\Sigma i(data_i - fit_i)^2/\Sigma idata$. The amplitude reduction factor, S_0^2, was set to 0.75 from Fh fit. The reported errors were determined by the fitting procedure. The Debye-Waller of Fe-Fe_2 and Fe-C distances were determined from the <30kDa fraction and then fixed to these values in all fractions. Parameter uncertainties are presented for the last significant figure and determined by the fitting.

difference in O and C electronegativities (Arčon et al., 2005; Smith et al., 2005; Lombi et al., 2009). Core electrons of As atoms in an As-C bond are more easily photoionized than the 1s electrons of As in an As-O bond. The white line position observed for <30 kDa and 5KDa fractions, could thus be attributed to As(V)-methylated compounds such as AB, DMA or MMA. The distinction between each species is prevented by the XANES inability to discriminate between two aliphatic substituents on the C backbone (George and Pickering, 2007).

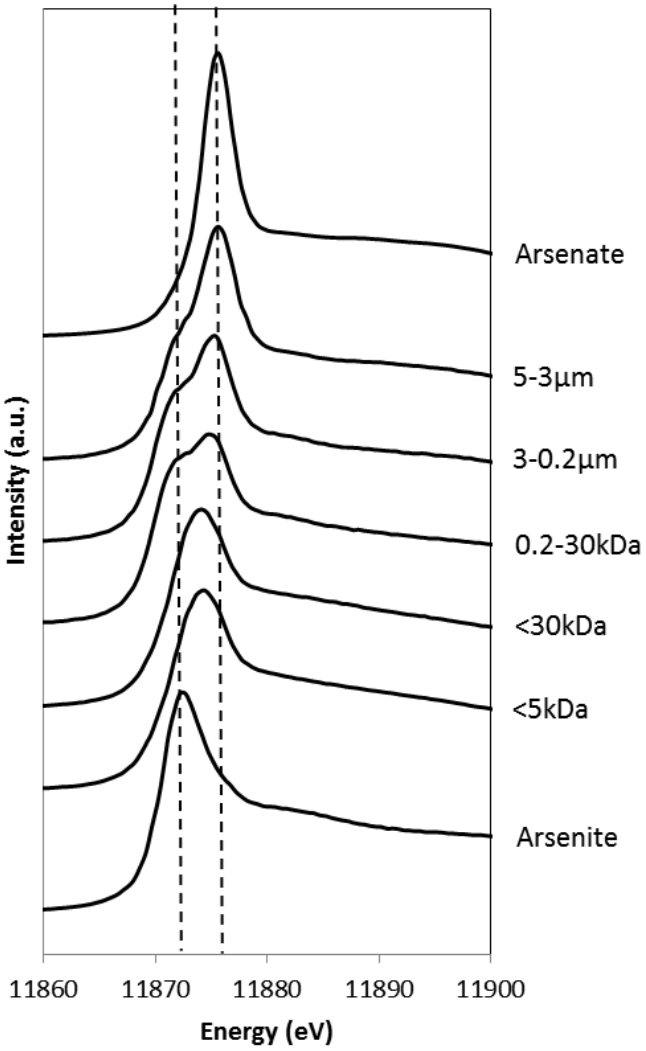

Figure III. 7 As K-edge X-ray absorption near-edge structure (XANES) spectra of different fractions of the oxidized soil solution along with inorganic As(III) and As(V) references.

As K-edge EXAFS. The As K-edge EXAFS data and the corresponding Fourier-Transform of each size fractions are reported in Figure III. 8. Due to a lower concentration in As, the quality of the

data of the <30kDa and <5kDa fractions had poor signal/noise ratio compared to larger size fractions. However, the quality was good enough to extract information. From 5-3µm fraction to 0.2µm-30kDa fraction, EXAFS spectra exhibited a shoulder at 5.05 $Å^{-1}$. The second oscillation was characterized by a slight double-hump feature at approximately 6.55 and 7.55 $Å^{-1}$. The amplitude of the second hump decreased at the expense of the first one with the decreasing size fraction. The third oscillation, was not well-defined for the <30kDa and <5kDa fractions but was composed of one peak at 9.05 $Å^{-1}$ for the 0.2µm-30kDa fraction that exibited an increasing shoulder with the increasing size fraction. The main peak in the Fourier transform was located at R + ΔR ~1.3 Å and corresponded to the first neighboring shell. With the decreasing size fraction, the wide of the first peak increased until reaching two separate peaks in <30kDa and <5kDa fraction at 1.07 and 1.56 Å, respectively. The 0.2µm-30kDa, <30kDa and <5kDa fractions exhibited two additional small peaks at R + ΔR ~2.4 Å and ~3.2 Å accounted for the second coordination shell neighbors. Whereas 5-3µm and 3-0.2µm fractions exhibited non-distinct peaks at R + ΔR ~2.2 Å, 2.5 Å and 3.0 Å. To explore the local As coordination, fits were performed in the 1-3.5 Å R-range (Figure III. 8). The fitted parameters and constraints for the references and each size fraction were reported in Table III. 1.

***First shell*.** The samples can be divided in two groups according to their first shell shape and fit. In the first group, composed by the largest fractions (i.e. 5-3µm, 3-0.2µm and 0.2µm-30kDa), between 3.6 and 4.3 O were necessary to accurately fit the first shell at a distance of 1.72-1.73 Å for both the 5-3µm and 3-0.2µm fractions and 1.77 Å for the 0.2µm-30kDa fraction. In the second group, composed of the smallest fractions, the two peaks were successfully fitted using two paths. The first one was As-O with 0.9 O at 1.74 Å and 0.8 O at 1.66 Å for <30kDa and <5kDa fractions, respectively. The second one was As-C with 4.4 C at 1.92 Å and 3.2 C at 1.97 Å for <30kDa and <5kDa fractions, respectively. The values for As-C distances were in agreement with Miot et al. (2008) who obtained an As-C distance at 1.91 Å, in AB compound.

These EXAFS results refined the XANES observations showing that methylated As species dominated in the <30kDa and <5kDa fractions but inorganic As persisted.

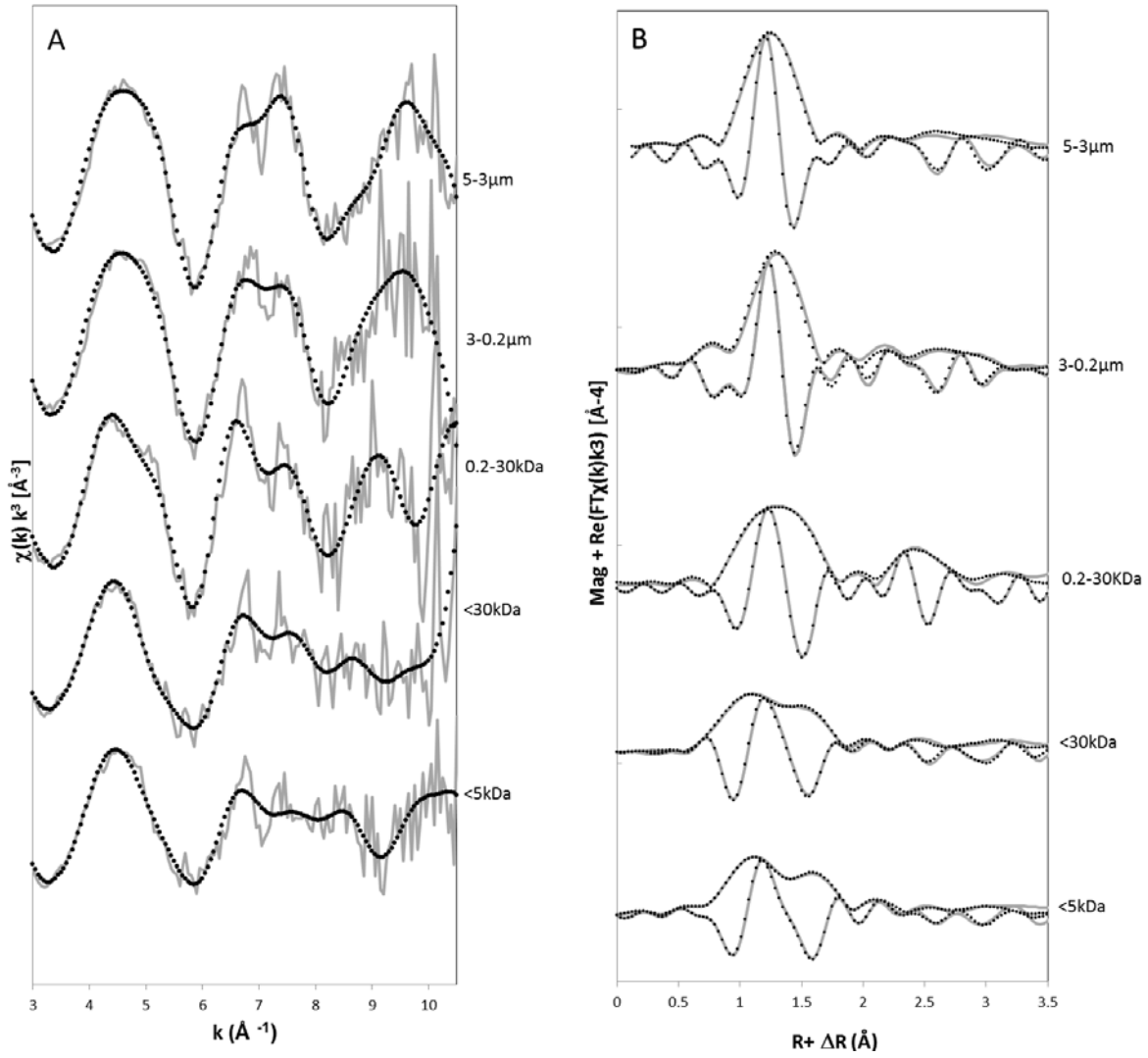

Figure III. 8 As K-edge EXAFS spectra, magnitude and imaginary part of the Fourier transform (uncorrected from phase shift) of the different fractions A) and B) respectively. The fit results, given as dotted lines, are superimposed onto the data in solid grey lines.

Table III. 2 Shell-Fit parameters determined from the As K-edge EXAFS spectra of the size fractions.

	As-O			As-C			As-(O)-C			As-Fe				
Sample	**N[a]**	**R[b] (Å)**	**σ^{2} [c]**	**N**	**R (Å)**	**σ^{2}**	**N**	**R (Å)**	**σ^{2}**	**N**	**R (Å)**	**σ^{2}**	**ΔE_0 [d]**	**R factor [e]**
5-3µm	4.3 (4)	1.72 (1)	0.003				1.7 (5)	2.85 (3)	0.003	1.2 (2)	3.35 (1)	0.010	6.93	0.006
3-0.2µm	3.7 (5)	1.73 (1)	0.007				2.1 (6)	2.86 (2)	0.004	1.0 (4)	3.33 (3)	0.009	8.62	0.013
0.2-30KDa	3.6 (8)	1.77 (2)	0.003							0.8 (5)	3.40 (4)	0.004	10.4	0.013
<30KDa	0.9 (1)	1.74 (6)	0.004	3.2 (4)	1.97 (4)	0.008				1.2 (2)	3.33 (4)	0.009	12.8	0.010
<5KDa	0.8 (2)	1.66 (9)	0.003	4.4 (2)	1.92 (6)	0.006				0.5 (1)	3.34 (3)	0.005	10.7	0.015

The amplitude reduction factor, S_o^2, was set to 1. [a]N, path degeneracy (coordination number); [b]R(Å), interatomic distance; [c]The Debye-Weller parameters were homogenized around a mean value; [d]Energy-shift parameter; [e]R-factor =$\Sigma i(data_i\text{-}fit_i)^2/\Sigma idata$. The Debye-Weller for the Fe-Fe paths are covaried with $\sigma^2As\text{-}Fe_1 = \sigma^2As\text{-}Fe_2$. The reported errors are determined by the fitting procedure.

Second coordination shell. An As-Fe distance was used to fit the second coordination shell for all the fractions. These distances varied between 3.33 and 3.40 Å. They were in agreement with distances reported for As(III) and As(V) monodentate binuclear corner-sharing complexes ^{2}C where As(III) and/or As(V) were bound to the apical O atoms of two edge-sharing FeO_6 octahedra (Waychunas et al., 1993; Manceau, 1995; Ona-Nguema et al., 2005). For 5-3µm and 3-0.2µm fractions, the residual between the fit and the spectra was high, suggesting the contribution of an additional neighbor in the second coordination shell. A path with interatomic As-Fe distance of 2.89 Å, corresponding to an As(III) edge-sharing complexes E^2 (Ona-Nguema et al., 2005), was tested. However the Debye-Weller of the fit was negative excluding this bonding. A second path As-C (via O binding) was tested. A better fit was obtained with a distance at 2.85 Å for 5-3µm fraction and 2.86 Å for 3-0.2µm fraction. The presence of other light atoms was also considered but finally ruled out because they would result in longer interatomic distances for Ca and Al (Arai et al., 2001; Bardelli et al., 2011) or shorter interatomic distance for S (Hoffmann et al., 2014).

III.3.6 Arsenic speciation using SEC-ICP-MS and HPLC-ICP-MS

The size separation of As reference materials was displayed in Figure III. 9A. The retention times of As references were 4.8 min for dissolved As(V), 5.3 min for MMA, 7.1 min for DMA and 9.8 min for dissolved As(III). The retention times of OM, Fe and As in <30kDa and <5kDa fractions were displayed in Figure III. 9B and C. The Fe signal derived from SEC-ICP-MS analysis was parallel to UV signal corresponding to organic molecules. They were both constituted of a peak at 4.35 min and a shoulder at 4.80 min. This coelution indicated that Fe and OM are associated in two closed sizes. No signals of dissolved As(III), MMA nor DMA were detected in both fractions. Arsenic signal followed the Fe-OM association signal. For the < 5kDa fraction, a small peak matched the main peak of the Fe-OM signal but a higher peak matched the Fe-OM signal shoulder. For the <30kDa fraction, two peaks quite similar in intensity were observed. The second peak at 4.8 min observed for As matched also with that of As(V) reference in solution (Figure III. 9A). Two hypotheses can be considered: i) all As

species were associated with Fe-OM aggregates which size corresponded to the 4.8-min retention time or ii) an As(V) portion remained in solution.

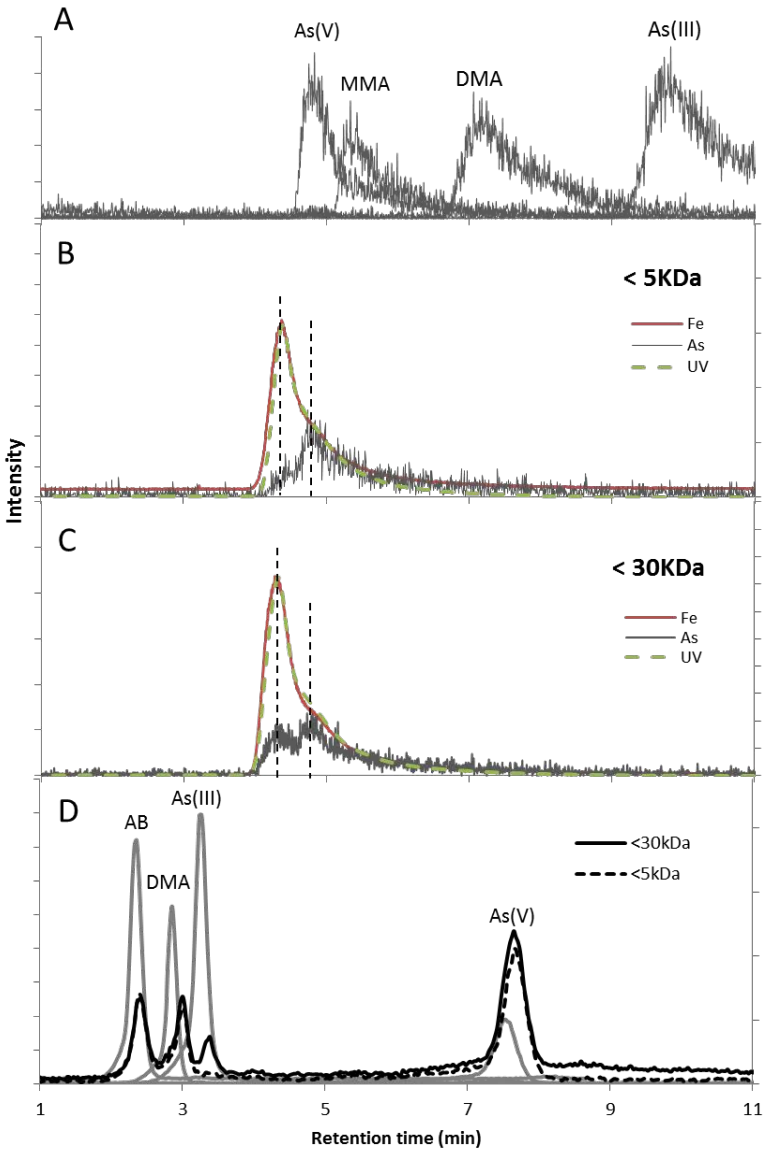

Figure III. 9 A: SEC-UV-ICP-MS chromatogram of reference As species, B and C: chromatograms of OM(corresponding to the UV), Fe and As for <30kDa and <5kDa fractions. Vertical dotted lines highlight the main features of the signals. D: HPLC-ICP-MS chromatograms of As reference species used for peak identification (grey lines) and <30kDa and <5kDa fractions (black lines).

Results from the HPLC-ICP-MS analysis are displayed in Figure III. 9D. The chromatograms revealed that As was mainly present as As(V) with a retention time of 7.6 min. Three others peaks were observed at 2.3, 2.9 and 3.3 min and were attributed to AB, DMA and As(III) dissolved in solution respectively. The amount of As(III) was much lower in <5kDa than in <30kDa fraction. Both

organic As species were methylated As(V). A systematic shift about 0.15 min was observed between the samples and each standard. It can be explain by the difference in the injected volume which was of 30 µL for the standard against 100 µL for both fractions. Neubauer et al. (2013) demonstrated that the retention time increases with the sample load. As the peaks were distant from each other, no misidentification was possible; the time shift was thus not corrected. The determination of each As species concentration was performed by injecting reference compounds at various concentrations. The calibration curves between the peak areas and concentrations are displayed in Annexe II. The estimation of each species recovery was estimated by directly injecting the sample in the ICP-MS and comparing both concentrations (Annexe II). The total recovery of the injected standard solutions was about 90%. However, the total recovery was only 65 % for <5kDa fraction and 32 % for <30kDa fraction, suggesting that a sample matrix effect through the column could have occurred.

It important to note here that HPLC-ICP-MS technique only allows detecting dissolved species. However, SEC-ICP-MS analysis showed that As species was co-eluted with Fe/OM associations, namely that As was bound to Fe/OM associations. The detection of As species by HPLC-ICP-MS could result in the As species release subsequent to a Fe/OM solubilization promoted by the presence of EDTA, being a strong complexing agent of Fe, in the mobile phase of the HPLC column. This hypothesis was confirmed by the detection of Fe in column solution outlet by ICP-MS measurements. The EDTA seemed to impact the release of inorganic and organic As species differently. Therefore, HPLC, here, only provided information on the presence /absence and relative proportion between each detected As species in the <30 kDa and 5kDa fractions.

III.4 Discussion

III.4.1 As speciation as a function of the size fraction

Our results evidenced that the speciation and distribution of Fe and As, as well as the composition of OM varied accordingly to the molecular size fractions of the oxidized soil solution.

5-3µm and 3-0.2µm fractions. As revealed by TEM images, the fractions were heterogeneous. Above 0.2 µm, a major mass fraction was composed of silicate, remain of plant stem and diatoms. The OM in both 5-3µm and 3-0.2µm fractions was composed of little degraded organic compounds originated from plants (i.e. leaves and roots remains) with a rich proportion of fatty acids. Iron was present as aggregates of nanoparticles embedded in OM (Table III. 2). The low degree of polymerization, evidenced by TEM and XAS analysis, could be explained by the high amount of OM which impair the crystal growth of Fe(III)-oxyhydroxides (Cornell and Schwertmann, 2003; Pédrot et al., 2011b). Scarce Fe well-formed crystals were supposed to be inherited from soil and therefore preserved from the reductive dissolution. Arsenic occurred mainly as As(V). A strong correlation existed between As and Fe concentrations (Figure III. 1A) indicating that most of As was associated to Fe particles and aggregates. The specific surface of nanoparticles aggregates was expected to be higher than the well crystallized Fe(III)-oxyhydroxides (Hiemstra and van Riemsdijk, 2007). Arsenic was therefore more likely to be bound as bidentate complex to Fe nanoparticles aggregates (Ona-Nguema et al., 2009). The As K-edge EXAFS revealed the presence of an interatomic distance As-C at 2.85 Å suggesting the presence of As as organic compounds probably inherited by the biological activities or matter. Several studies hypothesized the binding of As to OM carboxylic or phenolic sites (Redman et al., 2002 ; Buschmann et al., 2006). Buschmann et al. (2006) suggested the formation of As(V)-HA complex due to an additional chelation and stabilization effect. Dembitsky and Rezanka (2003) suggested that inorganic As was complexed to carboxylic groups during the uptake by the plants or fungi. The GC-MS analysis revealed also the presence of small amount of arsenobetaine (AB) whose low concentration did not allow to be evidenced by XAS (no As-C distance observed at 1.98 Å) which is an averaging tool. The large binding of As with Fe phase did not allow detecting As-C distance at 1.98 Å which was masked by the presence of high amount of stronger backscatterers Fe neighbors in EXAFS spectra (Table III. 2). Arsenobetaine was primarily found in marine environment but also showed to occur in terrestrial organism such as mushrooms, earthworms, plants and soils (Huang and Matzner, 2007). Its formation was considered to be a detoxification mechanism of

organisms (Tamaki and Frankenberger, 1992). Arsenobetaine was probably adsorbed to Fe(III)-oxyhydroxides, as previously observed for other As methylated species (Bowell, 1994; Cox and Ghosh, 1994). Methylated As could also be taken up by plants which translocate the As from the soil to their tissues (Hitbold, 1975; Geiszinger et al., 2002). Since in 5-3µm and 3-0.2µm fractions, OM appeared to be originated from plants, As methylated compounds could also be included in the plant remains.

0.2µm-30kDa fraction. This size fraction represented the most concentrated fraction in Fe and OM. Those distributions were consistent with the ultrafiltration analysis of the shallow groundwater of the wetland in which the present soil was sampled (Pourret et al., 2007). Pourret et al. (2007) noticed that most Fe occurred as Fe-OM colloids whose size ranged from 0.2µm to 30kDa. Here, the Fe was identified to occur as nanoparticles aggregated or dispersed in the OM matrix (Figure III. 3). Compared to the high molecular size fractions where carboxylic groups (within fatty acids) were dominant, the GC-MS analysis showed that OM in this fraction was mainly composed of lignin and tannin markers which are more enriched in phenol groups. The complexation capacity of the phenolic groups is stronger than carboxylic which implies a higher reactivity of this fraction toward metallic ions such as Fe (Tipping, 1998). Arsenic was present as a mixture of As(III) and As(V). Guénet et al. (2016) provided evidence that, in natural Fe-OM colloidal agglomerates, OM prevents total As(III) oxidation by controlling the Fe species as Fe monomer/small clusters and weakly polymerized Fe(III) oxyhydroxides. Arsenic reached its highest concentration and was strongly correlated with Fe in this fraction indicating the As was adsorbed by Fe(III) phases (Figure III. 1). Those results were supported by EXAFS measurements where As appeared highly bound to Fe. However, the THM-GC-MS analysis also detected the presence of AB.

<30kDa and <5kDa fractions. Iron concentration, unlike OC, strongly decreased in these fractions. Fe was almost removed after this ultrafiltration step. Iron formed small clusters as evidenced by the absence of Fe-Fe distance at 3.03 Å and the fitting of the Fe-Fe distance at 3.44 Å which corresponds to corner-sharing $Fe(O,OH)_6$ octahedra. The absence of a Fe(III)-oxyhydroxides

phase was consistent with the TEM images where no Fe-nanoparticles were observed. Clusters were embedded in an OM matrix as revealed by the interatomic distance Fe-C at 2.9 Å. Organic matter is able to strongly bind Fe(II, III) through its carboxylic or phenolic groups (Liang et al., 1993; Tipping et al., 2002; Catrouillet at al., 2014). The stability constant of Fe(III)-phenol complex, log K, is equal to 8.40 against 4.01 for Fe-acetate complex at ionic strength 0 (Sommer and Pliska, 1961; Desai and Milburn, 1969). Because, LMW OM was expected to contain more phenolic compounds, these fractions were highly reactive against Fe.

A weak correlation between As and Fe was calculated for this LMW fractions which suggested that As was be less associated with Fe phases. The HPLC-ICP-MS and XAS analysis revealed the presence of As organic species where oxidized As(V) was methylated as AB, MMA and DMA. In our experiment, the analysis of the soil solution before oxidation did not show any AB or DMA which are therefore produced during soil solution oxidation. Sohrin et al. (1997) observed in eutrophic lake a seasonal variation of methylated As species concentration produced under oxidative condition and decomposed to inorganic As under anoxic conditions. The presence of about 30% of methylated species combined with the AsO_4 presence explained the weak As/Fe correlation. However, As K-edge EXAFS spectra showed that a part of As was bound to Fe as monodentate binuclear corner-sharing complexes ^{2}C on the small Fe clusters. Considering the Fe-C distance at 2.8 Å as well as the As-Fe distance at 3.43 Å, ternary complexes were possibly formed in the LMW fractions (Mikutta and Kretzschmar, 2011; Sharma et al., 2011; Hoffmann et al., 2013) which was confirmed by the coelution of Fe, As and OM in the SEC-ICP-MS analysis.

III.4.2 Implications for As dynamic in wetland

In previous studies, Al-Sid Cheikh et al., (2015) and Guénet et al., (2016), from NanoSIMS analysis of agglomerate solids produced during oxidizing period in our studied wetland, showed that As distribution was highly heterogeneous with i) As associated to Fe-enriched zones and ii) As associated to OM-enriched but Fe-depleted hotspots. To explain this observed colocalizations of As and OM, Al-Sid-Cheikh et al. (2015) suggested the binding of a part of As as As(III) to OM thiol (SH-)

functional groups. Unfortunately, the present results did not support this assumption; no As-S distances were detected in EXAFS spectra for any size fractions, even in the lowest fraction. The association between As and OM must thus be explained by a new mechanism. The present results demonstrated the presence of significant amount of As as As(V) organic species notably in the large size fractions (between 5 and 0.2 µm) (Figure III. 2). These As(V) organic species sourced from plants and organisms did not directly depend on the prevailing redox conditions. Organisms detoxification processes activated by the production of dissolved As was the mechanism that most probably controlled these organic As(V) species production. A proportion of this organic As(V) species was scavenged in plants and organisms although a second part was probably excreted and subsequently adsorbed to Fe phases. The organic As(V) species in organisms residues might explained the colocalization of As and OM observed by NanoSIMS in the OM-enriched but Fe-depleted hotspots (Al-Sid Cheikh et al., 2015; Guénet et al., 2016).

Considering the wet mass of each fraction, about 92% of As (inorganic and organic) was situated in >0.2 µm fractions, namely in particulate fractions. Regards to these large sizes, such particles were not mobile since they could settle rapidly and easily. Larger ones can be regarded as soil own particles which have been suspended in solution by the experimental design. The present results demonstrated thereby that a large proportion of As was i) involved in biological mechanism and integrated in particulate biological materials and ii) bound to not mobile Fe particles (>0.2 µm particulate fractions). Both mechanisms promoted As trapping in the soil wetland. The 0.2µm-30kDa fraction was the most Fe-enriched phase. In such fraction, As speciation was mainly controlled by its binding to poorly ordered Fe(III)-oxyhydroxides. Ranging in the colloidal size, this fraction might be considered as mobile and able to transport As until rivers or aquifer along with water movement. About 6 % of As was in this size-fraction which was few regards to the larger size fraction. Finally, below 30 kDa fractions were mainly constituted of organic colloids and/or molecules. In this smaller size fraction, As was present as inorganic species (arsenite and/or arsenate) and as organic As(V) species. Both seemed to be bound to the colloidal phases either via direct interaction or via Fe

monomer or small clusters, in a ternary system, with organic colloids. Stolpe and Hassellöv (2007) demonstrated that, in aquatic systems, organic-rich colloids are more mobile than Fe-rich colloids subject to aggregation and sedimentation. This fraction represented 2% of the total As. For both 0.2µm-30kDa and <30 kDa fractions, As mobility will be controlled by the ability of colloids to be maintained in solution relative to their affinity with soil components and water flux in soil porosity where they were produced. A point that should be, however, further considered is the potential (bio)degradation of organic As(V) species as inorganic As(V) (Ritchie, 2004) although their binding to colloids should decrease their (bio)degradation.

These results shed a new light on the As dynamic control by wetlands. Wetland are often regarded as As sources for groundwater and/or river (Kocar et al., 2008; Polizzotto et al., 2008; Fendorf, 2010; Elisabeth Neubauer et al., 2013a, 2013b). However, these studies were mainly interested by the <0.2 µm fraction of water sample. They demonstrated that As was released in solution as labile inorganic species or bound to Fe/OM colloids. The present work showed that the most removable As was the As bound, not only as inorganic but also as organic species, to colloids whose size was <0.2 µm. The proportion (8%) of such As was low regards to the As contained in higher size fractions in which As speciation seemed to be controlled by biological activity and binding to particulate Fe-oxyhydroxides. Therefore, if riparian wetlands are able to produce labile As(III) under the reducing period (Takahashi et al., 2004; Fendorf, 2010), several mechanisms could however interfere in its transfer to river and aquifer and therefore limit As mobility. The most studied is the As bind to soil particulate or colloidal Fe(III)-oxyhydroxides, the latter, as showed here and elsewhere, being intimately associated to OM (Pokrovsky and Schott, 2002; Stolpe and Hassellöv, 2007; Elisabeth Neubauer et al., 2013a). A second mechanism concerns the As biological uptake (e.g for detoxification process) resulting in the production of organic As(V) species that can be scavenged by plants and organisms or bound to Fe(III) oxyhydroxides. Such As mobility decrease, subsequently to the establishment of oxidizing conditions, was previously discussed by Frohne et al. (2014) and Shaheen et al. (2016). The proposed mechanism was the precipitation of Fe(III)-oxyhydroxides and

subsequent As binding. However, the present results provided evidence that this process was not the sole and could not be the most important in riparian wetland.

III.5 Conclusion

This study highlighted the large variation of As speciation in the various size compartments of a suspension provided by the reoxidation of a riparian wetland soil solution. Three main product were evidenced: i) particulate biological material inherited from the soil biological activities, ii) Fe-OM-rich colloid with a size ranging from 0.2 µm to 30 kDa and ii) a OM-rich colloid below 30 kDa in which Fe was present as monomer or small clusters. The OM characterization revealed that fractions above 0.2 µm were mainly composed of fatty acid (with carboxyl groups) whereas < 0.2 µm fractions, lignin and tannin markers (with phenolic groups) were in majority. The 0.2µm-30kDa fraction corresponded to a transition phase in term of degradation and main functional group composition. Fraction < 30KDa were enriched in phenolic groups suggesting a higher affinity for Fe as confirmed by EXAFS records where Fe-C was detected in <30kDa fraction. Despite oxidizing conditions, a few amount of reduced inorganic As was still present in the sample. Arsenic occurred as As(III) or As(V) bound to Fe(III) as particulate, colloids or small clusters. Most surprisingly, methylated As(V) species were formed during the oxidation period and detected in all size fractions. These organic As(V) species are usually biologically produced and could be bound to Fe(III), as particulate, colloids or cluster, to colloidal OM or remained integrated in the soil biological residual material.

This studies provided evidence that As was in majority distributed in the high size fraction (>0.2 µm), namely in the no transferable fractions of the suspension. Only 8% of As was present in smaller fraction expected to be removable. An important issue was also the identification of the importance of the biological activity in the immobilization of As in riparian wetland soils.

Chapitre IV. Caractérisation de nano-agrégats Fe-matière organique par un couplage SAXS/SANS et XAS : impact sur les processus d'adsorption de l'As

Dans la deuxième partie de ce travail, j'ai montré qu'une part importante de l'As produit en période de réduction pouvait être immobilisé, après une étape d'oxydation, via des processus biologiques et géochimiques dans la fraction particulaire d'un sol de zone humide. Cette étude a cependant mis en exergue le rôle que pourrait avoir la fraction comprise entre 0,2 µm et 30 kDa dans la mobilité de l'As. De toutes les fractions non particulaires, c'est-à-dire < à 0.2 µm, la fraction 0,2 µm-30 kDa est la fraction la plus riche en As. Le Fe y est sous forme de nano-oxydes et de polymères fortement associés à la MO probablement sous forme d'agrégats nanométriques. Les analyses spectroscopiques au seuil K de l'As ont montré que dans cette fraction, l'As était principalement associé à la partie ferrique de ces agrégats. Etant donné leur importance, il est donc crucial de mieux caractériser ces agrégats nanométriques et d'identifier l'impact que peut avoir leur structure sur les processus d'adsorption de l'As. En effet, leur capacité de sorption dépend de la densité de sites disponibles pour l'As. Or, cette densité est fortement dépendante de la surface spécifique, du taux de recouvrement entre surfaces, etc… autant de points que je vais développer dans cette troisième partie.

Ce chapitre correspond à un article qui sera soumis prochainement dans Langmuir : Characterization of iron-organic matter aggregates network by a combination of SAXS/SANS and XAS: impact on the As binding, Hélène Guénet, Mélanie Davranche, Delphine Vantelon, Julien Gigault, Sylvain Prévost, Olivier Tâché, Sebastian Jaksch, Mathieu Pédrot, Vincent Dorcet, Jacques Jestin

Characterization of iron-organic matter aggregates network by a combination of SAXS/SANS and XAS: impact on the As binding

RESUME

Les agrégats de taille nanométrique jouent un rôle important dans le contrôle de la mobilité des polluants tels que l'arsenic (As) dans l'environnement. Dans les solutions de sols, ces agrégats peuvent être constitués de matière organique (MO) associée au fer (Fe). Cependant, il existe un réel manque de connaissances sur la structure de ces agrégats nanométriques et notamment, sur l'organisation des composés dans le réseau. Or, de cette structure dépendent la réactivité de surface et la capacité de sorption de ces agrégats vis-à-vis des métaux et des métalloïdes. Nous avons choisi de synthétiser des agrégats nanométriques à partir de Fe(II) et d'acide humique, ces derniers étant représentatifs de la matière organique naturelle. Dans une seconde étape, nous avons réalisé des expériences de complexation d'As sur ces agrégats synthétiques. Le choix de l'As a été guidé par sa toxicité et sa forte affinité pour le Fe. L'influence de différents rapports Fe/carbone organique (CO) (mg/mg) situés dans la gamme des rapports naturels a été étudié. En couplant les techniques de diffusion de neutrons et de rayons-X aux petits angles (SANS, SAXS) avec des techniques d'absorption des rayons-X (XAS), nous avons montré qu'il existe une organisation fractale du Fe dans la matrice organique. Des billes primaires de 0,8 nm sont associées pour former des agrégats intermédiaires dont le rayon augmente de 3,3 à 5,7 nm lorsque le rapport Fe/CO varie de 0,1 à 0,4. Ces agrégats intermédiaires peuvent soit être isolés dans la matrice organique non agrégée soit constituer des

agrégats secondaires dont les rayons géométriques augmentent de 131 nm à 689 nm avec le rapport Fe/CO. Ces agrégats secondaires renferment en leur sein un agrégat de MO sphérique et compact dont le rayon géométrique varie de 90 nm à 136 nm entre les rapports Fe/CO. Etonnamment, alors que la surface spécifique (S/V) du Fe reste constante, l'adsorption de l'As augmente. Par analyse des courbes de diffusion et observations par microscopie électronique à transmission (MET), cette augmentation de sorption pourrait être reliée à une augmentation des distances entre les agrégats intermédiaires formant les agrégats secondaires, résultant d'une augmentation des forces de répulsion avec le rapport Fe/CO. La conséquence directe est un accroissement de la densité de site de complexation disponible pour la sorption de l'As. Cette augmentation de la sorption pourrait aussi être liée à une chute du taux de recouvrement des sites de sorption de l'As dans l'agrégat secondaire. Avec l'augmentation des rapports Fe/CO, la taille des agrégats de Fe et leur ramification augmentent plus fortement que celle de l'agrégat organique entrainant en conséquence une chute du taux de recouvrement des agrégats de Fe par l'agrégat organique. Cette étude offre un regard nouveau sur l'impact de la structure des réseaux formés entre les différents composants des agrégats nanométriques hétérogènes sur leur capacité de sorption. Ils pourraient expliquer certains résultats obtenus pour des solutions naturelles dont les rapports Fe/CO varient temporellement et spatialement.

ABSTRACT

Nanometric aggregates play an important role in controlling the mobility of pollutants such as arsenic (As) in the environment. In natural waters, aggregates can be constituted of organic matter (OM) associated with iron (Fe). However, little is known about their network structure, especially the role of each component on the resulting aggregate morphology. This network structure can be of major importance for the metal and metalloid sorption processes. We synthesized model aggregates by varying Fe/organic carbon (OC) ratio. By coupling Small Angle

Neutron and X-rays Scattering (SANS, SAXS), Dynamic Light Scattering (DLS), Transmission Electronic Microscopy (TEM) and X-rays Absorption Spectroscopy (XAS) techniques we revealed that the Fe organization follows a fractal modelling in the presence of OM. Primary beads of Fe of 0.8 nm associate to form intermediate aggregates whose radius increases from ~3 to 6 nm between the Fe/OC ratio R= 0.1 to 0.4. These intermediate aggregates compose large scale secondary aggregates whose radius increases from ~100 nm to 700 nm with the Fe/OC ratio. The OM part of the aggregates, only visible with SANS and contrast variation method, shows a dense single size component of typical radius equal to 100nm whose size and density slightly increase with the Fe/OC ratio. Surprisingly, as the characteristic sizes of the aggregates increase, the overall specific surface (S/V) of the system stays rather constant while the As adsorption increases. We first hypothesized that with the increasing Fe/OC ratio, the repulsion interactions between the intermediate aggregates within the secondary large scale structure increase inducing a structure opening and a subsequent increase of the number of available As binding sites. A second hypothesis concerned the coating rate of the Fe part of the secondary aggregate by the OM part. With the increasing Fe/OC ratio, the Fe part size increases more strongly and was more ramified than the OM part. The coating therefore decrease and the As binding site availability increase. This study offered new perspectives on the impact of network structure formed between the various components of heterogeneous nano-aggregates on their sorption capacity. They could explain some metal/metalloids sorption variations observed in natural samples with the temporal and spatial variations of the Fe/OC ratios.

IV.1 Introduction

In aqueous environment including surface waters, soil pore water and groundwater, aggregates of nanoparticles were widely observed (Kretzschmar and Schäfer, 2005; Pokrovsky et al., 2005; Pédrot et al., 2008; Bauer and Blodau, 2009; Ilina et al., 2013). Usually defined as particles in suspension smaller than about 1µm, such small aggregates exhibit a high specific area involving a high reactivity regards to metallic micro-pollutants (metals or metalloids) sorption. They are mainly

formed of more or less combined nano-sized minerals (e.g. clays, Fe, Al, Mn or Si oxides and hydroxides, carbonates, phosphates), and organic molecules/particles (e.g. humic and fulvic acids) (Buffle et al., 1998; Kretzschmar and Schäfer, 2005). Their complexity and heterogeneity also concerned the organisation of the network structure between minerals and OM molecules. Jarvie and King, (2007) showed from small angle neutron scattering (SANS) analysis that natural nano-aggregates extracted from river waters have a fractal organization with 3D network-type structures mediated by the OM presence. They suggested the existence of 3 characteristic length scales i) primary particles (3-10 nm), ii) small aggregates (20-50 nm) and iii) transient network of the aggregates (50-200 nm). Unfortunately, they did not detail the elemental composition (Si, Al, Fe, etc.) and OM amount of their natural nano-aggregates making difficult to transpose their data to other systems.

However, the knowledge of the network structure of small aggregates is essential to better understand the sorption mechanisms of micro-pollutants. The binding sites available for sorption are indeed strongly dependant on the spatial organisation between the various components of heterogeneous aggregates. As an example, an important coating between components could decrease the density of available binding sites and the subsequent sorption of micro-pollutants or modify their surface charge. In many studies dedicated to metal sorption in heterogeneous systems, geochemical models failed to reproduce experimental datasets (e.g. (Vermeer et al., 1998; Lippold and Lippmann-Pipke, 2009; Janot et al., 2013). The reason is that models predict sorption through stability constants, determined for single phases, which do not allow describing interactions between each component of the heterogeneous system (Vermeer et al., 1998; Weng et al., 2009; Reiller, 2012).

Assess the natural small aggregates network is however not trivial regards to their composition heterogeneity. Natural low amounts that generally require a concentration step as well as the sampling procedure are indeed likely to modify the aggregation. It is therefore necessary to firstly study synthetic model systems. Aggregates composed of Fe and OM are good candidates for

such model systems. They were identified in several natural areas such as wetlands in which they are produced by redox cycle and boreal system in which they are produced by permafrost thawing (Pokrovsky et al., 2005; Dahlqvist et al., 2007; Pédrot et al., 2008; Pokrovsky et al., 2011; Al-Sid-Cheikh et al., 2015). Several X-ray absorption studies characterized Fe speciation in such Fe/OM aggregates. Relative to the Fe/OM ratio, several Fe(III) phases seem to coexist as sorbed mononuclear complexes, polymeric clusters and nano-oxides (Buffle et al., 1998; Mikutta and Kretzschmar, 2011; Karlsson and Persson, 2012; Guénet et al., 2016). Finally, Fe oxyhydroxides and organic matter are well known to be strong sorbents of metallic micro-pollutants (Stumm et al., 1996).

Thereby, to gain information on the potential control of small aggregates network structure on micropollutants sorption, we chose to combine the study of synthetic Fe-OM aggregates structural organisation with sorption experiments of arsenic (As). Beside As is recognised to be a strong toxic pollutant, As was interesting, here, regards to its high sorption affinity for Fe(III) as compared to the OM. This contrasted binding affinity should allow identifying the impact of Fe(III) spatial, chemical and physical structure variations (influenced by OM) on the As sorption mechanism. Moreover, several studies showed that Fe-OM aggregates might be important controlling factor of As mobility in environment (Ryan and Elimelech, 1996; Mikutt-a and Kretzschmar, 2011; Sharma et al., 2011; Guénet et al., 2016; E. Neubauer et al., 2013). We therefore synthesized Fe-OM aggregates as model aggregates, using a standard humic acid, at different Fe/OC ratios and performed subsequent As sorption experiments. To get information on size, shape, elemental composition and network structure, the aggregates were study using neutron and X-Ray small angle scattering (SANS and SAXS), neutron contrast variation, DLS, TEM and X-rays absorption spectroscopy (XAS) at Fe K-edge.

IV.2 Experimental method

IV.2.1 Synthesis of mixed Fe-OM aggregates

All of aqueous solutions were prepared with analytical grade Milli-Q water (Millipore).Iron-OM aggregates were synthesized at different Fe/OC ratios (wt/wt) (i.e. 0.05, 0.1, 0.16, 0.23, 0.3, 0.4) using Leonardite humic acid (HA) from IHSS: C = 63.81%, O = 31.27%, H = 3.70%, N = 1.23% (as a mass fraction). Iron(II) stock solution of 1000 mg L^{-1} was prepared with $FeCl_2.4H_2O$, (Sigma Aldrich) in 0.01 M HCl and was progressively added at 0.05 mL min^{-1} using an automated titrator (Titrino 794, Metrohm) to an HA suspensions at an ionic strength of 5 10^{-3} mol L^{-1} of NaCl. The HA concentration was determined, relative to the concentration of the organic carbon (OC) in the suspension, in order to obtain the required Fe/OC ratios at the end of the titration. The pH was continuously maintained at 6.5 by progressively adding 0.1 mol L^{-1} NaOH (from Fisher Chemical) using a second titrator used in a pH state mode (Titrino 794, Metrohm). The accuracy of the pH measurement was ± 0.04 pH units. At the end of synthesis, the suspensions were left at least 30 min in contact with the atmosphere to ensure the stabilization of the pH at 6.5. The final concentration of Fe(II) and OC as well as the added volume of NaOH are reported in the Table IV. 1.

Table IV. 1 Concentrations in Fe and OC in the samples at different Fe/OC ratios with the added NaOH volume

Sample	Fe mg L^{-1}	OC mg L^{-1}	NaOH added (mL)
R=0.05	43.58	871.6	0.75
R=0.1	97.16	972.3	1.19
R=0.16	138.03	852.69	2.14
R=0.23	202.73	886.45	3.74
R=0.3	227.01	753.39	6.14
R=0.4	282.68	716.7	12.7

IV.2.2 SANS, SAXS and XAS standard synthesis

The HFO sample was prepared using the following procedure (Wilkie and Hering, 1996). A 0.1 M KOH stock solution was added dropwise with stirring to 500 mL of 0.05 mol L^{-1} $Fe(NO_3).9H_2O$. The

pH reached a value of approximately 8 with the addition of 350 mL of 0.1 M KOH to ensure total Fe hydrolysis (Wilkie and Hering, 1996). A volume of 0.6 mL of a 0.05 M Na_2AsO_2 stock solution was added to obtain the desired concentration of 2 g L^{-1} and 11 mg L^{-1} for Fe and As respectively. The HFO suspension was aged for at least 24 h with stirring. The suspension was then washed three times with deionized water using centrifugation and dialyzed with 12-14 KDa cellulose membrane during 48 h. The HA suspension was prepared using the Leonardite HA whose pH was fixed to 6.5 with a ionic strength at 5 10^{-3} mol L^{-1} of NaCl.

IV.2.3 Chemical analysis

Dissolved organic carbon (DOC) concentrations were measured using an organic carbon analyzer (Shimmadzu TOC-V CSH). The accuracy of the DOC measurements was estimated to be at ± 5% by using a standard solution of potassium hydrogen phthalate (Sigma Aldrich). The Fe and As concentrations were determined by ICP-MS using an Agilent technologies 7700x at the University of Rennes 1. The samples were pre-digested twice with 14.6 N HNO_3 at 90°C, evaporated to complete dryness and then resolubilized with HNO_3 at 0.37 mol L^{-1} to avoid any interference with the DOC during the analysis. A flux of He was injected in a collision cell to remove interferences from $^{40}Ar^{35}Cl/^{75}As$ and $^{40}Ar^{16}O/^{56}Fe$. Quantitative analyses were performed using a conventional external calibration procedure (seven external standard multi-element solutions, Inorganic Venture, USA). Rhodium-Rhenium was added on-line as an internal standard at a concentration level of 300 ppb to correct for instrumental drift and possible matrix effects. Calibration curves were calculated from the intensity ratios of the internal standard and the analyzed elements. The international geostandard SLRS-4 was used to control the accuracy and reproducibility of the measurement procedure. The instrumental error on As and Fe analysis was below 3%. The chemical As and Fe blanks were lower than the detection limits (respectively 0.003 and 0.07 µg L^{-1}), no correction was thus needed.

IV.2.4 SANS and SAXS/WAXS analysis

Small-angle neutron scattering (SANS) were performed on the KW-S1 beamline operated by FRM II at the Heinz Maier-Leibnitz Zentrum (MLZ), Garching, Germany. The samples were held in 1 mm thick quartz cells. Three sample-to-detector distances (2, 8, 20 m) were used with a wavelength of λ = 7 Å. These conditions gave access to a momentum transfer range, q, from 1×10^{-3} to 2×10^{-1} $Å^{-1}$. All data were corrected for detector sensitivity, background noise and sample holder contributions according to standard data contribution handling procedures (Brûlet et al., 2007). Data were also acquired on the PACE beamline (LLB, Saclay, France) where three configurations were used: two sample to detector distances of 1 and 4.7m combined with two wavelengths 6 and 17 Å that enable to cover a q range between 3×10^{-3} - 0.3 $Å^{-1}$.

Wide angle X-ray scattering (WAXS) were performed on the MOMAC spectrometer (CEA-LIONS, LPS-Orsay, France). The instrument uses a molybdenum X-rays source, which produces a beam with a much higher penetration length than X-rays generated by a classic copper source. The selected instrumental configuration used a wavelength of 0.709 Å and a sample-to-detector distance of 72.10 cm. This set-up allowed measuring a q range of 0.03 to 3.6 $Å^{-1}$. To explore a smaller q range, synchrotron small-angle X-ray scattering (SAXS) experiments were conducted at the European Synchrotron facilities (ESRF) at Grenoble, France, on the ID02 beamline. The detector used was the CDD Rayonix MX170-HS with a wavelength of 10.8 nm. The samples were held in quartz capillaries of internal diameter of 1.4 mm (10µm thick) with a sample-to-detector distance of 5 m and 30.7 m. This set-up allowed access to a q range of 2.6×10^{-4}-1.1 10^{-1} $Å^{-1}$.

IV.2.5 Dynamic Light Scattering (DLS)

In order to confirm SANS/SAXS measurements and investigate the predominant aggregate size, Fe-OM aggregates were investigated with DLS technique. The Fe-OM aggregate suspension at a Fe/OC ratio of 0.4 was prepared as described in 2.1 section. Arsenic was added to reach a As/Fe ratio of 0.005. After 24h of stirring, the suspension was fractionated at several cut-size (i.e. 200 nm, 1000 kDa, 100 kDa and 30 kDa).

The Dynamic Light Scattering instrument used was a Vasco Flex (Cordouan Technology, France) which allowed analyzing particles directly into the solution. Each measurement corresponded to six replicates with 90 s of acquisition in order to obtain convenient and stable auto-correlation curves. A delay time of 10 µs associated to 400 channels was sufficient to obtain information on the smallest size while a number of 800 channels were used to analyze the largest colloidal particles. A control experiment was systematically performed and consisted to the same experimental conditions using polystyrene standards (Thermofisher, USA). The whole experiment was replicated several times. The presented data were a mean of this six replicates. No bias was identified in the measurements.

IV.2.6 XAS analysis of the aggregates

IV.2.6.1 XAS Data collection

A fraction of each Fe-OM aggregates were freeze dried. The obtained powders were pressed into 6 mm pellets mixed with cellulose to obtain an edge jump of 1. Iron K-edge spectra of aggregates and HFO reference were recorded on the LUCIA beamline (Flank et al., 2006) of the SOLEIL Synchrotron (St Aubin, France). The monochromators used were Si(111) crystals. They were calibrated setting the first inflection point of the K-edge of an Fe foil to 7112 eV. Spectra were collected in transmission mode using a Silicon Diode with a macro beam of 2 mm. To prevent beam-induced redox changes, samples were maintained under vacuum, at 150K using a liquid nitrogen cryostat.

IV.2.6.2 XAS data analysis

Iron XAS spectra were extracted using the Athena software (Ravel and Newville, 2005) including the Autbk algorithm (Rbkb = 1, k-weight = 3). Normalized spectra were obtained by fitting the pre-edge region with a linear function and the post-edge region with a quadratic polynomial function. The Fourier transform of the k^3-weighted EXAFS spectra were calculated over a range of 2-11 $Å^{-1}$ using a Hanning apodization window (window parameter = 1). Back Fourier filters were extracted over the R-range of 1-3.5 Å, using the same apodization window shape. EXAFS data were

analyzed by shell fitting using the software code Artemis (Ravel and Newville, 2005). Theoretical back scattering paths for the fits were calculated from goethite (Hazemann et al., 1991), and Fe-carboxylate (Horcajada et al., 2007). Shell-fit analyses were performed within the 1-3.5 Å. The best fit was chosen by minimizing the reduced χ^2 which depends on the number of independent parameters, the number of fitted parameters and the uncertainty of the data points.

IV.2.7 Transmission electron microscopy (TEM) analysis of Fe-OM aggregates

A drop of each synthetic colloid was deposited on a 300 mesh copper grid coated with a lacey carbon film (Oxford Instruments, S166-3) and dry at room temperature. Regards to its thin, this support was well suited for the observation of nanoparticles in high resolution. High Resolution Electron Microscopy (HREM) investigations were performed on a TEM with a JEOL 100CXII instrument (voltage 100 kV) (THEMIS Analytical Facility at the University of Rennes 1). The elemental composition of Fe in Fe-OM aggregates was determined with a JEOL 2100F (voltage 200 kV) equipped with an X-ray energy dispersive spectroscopy (XEDS) detector (Kevex detector with an ultrathin window).

IV.2.8 Sorption experiments

Arsenic (III) stock solution at 38 mg L^{-1} was prepared with Na_2AsO (Fluka Analytical). Adsorption experiments were performed in triplicate by adding aliquots of As(III) stock solution to 3 Fe-OM aggregates (i.e. at 0.10, 0.23 and 0.3 Fe/OC ratios). Two As/Fe ratios were used, one at 0.18 (wt/wt) which corresponded to a mean ratios used in literature and ensured a strong As adsorption (Dixit and Hering, 2003). A second As/Fe ratio at 0.005 was representative of the As/Fe ratio determined in riparian wetlands soil solution under high water period (namely, for the strongest As concentration) (Dia et al., 2000; Olivié-Lauquet et al., 2001). Grafe et al., (2001) showed that As adsorption equilibrium onto goethite in presence of HA was reached at around 5h. The steady state for As adsorption were determined at 4h for HFO and 24 H for goethite or magnetite, respectively (Pierce and Moore, 1982; Manning et al., 1998). In the present experiment, the suspensions were

therefore stirred for 24 h to reach equilibrium. Fifteen mL of solution were sampled and ultrafiltrated at 2 kDa (Vivaspin VS15RH12, Sartorius) by centrifugation at 2970 g for 30 min. The cutoff threshold of 2kDa allowed separating the truly dissolved species from As adsorbed onto Fe-OM aggregates. Ultracentrifugation cells were previously washed with Milli-Q water to obtain a DOC concentration below 0.2 mg L^{-1} in the ultrafiltrate. Concentrations of As, Fe and DOC were measured in the bulk suspensions and in the ultrafiltrates (i.e. fraction < 2 kDa). Considering this cut size, allowing to retain all As bound to aggregates, the adsorbed As percentages were calculated following this equation (Eq. 1):

$$\%As_{adsorbed} = 100 - \left(\frac{[As]_{<2KDa}}{[As]_{total}} \times 100 \right) \quad \text{(Eq. 1)}$$

No Fe was measured in the fraction <2 kDa confirming the efficiency of this cut-off.

IV.3 Results

IV.3.1 Aggregates conformation relative to the Fe/OC ratio

IV.3.1.1 Neutron and X-ray scattering results

We performed contrast variation method with SANS to characterize the morphology of the Fe-OM aggregates. The scattering intensity of a colloidal solution of scattered species dispersed in a continuous solvent can be written as (Eq. 2):

$$I(q)=\varphi V \Delta\rho^2 P(q) S(q) \quad \text{(Eq. 2)}$$

With φ and V the volume fraction and the volume of the scattered entities, $\Delta\rho^2$ is the contrast term, namely the square of the difference between the scattering length density (SLD) of the scattered species and the solvent SLD, here the water. P(q) and S(q) are the form and the structure factors. For a dilute solution, the interactions between the objects are negligible and the resulting structure factor tends to unity. The remarkable interest of the neutron-nucleus interaction is it dependency of the isotopic constitution. The SLD of the solvent can be varied for different volume ratios of protonated H_2O and deuterated water D_20 along a broad scale ranging from pure H_2O, SLD=-0.56 10^{10} cm^{-2} and pure D_2O, SLD=6.4 10^{10} cm^{-2}. Then, the principle of a contrast variation

experiment is to change this ratio for a given scattered volume fraction. The scattering intensity is only dependent on the contrast term according to Eq. 3:

$$\Delta\rho=[I(q)/\varphi VP(q)]^{1/2} \quad \text{(Eq. 3)}$$

We performed these experiments on the components of the Fe-OM aggregates, a pure hydrous ferric oxide (HFO) using 6 H_2O/D_2O ratios (5, 13, 25, 50 and 75 and 100% vol) and the Leonardite humic acid (HA) using four H_2O/D_2O ratios (25, 50, 75 and 100% vol). In the Figure IV. 1a and 1b, the variation of the contrast term are reported as a function of the H_2O/D_2O ratio for a given q value ($q^*=6.88\ 10^{-3}$ Å^{-1}). For the HFO, continuous decrease intensity was observed with the decreasing H_2O content indicating that the HFO SLD was close to that of D_2O. This variation was consistent with the high density and the high SLD of HFO. Even if it was difficult to fully exchange HFO in D_2O, its contribution could be however almost matched in the ratio of 5/95% vol H_2O/D_2O corresponding to the minimum of the parabolic variation in Figure IV. 1a.

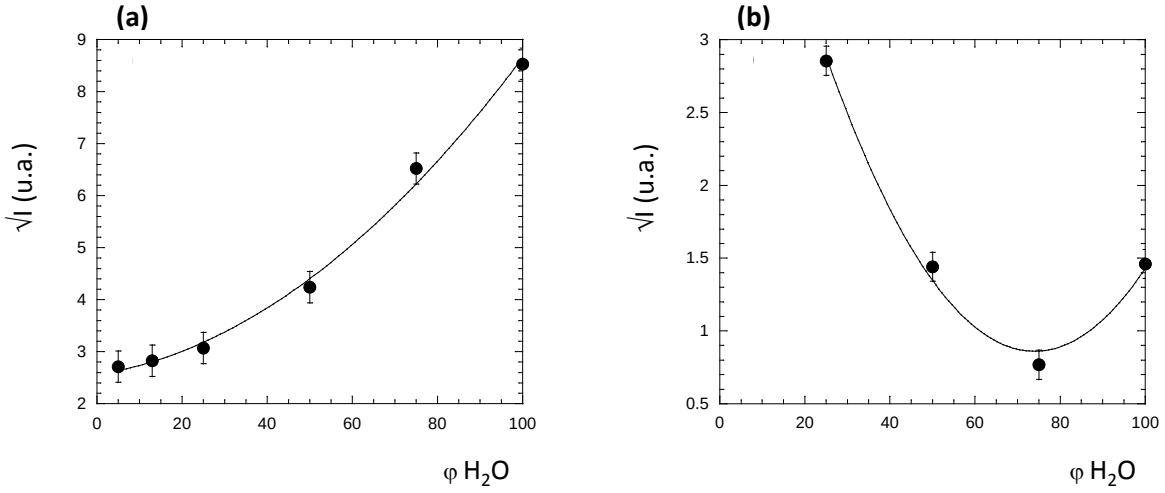

Figure IV. 1 Variation of the SANS intensity according to the equation 2 at a given q value $q^*=6.88\ 10^{-3}$ Å^{-1} as function of the H_2O/D_2O ratio for (a) HFO and (b) HA (Leonardite). The line is a polynomial curve as a guide for the eyes.

The Figure IV. 1b exhibited a nice parabolic minimum illustrating the HA matching point for a H_2O/D_2O ratio equal to 75/25% vol., corresponded to a contrast value of SLD=$1.18\ 10^{10}$ cm^{-2}. This result was promising because the difference between the two optimal values was large enough ($SLD_{HA}=1.18\ 10^{10}$ cm^{-2} *versus* $SLD_{HFO}=6.05\ 10^{10}$ cm^{-2}) to separate the contribution of both components

of Fe-OM aggregates in the total scattering intensity. Then HFO and HA were measured with SANS for the optimal contrast match values, namely at the H_2O/D_2O ratio of 75/25% vol. and 5/95% vol. for HA. The HA SANS curve was displayed in Figure IV. 2. The scattering curve can be modeled using simple functions separated by a cut off value. For the low q domain and $q<q_{cut\text{-}off}$, the so-called Guinier approximation was used (Guinier and Fournet, 1955) (Eq. 4) :

$$I(q) \sim I_0 \exp(-q^2 R_g^2/3) \qquad \text{(Eq. 4)}$$

Where I_0 is the pre-factor corresponding to the extrapolation of the intensity when $q \rightarrow 0$ and R_g the radius of gyration corresponding to a typical size of the system independent of geometrical hypothesis. The Guinier log-log representation was plotted in Figure IV. 2 with the red full curve. We calculated a radius of gyration equal to $R_{g\ HA}$ = 85 nm illustrating the size of the HA object. The corresponding geometrical spherical radius can be calculated using $R_g^2=3/5R^2$ and with $R_{HA}=110 \pm 16$ nm. For $q>q_{cut\text{-}off}$ in the intermediate and high q domain, the scattering is dominated by a power law function (Eq. 5) (Teixeira, 1988):

$$I(q) \sim q^{-Df} \qquad \text{(Eq. 5)}$$

Where D_f is the mass fractal dimension of the object illustrating the compactness of the objects.

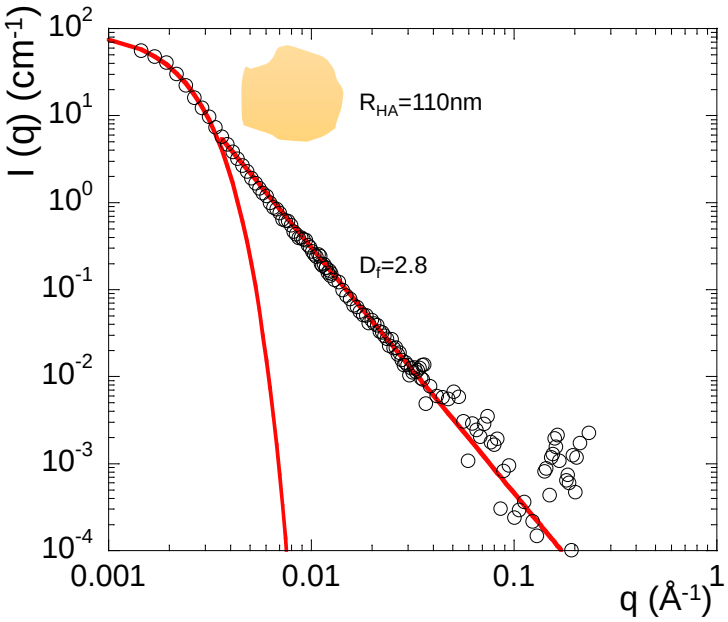

Figure IV. 2 SANS curve of HA dispersed in a solution of 5/95 vol. % H_2O/D_2O.The red lines are the Guinier and the power law determination (Eq. 3 and 4), the sketch represent the HA object.

This was highlighted in the Figure IV. 2 by the straight red line decrease of the scattering intensity with a characteristic exponent corresponding to a fractal dimension equal to $D_f = 2.8 \pm 0.4$ for the HA object. The value of the fractal dimension close to 3 indicated that the HA objects were compact structure.

We turn now to the characterization of the iron oxide component (HFO). An additional interesting approach in terms of scattering contrast is to combine neutrons and X-ray experiments. The X-ray contrast is indeed only depending of the electronic density of the element and is significantly higher for the HFO component compared to HA. Then the SAXS was measured for HFO and combined with the SANS curve, determined for a ratio H_2O/D_20 equal to 75/25 % vol., after renormalization with the contrast. The resulting SANS/SAXS combination was reported in Figure IV. 3. A different shape of the scattering curve than for the previous HA was observed with two characteristics shoulders respectively at high and low q indicating two different sizes. To analyze this curve, a fractal model was used. This model is commonly found for silica particles dispersed inside a polymer matrix for nanocomposites or filled elastomers. We started with a primary bead described with a spherical poly-dispersed form factor (a sphere radius R_0 and a log normal distribution of the sizes σ). The primary beads arranged according to a finite number of particles N and a fractal dimension D_f to form a primary aggregate also described by a radius R. In addition, we implemented a Percus-Yevick function (Robertus et al., 1989) traducing the interaction between the primary beads inside the primary aggregate according to a typical center to center distance d_0.

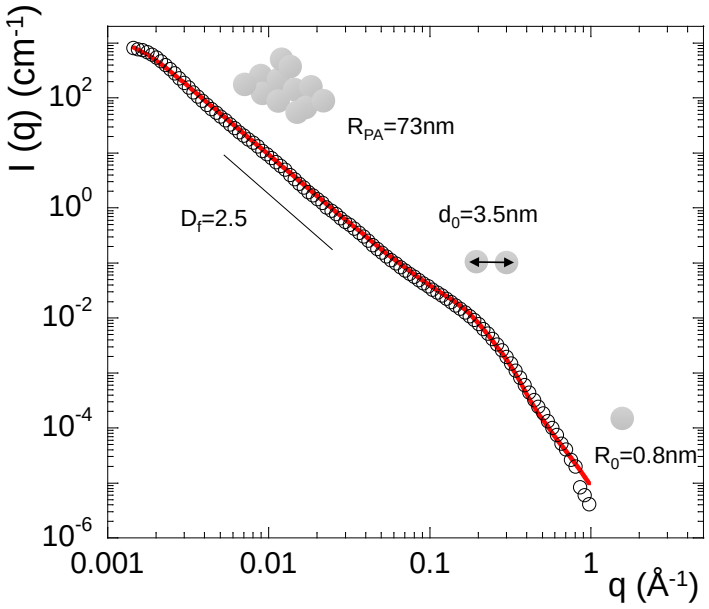

Figure IV. 3 Combined SANS (75/25 H_2O/D_20 % vol.) and SAXS for the HFO component. The red line is the fit of the fractal aggregate described in the text. The sketches illustrate (right to left): i) the primary spherical bead, ii) the interaction between the beads and iii) the primary aggregate made from the assembly of a finite number of primary beads.

The scattering curve was perfectly described by the model whose parameters were reported in Figure IV. 3. We found the best agreement for a primary bead of R_0=0.8 ± 0.12 nm and a log normal dispersion σ=0.3, an interaction distance d_0 between primary beads of 3.5 ± 1 nm and an aggregation number of 8 10^4 ± 1 10^4, a fractal dimension of D_f= 2.5 ± 0.3 corresponding to a radius of primary aggregates R_{PA} = 73 ± 10 nm.

To summarize the characterization of the pure components, the HA component was a single size compact structure while HFO was ramified primary aggregates resulting from the assembly of primary beads.

Following the characterization of the pure components, the contrast variation was applied to the Fe-OM aggregates with various Fe/OC ratios. One example of the variation of the SANS scattering as a function of the H_2O/D_2O ratio was displayed in the Figure IV. 4 for a Fe/OC ratio of 0.3.

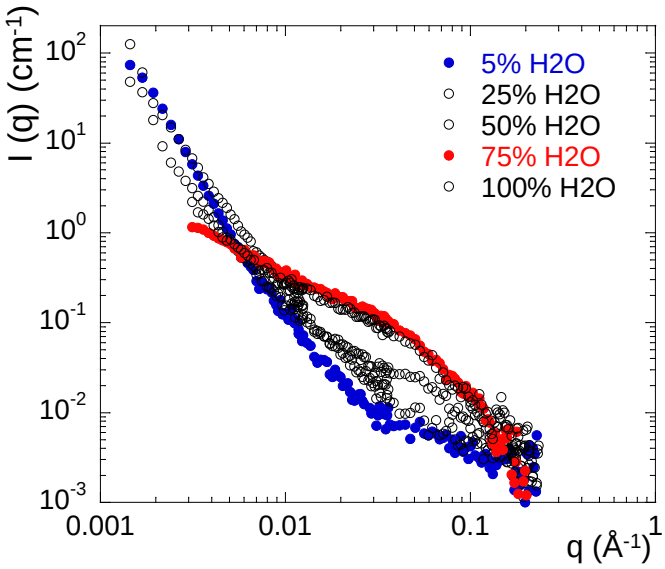

Figure IV. 4 Variation of the SANS intensity as a function of the H_2O/D_2O ratio, from 5 to 100 vol. %, for a Fe-OM aggregate at Fe/OC ratio of 0.3. The blue curve is the contrast matched condition of the Fe part (H_2O/D_2O = 5 vol. %) and the red curve is the contrast matched condition of the HA part (H_2O/D_2O = 75 vol. %).-

From a qualitative point of view, the blue and red curves presented two different shapes indicating that the morphologies of the two parts of the Fe-OM aggregates were different when they were associated in the complex. This was especially true for the Fe part showing a different shape of the scattering intensity compared to the pure HFO (Figure IV. 3). Let's now quantify these morphology variations as a function of the Fe/OC ratio. The Fe-OM aggregates was firstly analyzed in the HFO contrast matched conditions (H_2O/D_2O=5 % vol.) to highlight the HA morphology inside the colloid. The SANS curves were presented in Figure IV. 5 for 3 Fe/OC ratios R=0.05, R=0.16 and R=0.3.

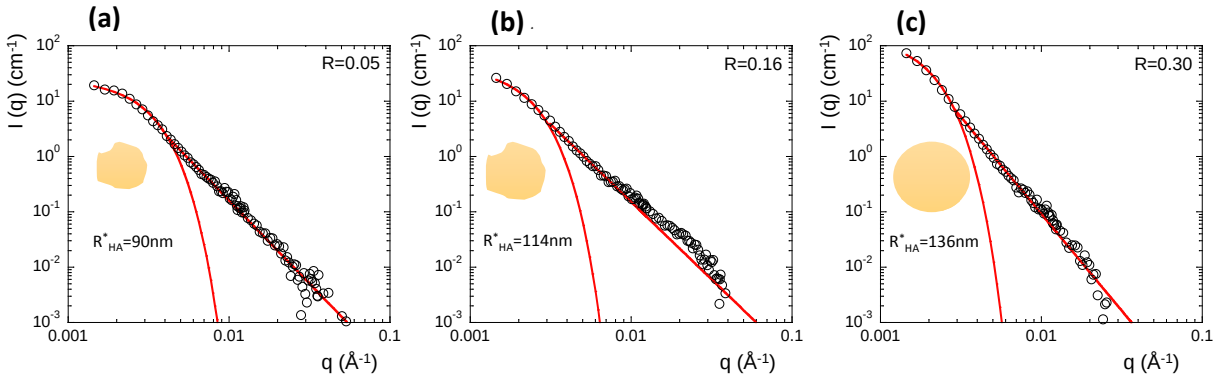

Figure IV. 5 SANS curves of the Fe-OM aggregates at the contrast matched conditions of the Fe part (H_2O/D_2O = 5% vol.) at Fe/OC ratios R=0.05 (a), R=0.16 (b) and R=0.30 (c). The red lines are the Guinier calculations (Eq. 3) and the straight lines indicate the slopes of the power law (Eq. 4).

The same analysis than for the pure HA was applied. The curves were fitted using the Eq.3 and 4 to extract the radius of gyration, the corresponding geometrical radius and the fractal dimension of the HA part in the Fe-OM aggregates. The values were reported in the Table IV. 2. The geometrical radius of the HA part was noted R^*_{HA}.

Table IV. 2 Fitting parameters deduced from the analysis of the SANS curves at the Fe contrast match conditions to illustrate the HA part morphology in the Fe-OM aggregates. The error on the parameters was 15%.

Sample	R=0.05	R=0.16	R=0.30
I_0 (cm^{-1})	28	42	140
R^*_{HA} (nm)	90	114	136
D_f	3.0	2.8	3.5

The morphology of the HA part within the aggregates was close to the pure HA. The size of the HA part was rather smaller in the Fe-OM colloids than in the pure HA component and increased with increasing the Fe content. Similarly, the fractal dimension also increased traducing a raise of the compactness of the HA component.

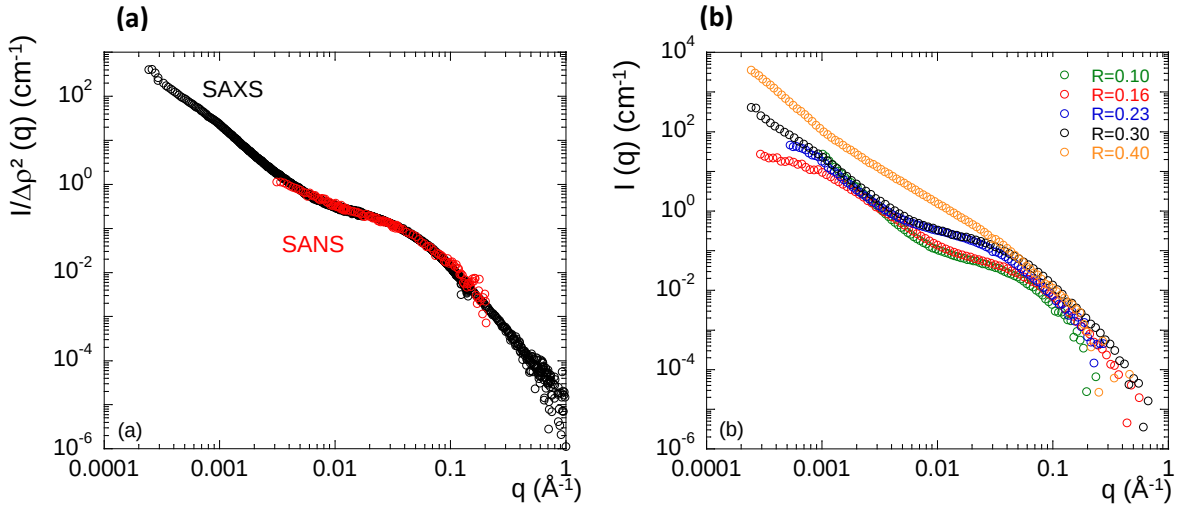

Figure IV. 6 (a) Comparison between SAXS (black curve) and SANS (red curve) at the OM contrast matched ratio for the Fe-OM aggregate at R=0.3 (b) Variation of the SAXS curves on the Fe-OM aggregates as a function of the Fe/OC ratio R=0.1 (green), R=0.16 (red), R=0.23 (blue), R=0.30 (black) and R=0.40 (orange).

We focus now on the characterization of the Fe part of the aggregates. Records of SANS at the HA contrast matched conditions (H_2O/D_2O = 75/25% vol.) was used and completed by SAXS where the contrast was dominated by the Fe part. An example was given in Figure IV. 6a for a Fe/OC ratio R=0.30 for the same sample. After normalization of the scattering curves by the contrast equal to $\Delta\rho^2$=2.37 10^{21} cm^{-4}, both SAXS (black) and SANS (red) curves superimposed perfectly. For this given neutron contrast, both SANS and SAXS probed the same morphology of aggregates. However, SAXS offered a larger q range with an excellent resolution. For this reason, we used SAXS to characterize the evolution of the Fe part morphology in the Fe-OM aggregates as a function of the Fe/OC ratio by combining measurements on ID2 and MOMAC to extend the q range (Figure IV. 6b). As expected, the scattering intensity scaled the Fe content. As for pure HFO, the scattering curves showed two shoulders corresponding to different characteristic sizes - a local small one and a large scale one – and followed a power law behavior illustrating the compactness of the object. The shifting of the high q shoulder to the low q values when increasing the Fe/OC ratio indicated that the small size increased with the ratio as a result of a new aggregation level. We used the same previous model of fractal aggregates to describe the scattering curves. First, we modeled the high q shoulder with the idea that the primary beads formed intermediate aggregates (different from the primary aggregates seen in the pure HFO). An example of such modeling was given in Figure IV. 7a for the Fe/OC ratio R=0.16. The results of the modeling for the different Fe/OC ratios were reported in Table IV. 3.

Table IV. 3 Fitting parameters for the intermediate aggregates form factor deduced from the analysis of the SAXS curves. Fixed parameters are the primary bead radius R_0=0.8, the log normal distribution σ=0.3 and the contrast $\Delta\rho^2$=2.37 10^{21} cm^{-4}. The errors on the parameters were 15%.

Sample	R=0.1	R=0.16	R=0.23	R=0.30	R=0.40
φ_0	9.74 10^{-5}	2.58 10^{-4}	2.36 10^{-4}	5.20 10^{-4}	4.35 10^{-4}
N_{IA}	30	11	32	25	110
R_{IA} (nm)	3.3	2.7	4.2	3.6	5.7
$D_{f\,IA}$	2.40	2.00	2.40	2.15	2.40

Following the determination of the intermediate aggregate form factor, we could, according to Eq. 1, divide the total scattering intensity by this form factor to extract an apparent structure factor S_T (q).

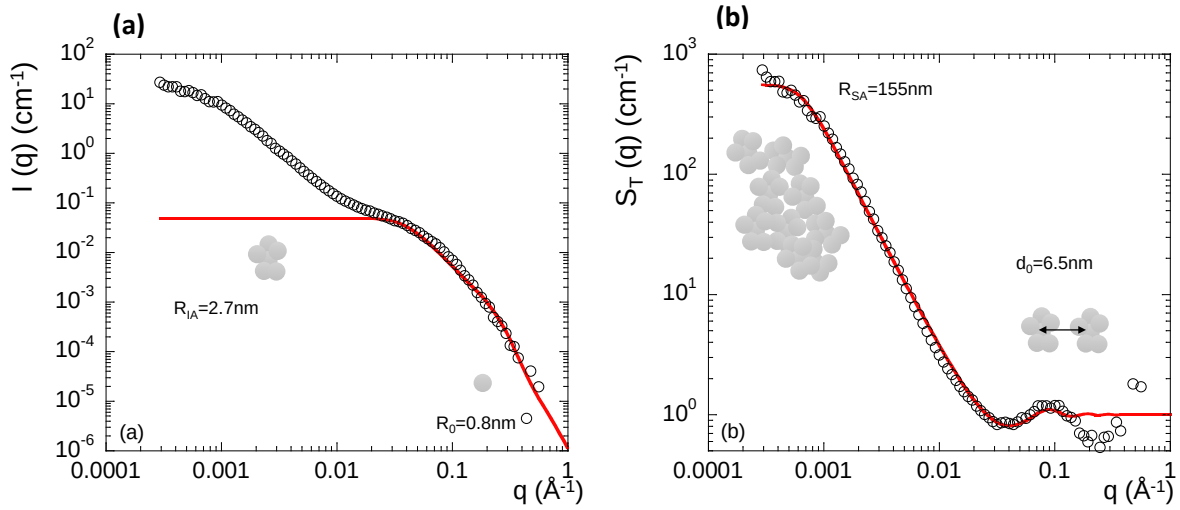

Figure IV. 7 (a) SAXS curve obtained on the Fe-OM colloids at a Fe/OC ratio R=0.16 and the modeling of form factor of the intermediate aggregate (red line) from the spherical form factor of the primary beads. (b) Apparent structure factor ST (q) deduced from the division of the total intensity I (q) by the calculated form factor of the intermediate aggregate. The sketches represent from the left to the right the primary beads, the intermediate and the secondary aggregates.

This apparent structure factor, reported in Figure IV. 7b, exhibited a peak at high q representing the interactions between the intermediate aggregates. This suggested that the low q increase of the scattering intensity came from the formation of secondary aggregates made from the assembly of a finite number of intermediate aggregates. We were able to model the apparent structure factor as the sum of the interacting Percus-Yevick function. The form factor of the secondary aggregates was calculated using the same previous fractal model by fixing the size of the primary beads (R_0) to the one of the intermediate aggregates (R_{IA}). An example of such modelling was given in Figure IV. 7b (red line) and the parameters deduced from the fit for the different Fe/OC ratios were reported in Table IV. 4.

Table IV. 4 Fitting parameters for the apparent structure factor ST deduced from the analysis of the SAXS curves. Fixed parameters are the primary bead radius $R_0=R_{IA}$, the log normal distribution $\sigma=0.3$ and the contrast $\Delta\rho^2=2.37$ 1021 cm-4. The errors on the parameters were 15%.

Sample	R=0.1	R=0.16	R=0.23	R=0.30	R=0.40
$D_{f\,IA}$	2.40	2.00	2.40	2.15	2.40
R_{SA} (nm)	131	155	187	400	689
$D_{f\,SA}$	2.50	1.85	1.85	2.25	2.15
d_0 (nm)	7.5	6.5	7.0	8.0	15.0

We then analyzed the variations of the different parameters of the Fe component in the Fe-OM aggregates relative to the Fe/OC ratios. In the Figure IV. 8a and 8b, we can see that both the radius of the intermediate and of the secondary aggregates increased with the Fe/OC ratio as a result of the aggregation process. Both the number of primary beads per intermediate aggregates and the number of intermediate aggregates per secondary aggregates increased. The morphologies of the different objects varied also with the Fe/OC ratios, as highlighted by the fractal dimensions evolution in Figure IV. 8c and 8d. The fractal dimension of the intermediate aggregates slightly increased, illustrating a compaction of the objects. By contrast, the fractal dimension of the secondary aggregates slightly decreased with the Fe/OC ratio revealing a light opening of the aggregates structure.

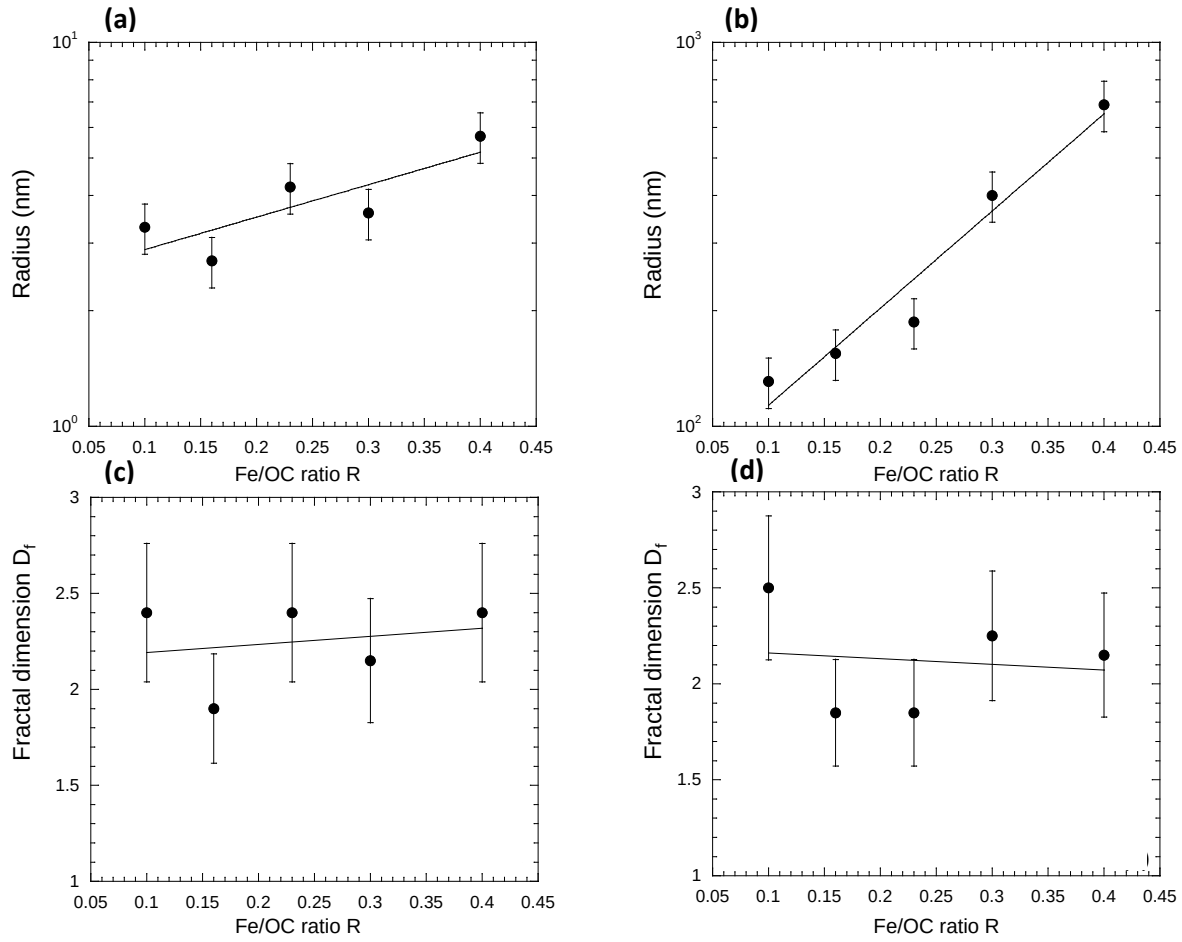

Figure IV. 8 Variations of the radius as a function of the Fe/OC ratios for (a) the intermediate aggregates, (b) the secondary aggregates. Variation of the fractal dimension as a function of the Fe/OC ratios for (c) the intermediates aggregates, (d) the secondary aggregates.

IV.3.1.2 Dynamic light scattering results

In complement to the previous determination, dynamic light scattering (DLS) was used to characterize the aggregates in solution for a Fe/OC ratio of 0.4. One advantage of the DLS is to extend the domain of observation toward the larger sizes to see whether additional larger scale structures are present in the system. The Figure IV. 9 presents the size distribution obtained with DLS for various decreasing filtration cut off, namely the bulk (red double dot line), and the same suspension filtered at 0.2 µm (blue double dot line) and below 1000 kDa (orange double full line). The size distribution was determined from six measurements to obtain a representative statistical size distribution. For the bulk, two broad populations appeared. A first one between 4 and 70 nm, centered around 30nm, and a second between 100 and 1000 nm, centered around 300 nm. The large

scale population is dominant in numbers compared to the small scale population. Following the first filtration (below 0.2 µm), both characteristic sizes decreased: the large scale population moved toward a centered value around 150nm while the small scale population moved toward a centered value equal to 15nm. The respective intensities also decreased indicating that the number of large objects decreased relative to the number of small objects. After the second filtration stage (below1000 kDa), the large population was still present but reduced to a very small fraction. Almost all the intensity was focused on the small scale population centered around 15 nm.

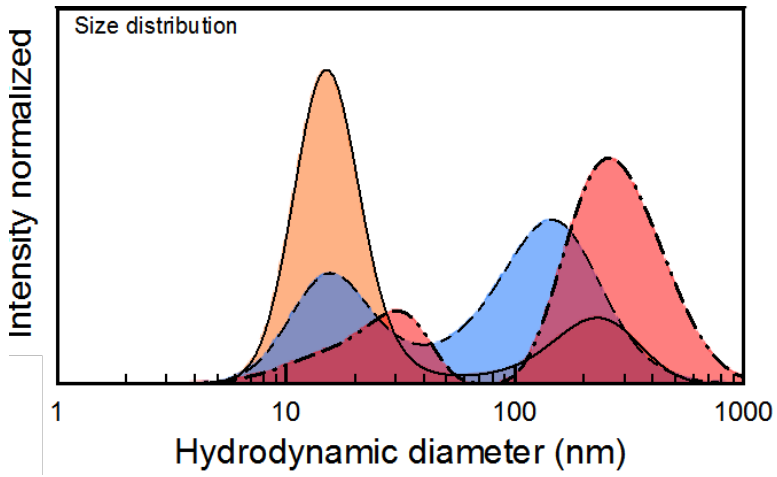

Figure IV. 9 Size distribution and Padé-Laplace mean size determination obtained by DLS for the bulk sample (red trace and double dotted line), the solution filtered below 0.2 µm (blue trace with dot-line) and the solution filtered below 1000 kDa (orange trace with full line). All the results represented the statistical size distribution on six replicates. The uncertainties on the size determination were not represented due to the convenient accuracy of the determination (less than 0.2% of error).

Although compare scattering and DLS is difficult, the large scale population ranging from 100 and 1000 nm diameter seem to be consistent with the secondary aggregates (average diameter 1400nm) highlighted by the SANS/SAXS analysis (Table IV. 4) for the Fe/OC ratio R=0.4. The difference obtained with both techniques can be attributed to a combination of several factors such as the sizes extraction methods (weighting on the numbers of scatters for DLS and on the mass of the scatters for the SAS) and the polydispersity effects. In addition, when considering fractal modelling instead of a simple spherical geometry, larger discrepancy is commonly observed between the corresponding geometrical fractal calculation and the hydrodynamic values. The new insight here is

the presence of the small scale population whose typical size is close to that of intermediate aggregates (average diameter 12nm). This result suggests that a fraction of the Fe beads forms intermediate aggregates which are stabilized in solution in the sample while another part is aggregated to form larger secondary aggregates

IV.3.1.3 Iron X-ray absorption spectroscopy

Iron K-edge XANES analyses were performed on the 3 Fe-OM aggregates (i.e. R=0.3, R=0.23 and R=0.1). The EXAFS spectra and the corresponding Fourier transforms (FT) (magnitude and imaginary part) of the aggregates were reported in Figure IV. 10a). The EXAFS spectra of R=0.23 and R=0.3 were similar with a small oscillation at around 7.5 $Å^{-1}$ whose intensity was higher for R=0.3. Both spectra exhibited a shoulder in the oscillation at 9.8 $Å^{-1}$ which was more pronounced for R=0.3. The R=0.1 EXAFS spectra presented no oscillation at 7.5 $Å^{-1}$ or shoulder at 9.8 $Å^{-1}$. Three peaks dominated the FT of the aggregates. The first peak, located at approximately 1.5 Å (R+ΔR), corresponded to the first shell of the neighboring atoms within the FeO_6 octahedra. The second and third peaks at approximatively 2.6 Å (R+ΔR) and 3.2 Å (R+ΔR) arose from the scattering of the Fe neighbors from the second and third coordination shells.

The shell fits were performed on the 1-3.5 Å range of the Fourier transformed k3-weighted spectra over a k-range 2-11 Å (Figure IV. 10 b). The resulting EXAFS parameters of the fits were reported in Table IV. 5. For the 3 aggregates, the first O shell was accurately modelled with one Fe-O path at an average distance of 1.98 ± 0.01 Å with a Debye-Waller of 0.009 ± 0.001. This distance corresponded to the Fe-O distances for the octahedra in the Fe(III)-oxyhydroxides (Waychunas et al., 1993). The fitted model contained two additional Fe-Fe paths. The first Fe-Fe1 distance was reported at 3.00-3.02 Å with a Debye-Waller at 0.007, 0.011 and 0.010 for R=0.1, R=0.23 and R=0.3 respectively. This distance was characteristic of edge-sharing FeO6 octahedra (Manceau and Combes, 1988; Manceau and Drits, 1993). The second Fe-Fe2 distance was specific to double corner-sharing as previously reported (Manceau and Combes, 1988; Waychunas et al., 1993; Bottero et al., 1994) at

3.50 ± 0.02 Å for R=0.1, 3.47 ± 0.02 Å for R=0.23 and 3.46 ± 0.03 Å for R=0.3. With the increasing Fe concentration, the number of corner sharing increased.

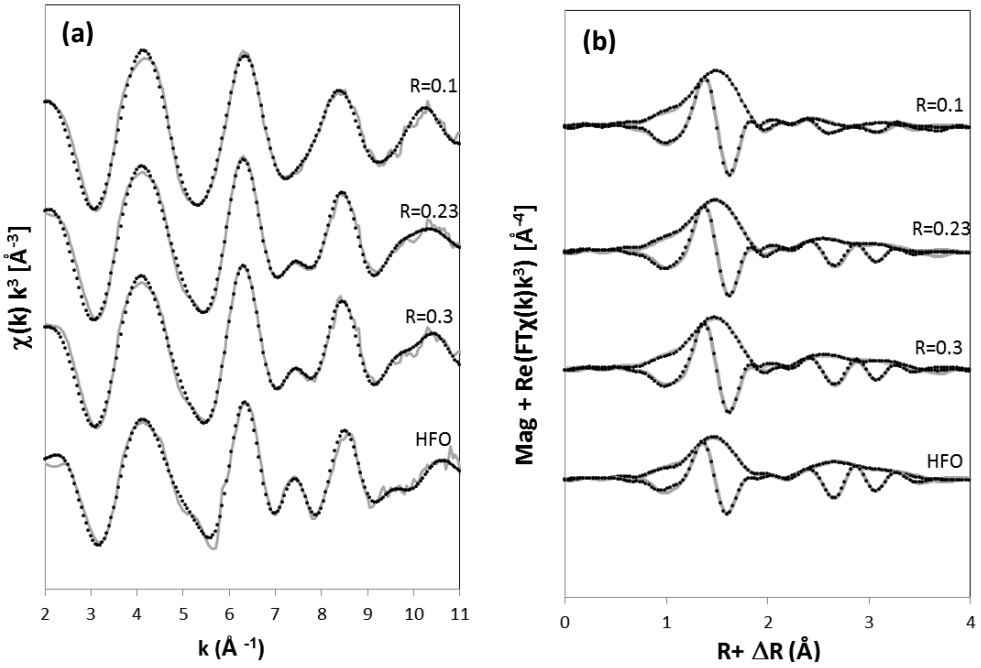

Figure IV. 10 (a) Iron K-edge EXAFS spectra of the three different ratios aggregates and HFO and (b) magnitude and imaginary part of the associated Fourier transform (uncorrected from phase shift). Solid lines are experimental data and dotted lines are the fit results.

A Fe-C path at 2.84 Å was necessary to accurately fit the R=0.1 EXAFS spectrum. This was supported by the low coordination number of 0.6 ± 0.4 Å obtained for corner-sharing distance Fe-Fe_1. At this distance, the number of Fe for R=0.23 and R=0.3 was consistent to three octahedra bound to the edge. These results revealed that two Fe phases coexisted for low Fe/OC ratio, small Fe(III)-OM complexes and nanometric Fe(III)-oxides whose distances at around 3.06 and 3.46 Å were specific to ferrihydrite (Manceau and Combes, 1988; Mikutta, 2011). For higher Fe/OC ratio (i.e. for R=0.23 and R=0.3), no Fe-C distance was detectable suggesting that only nanometric Fe(III)-oxides were present. Similar results were obtained by (Karlsson and Persson, 2012) at a Fe/OC ratio of 0.11. They observed a Fe-C distance at 2.89 Å which they interpreted as mononuclear Fe(III)-NOM complexes. In previous studies on fresh-water Fe-NOM samples, (Rose et al., 1998)and (Vilgé-Ritter et al., 1999) reported a Fe-C distance in the range of 2.76-3.0 Å and demonstrated that Fe was complexed with OM and poorly crystallized.

Table IV. 5 [a]N, path degeneracy (coordination number); [b]R(Å), interatomic distance [c]σ²(Å), Debye-Waller factor; [d]Energy-shift parameter; [e]R-factor =Σi(data$_i$-fit$_i$)²/Σ$_i$data. * Coordination number of O distal was covaried as follows: N$_O$dist = 2xNFe1 + (NFe2-NFe1). The amplitude reduction factor, S0², was set to 0.75. Parameter uncertainties are presented for the last significant figure and determined by the fitting

	Fe-O			Fe-C			Fe-Fe1			Fe-Fe2			Fe-O$_{dist}$				
Sample	**N**[a]	**R**[b] (Å)	**σ**^{2} [c]	**N**	**R (**Å)	**σ**^{2}	**N**	**R (**Å)	**σ**^{2}	**N**	**R (**Å)	**σ**^{2}	**N**	**R (**Å)	**σ**^{2}	**ΔE**$_0$ [d]	**R factor** [e]
HFO	2.8 (1)	1.93 (1)	0.003				1.2 (2)	3.03 (2)	0.010	2.6 (3)	3.49 (2)	0.01	4.1 (4)	3.60 (4)	0.010	0.9	0.0040
	1.6 (2)	2.09 (1)	0.003														
R=0.1	6.1 (3)	1.98 (1)	0.009	0.9 (9)	2.84 (5)	0.007	0.6 (4)	3.00 (2)	0.007	0.4 (4)	3.50 (2)	0.005	1.0 *	3.72 (3)	0.007	-2.76	0.0062
R=0.23	6.2 (4)	1.98 (1)	0.010				1.6 (3)	3.02 (1)	0.011	1.4 (2)	3.47 (2)	0.007	3.3*	3.64 (6)	0.011	-2.38	0.0053
R=0.3	5.9 (5)	1.97 (1)	0.009				1.3 (4)	3.01 (1)	0.010	2.6 (5)	3.46 (3)	0.009	4.0*	3.62 (6)	0.007	-2.09	0.0065

IV.3.1.4 High TEM resolution observation of the aggregates conformation

The representative Transmission Electron Micrographs (TEM) of the Fe-OM aggregates at a ratio R=0.4 were displayed in Figure IV. 11. The Figure IV. 11a displayed the intermediate resolution picture. Two populations can be observed: a large object that seemed to be the results of the assembly of a large number of small dark spherical entities, and several non-associated entities that surrounded the central aggregate. This central aggregate was fully consistent with both the secondary aggregates highlighted with SAXS/SANS and the large scale population obtained by DLS. The Figure IV. 11b showed a high resolution TEM picture of the out off part of the aggregate. The sample was composed of a clear matrix with diffusely distributed darker particles whose crystal lattices were visible. The EDS composition as well as their higher electron density indicated that these particles were composed of Fe. Their nanometric sizes (around 5 nm diameter) were consistent with the intermediate aggregates deduced from the previous scattering analysis (Table IV. 3). The existence of non-associated, isolated intermediates aggregates was also consistent with the small scale population showed with DLS. The Figure IV. 11c showed the high resolution TEM picture of the inside part of the central aggregate. According to the SAXS results, one can clearly see that the secondary aggregates were composed of the association of sphere-like objects whose size (5nm diameter) was consistent with the intermediate aggregates. In addition and also according to the SAXS results, one can see that the intermediate aggregates were not in close contact inside the secondary aggregate. If considering two intermediates aggregates (the two sphere-like beads pointed with a red arrow that presenting a similar grey level which are probably in the same horizontal plan), we can approximatively evaluate the center to center inter-intermediate aggregate distance to be around 25nm. This distance was consistent with the d_0 distance deduced from the SAXS analysis equal to 15nm for the Fe/OC ratio R=0.4 (Table IV. 4).

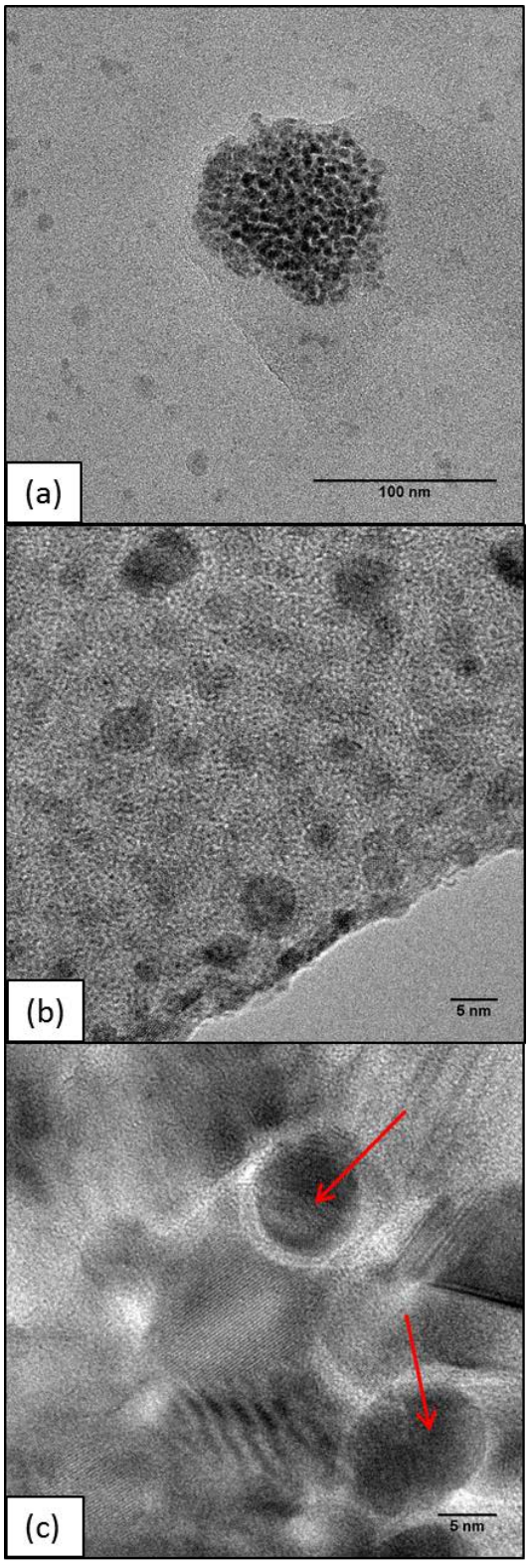

Figure IV. 11 Transmission Electron Microscopy micrographs of the R=0.4 Fe-OM aggregates suspension showing (a) a secondary aggregate surrounded by free intermediate aggregates (b) a close-up on the free intermediate aggregates and (c) a close-up on the secondary aggregate. The grey part in the right bottom corner of (b) corresponds to the edge of the grid. The red arrows corresponds to the considered agregates

IV.3.2 As adsorption on Fe/OM aggregate

Arsenic adsorption experiment results were displayed in Figure IV. 12 for two As/Fe ratios, $R_{As/Fe}$ =0.18 and 0.005. For a same As/Fe ratios, the concentration of adsorbed As increased with the increasing Fe/OC ratio. For the As/Fe ratio $R_{As/Fe}$ =0.18, the proportion of adsorbed As was 36.0%, 48.5% and 53.7% at R = 0.1, R = 0.23 and R = 0.30 Fe/OC ratio respectively. For the $R_{As/Fe}$ =0.005, the proportions of adsorbed As was 67%, 82% and 96.3 % at R = 0.1, R = 0.23 and R = 0.30 Fe/OC ratio, respectively.

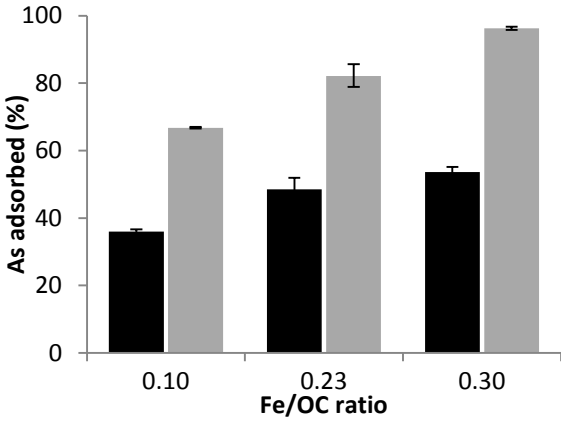

Figure IV. 12 Percentage of adsorbed As for the three Fe/OC aggregates ratios. Black bars correspond to the As/Fe ratio, RAs/Fe = 0.18 and the grey bars to the As/Fe ratio RAs/Fe = 0.005.

Arsenic adsorption, according to the fractionation size, was reported in Table IV. 6 along with the concentrations in Fe and OC the As/Fe ratio and Fe/OC ratio. For both large fractions, OC, As and Fe concentrations were quite similar (i.e. Bulk-1000 kDa and 1000-100 kDa). Moreover, they exhibited the same As/Fe ratio which was equal to the initial As/Fe ratios, $R_{As/Fe}$ =0.005. Almost all Fe and As were present in those both largest fractions. By contrast, in the < 100 kDa fraction, only 2 % of Fe and 7 % of As against 15 % of OC were determined.

Table IV. 6 Concentration of Fe, OC and As in the different fractions in the sample at an initial Fe/OC ratio of 0.4. The repartition (%) of OC, As and Fe were indicated for each fraction.

Fractions	OC mg L^{-1}	OC %	As mg L^{-1}	As %	Fe mg L^{-1}	Fe %
Bulk-1000 kDa	162.4	42	0.41	45	84.2	47
1000-100 kDa	165.9	43	0.44	48	91.9	51
< 100 kDa	59.8	15	0.06	7	3.3	2

IV.4 Discussion

IV.4.1 Evolution of Fe-OM aggregates structure: influence on As adsorption

The analysis of the synthetic HFO using SANS and SAXS showed that two sizes coexisted according to a fractal assembly (D_f=2.5): a large unit of R=73 nm (primary aggregates) composed of small spherical units of R_0=0.8 nm (primary beads). The pure HA analysis was composed of a single size (R=110nm) and compact entity (D_f=2.8). Jarvie and King (2007) showed in river sediment that OM promoted the formation of 3D "network"-like structure, as small ramified OM between aggregates. This difference with our model of a one compact organic size could be explained by the difference in OM origin between both studies. Jarvie and King (2007) studied naturel river fulvic OM although here wetland soil humic acid was used. When HA was mixed to Fe, Fe and HA combined together to form a binary Fe-OM aggregate whose different part could be analysed separately: SANS enabled to see only the HA part of the aggregate while SAXS enabled to see only the Fe part. The HA part of the Fe-OM aggregate showed a structure very close to the pure HA entity whose size and compactness slightly increased when the increasing Fe/OC ratio. Conversely, the Fe part presented a structure different from the pure HFO. The primary beads (Figure IV. 13, 1) formed intermediate aggregates (Figure IV. 13, 2) which organized themselves to form secondary aggregates (Figure IV. 13, 3). Within the uncertainties range, the intermediate aggregates presented a repulsive interaction when composing the secondary structure. Both sizes and multi-scale assemblies were nicely confirmed by TEM and DLS. In addition, both DLS and TEM showed the presence of additional isolated intermediate aggregates which seemed to be stabilized in the sample and to be independent from the secondary aggregates (Figure IV. 13, 4). The Fe part structure of the secondary aggregate

became slightly more ramified (decreasing of the Fe fractal dimension (Df) (Figure IV. 8d)) as the hydrolysis increased. With the increasing Fe/OC ratio, the Fe K-edge EXAFS demonstrated that the Fe neighbors in edge and corner sharing increased reflecting a higher polymerisation of intermediate aggregates. The EXAFS results were thus coherent with both SANS/SAXS measurements and TEM observations. Several authors demonstrated that for high OM amount, Fe hydrolysis was impaired and crystals growth limited (Cornell and Schwertmann, 2003; Pédrot et al., 2011b), which was coherent with the presence and the size of intermediate aggregates (i.e. nano-oxides). They are stabilized in the suspension probably regards to their complexation with non-aggregated organic molecules (figures V. 13, 4). For similar Fe-OM aggregates synthesis, Pédrot et al., (2011) showed that a small fraction of Fe did not precipitate but instead was adsorbed on HA. In our experiment, for Fe/OC ratio R=0.1, adding a Fe-C distance at 2.84 Å improved the fit of the EXAFS spectra. This distance could be attributed to the presence of small Fe(III) clusters or Fe(III) monomers bound to OM (Figure IV. 13, 5) (Guénet et al., 2016; Karlsson and Persson, 2012; Sjöstedt et al., 2013). These small clusters might correspond to the primary beads of R_0=0.8 nm (Figure IV. 13, 6). The Fe-C distance was not detected for the R=0.23 and R=0.3 Fe/OC ratios since the number of heavy Fe neighbors increased and thus masked the Fe-C contribution. However, at high Fe/OC ratio, R=0.4, filtration analysis demonstrated that about 2 % of Fe was present the <100 kDa fraction, namely in fraction without secondary or intermediate aggregates, as displayed in Table IV. 6. Therefore, even at high Fe/OC ratio, small amount of Fe remained as small entities that could be considered as Fe individual primary beads. Their stabilization was explained by their binding to organic molecules as confirmed by the Fe-C distance fitted in the EXAFS spectra and TEM observations., Organic matter is a complex polydisperse mixture of various organic molecules (e.g., Piccolo et al., 1996; Wershaw, 1999). Regards to their hydrophobicity, molecular weights, steric arrangement and OH sites density, organic molecules can be fractionated by adsorption with Fe oxides (Gu et al., 1995). In the present work, some organic molecules were not bound to Fe (figure V.13, 7) while others were complexed with Fe controlling its hydrolysis and crystals growth (figure V.13, 4,5,6). SANS provided evidence

that a second part of OM formed dense aggregated structures within the secondary aggregates (Figure IV. 13.8). Such dense aggregates were probably bound to secondary Fe aggregates since their sizes increased with the increasing Fe/OC ratio and the secondary Fe aggregates ramification. Baigorri et al., (2007) studied molecular aggregation of humic substances (HS) and suggested that HS could be composed of stable molecular aggregates and supra molecular associations in which low and high molecular weight molecules coexist. In such supra molecular assemblies, molecules are stabilized together by dispersive weak forces. Therefore, to summary, OM was present as organic molecules organized as non-aggregated molecular network showed by the high OC concentration measured in the <100KDa fraction (i.e. 59.8 mg L^{-1} of OC) while no aggregates were detected by DLS. They were bound, or not, to Fe clusters, isolated Fe beads and intermediate aggregates. Organic matter was also present as nanometric dense aggregates associated with the Fe secondary aggregates.

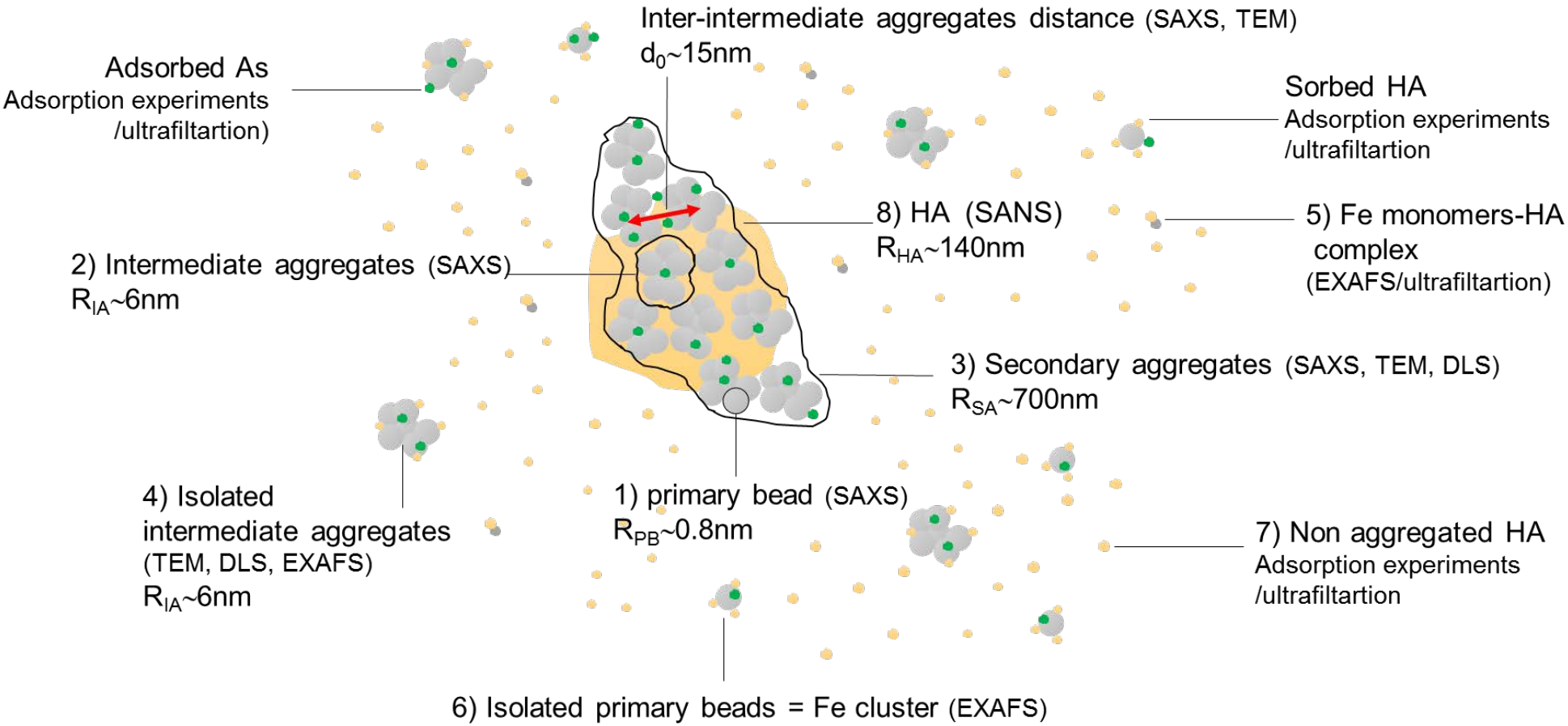

Figure IV. 13 Schematic representation of the different Fe-OM aggregates and associated methods used for their identification. The color grey was attributed to Fe, orange to OM and green to As.

At constant As/Fe ratio, As adsorption increased with the Fe/OC ratio. The enhancement of the adsorption was commonly attributed to the decreasing particle size which induced an increase of the surface area (Yean et al., 2005; Wang and Shadman, 2013). However, the present study demonstrated that the As adsorption was promoted by the increase of the particles size at high Fe/OC ratios suggesting the occurrence of another mechanism. The variation of the specific surface was therefore investigated. Knowing the volume fraction of primary beads φ_0 from the data fitting, the high q domain of the scattering curves, the so-called Porod region which is proportional to the specific surface of the system, can be investigated according to Eq. 6:

$$\text{Lim } I.q4 = 2\pi\varphi_0\Delta\rho^2 S/V \qquad \text{(Eq. 6)}$$

Assuming a mean density for the Fe aggregates equal to 3.96 g/cm^3 (Hofmann et al., 2004), the specific surface S/V variations was calculated relative to Fe/OC ratio (Figure IV. 14a). Despite that the aggregation process was supposed to reduce the specific surface, the specific surface remained on average constant around 900 m² g^{-1} with the increasing ratio, even for the largest aggregates. A tentative explanation of this effect, was to consider the distribution of intermediary aggregate inside the secondary structure and the organization variation with the Fe/OC ratio. In Figure IV.14b were reported the variations of the d_0 between intermediate aggregates within secondary aggregates and the corresponding sizes of the intermediate aggregates equal to twice the radius (Table IV. 3). Whatever the Fe/OC ratio, the distance between the aggregates was larger than the aggregate dimension (in comparison with the linear full line correlation) indicating that the repulsions between the aggregates inside the secondary structure were always effectives. In other words, the intermediate aggregates were never in close contact with a neighboring structure. In addition, for the larger ratio R=0.4, the deviation with the full line became larger suggesting that the repulsive interactions specifically increased for this ratio. Beyond to be visible for only a single dot, this trend was confirmed with the TEM (Figure IV. 11c) that showed a distance between the aggregates (25nm) significantly larger than the aggregates size. This is also in line with the aggregate morphology variation which showed a slight decrease of the fractal dimension of the secondary structures (Figure

IV. 8d). This fractal dimension decrease suggested an opening of the structure as a result of the internal repulsions raise. Such increase of the internal repulsions can induce an increase of the number and/or the density of the binding sites for the As adsorption despite of the aggregation process.

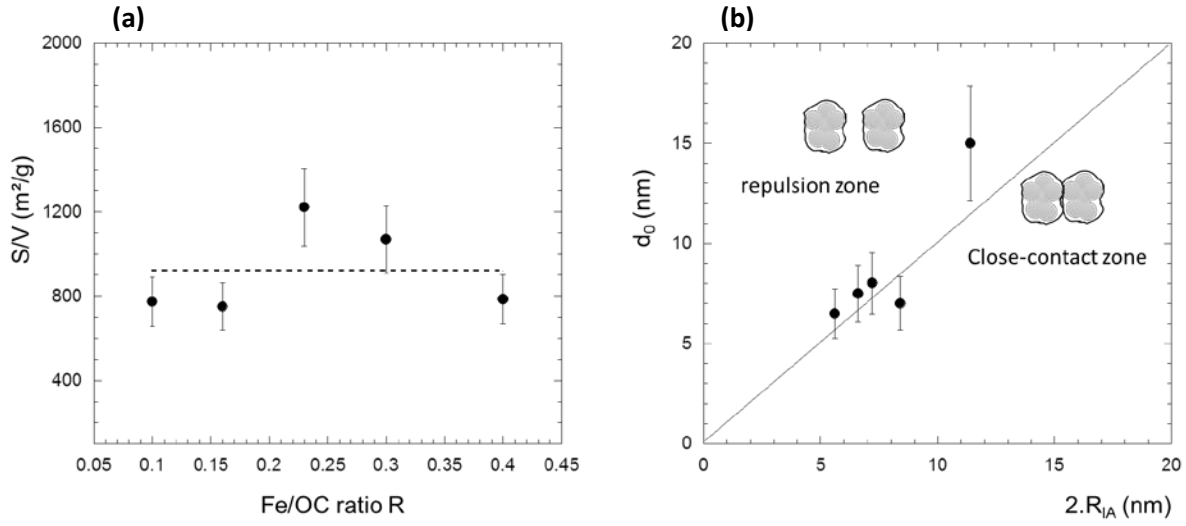

Figure IV. 14 (a) Specific surface S/V determination from the Porod law analysis (Eq. 6) relative to the Fe/OC ratios, the dot line is the average value. (b) Variation of the interacting distance d0 with the diameter of the intermediate aggregates RIA, the full line corresponds to d0=2*RIA

A second explanation could be a coating rate decrease in the secondary aggregate with the Fe/OC ratio inducing a increase of the As binding site availability. With the increasing Fe/OC ratio, the size and the Df of the Fe part increased more strongly than the size of the OM part of the secondary aggregates, 131 to 400 nm against 70 to 105 nm, respectively. The Fe part grew strongly than OM part and more As binding were available.

IV.4.2 Environmental implications

The present results provided evidence that Fe(III)-oxyhydroxides specific surface area was not the only controlling parameter of the binding capacity of large Fe-OM aggregates. The importance of these results was highlighted by considering the possible variations of the Fe/OC ratio under various environmental conditions. For example, in wetland soil solution, Dia et al. (2000)

measured Fe/OC ratios varying around 0.20 (wt.wt); in boreal rivers, Pokrovsky et al. (2011) displayed Fe/OC ratio around 0.06; while Neubauer et al. (2013) calculated Fe/OC ratios for stream aggregates during storm event varying from 0.01 to 0.05 relative to the primary stream water concentrations. The range of Fe/OC ratio extended throughout the range from Fe monomers bound to OM to nano-Fe(III)oxyhydroxides associated to spheroid compacted OM. The result was contrasted metal or metalloid sorption mechanisms. Such new results could explain the discrepancy observed between modelling calculations and field/experimental sorption datasets when OM-rich aggregates prevailed. Several studies observed a decrease in As(V) adsorption on crystalline Fe(III)-oxyhydroxides in the presence of OM (Bowell, 1994; Grafe et al., 2001). Such decrease was often explained as a competition between As and OM, regard here as competitive anionic species for the Fe(III)-oxyhydroxides adsorption sites. However, in natural organic-rich environment, prevailing Fe(III)-oxyhydroxides are not well crystallized particles but rather nanometric Fe(III)-oxyhydroxides embedded in an organic matrix. In such context, the present results shed a new light on the As sorption decrease in presence of OM suggesting that the adsorption decrease occurred through the Fe species distribution (dispersed small cluster or nano-Fe(III)-oxyhydroxides) and their degree of coating by the organic molecules.

It is important to note that the secondary aggregates, despite representing less than 10 % of the number of particles, adsorbed high As amount (Table IV. 6). However, as the largest aggregates, they are suspected to be more easily settled in the soil porosity limiting thereby the expected As mobility in the environment (Kocar et al., 2008; Polizzotto et al., 2008; Fendorf, 2010).

IV.5 Conclusion

In this study, we successfully combined neutron and X-ray scattering with EXAFS and imaging technique (TEM) to investigate Fe-OM aggregates structure. Small angle neutrons scattering allowed probing OM and Fe phases separately. A fractal model was adapted to the Fe part and three distinct sizes were observed: i) primary beads of 0.8 nm which were distributed as individual beads bound to

organic molecules or which composed ii) intermediate nanometric aggregates, which were distributed as isolated aggregated bound to organic molecule or as iii) secondary Fe-aggregates associated with dense OM structure (Figure IV. 13). Before reaching Fe(III)-oxyhydroxides solubility limit, Fe(III) was complexed to OM as monomers or small clusters, the latter can be considered as primary beads. When the solubility limit was locally reached, Fe(III) precipitated as nano-oxides at various scale embedded in OM, namely bound to organic molecules. With the continuous increase of Fe content, the intermediate aggregate aggregated until forming a secondary aggregate in which OM formed a spherical dense structure. With the increasing Fe/OC ratio, the size of such large secondary aggregates increased and their Fe part was more and more ramified. Within secondary aggregates, repulsive forces increased between intermediate aggregates which was traduced by an increase of the distance between intermediate aggregates. A direct impact of this distance increase was a enhance of the As binding sites availability. A second hypothesis concerned the coating rate between the Fe and the OM part of the secondary aggregate. When Fe/OC increased, the Fe part grew more strongly and was more and more ramified as compared to the OM part. The coating therefore decreased and the availability of binding site increased.

Chapitre V. Conclusions et perspectives

V.1 Conclusions

Dans le contexte de la contamination des eaux par l'As, l'objectif de ce travail de thèse a été d'étudier les produits de réoxydation du sol d'une zone humide riparienne et la spéciation de l'As associé afin de mieux appréhender la dynamique et le devenir de l'As dans l'environnement.

A travers trois études connexes ce travail a permis de :

- déterminer le rôle de la matière organique dans l'oxydation de l'As lors de la réoxydation de la zone humide et également son influence sur la nature des phases porteuses de l'As.
- mettre en évidence la grande variabilité de spéciation de l'As (organique et inorganique) produit lors de la réoxydation de la zone humide
- déterminer l'influence de la structure des agrégats Fe-MO sur leur capacité d'adsorption de l'As

V.1.1 Rôle de la matière organique sur l'état d'oxydation de l'As et sur la nature des phases porteuses.

Dans cette première partie, j'ai analysé des échantillons solides produits par réoxydation d'un sol de zone humide riparienne (Naizin, ORE Agrys, France). Ces échantillons ont été prélevés directement sur le terrain à l'aide d'un système de pièges téflon (Al-Sid-Cheikh et al., 2015). La caractérisation chimique des solides a montré un enrichissement en MO, en Fe et en As par rapport au sol et à la solution du sol. Des analyses de NanoSIMS ont mis en évidence une distribution hétérogène des éléments et notamment de l'As. Il apparait diffus dans la matrice de l'échantillon mais également sous forme de 'hotspots' dans lesquels l'As est colocalisé soit avec le Fe, soit avec la

MO. La spéciation de l'As et du Fe ont été déterminée par XAS au seuil K de l'As et du Fe. Les principaux résultats ont montré que :

L'As(III) n'est que partiellement oxydé en As(V). L'acquisition de spectres XANES de l'As sur différents points de l'échantillon a montré, par le biais d'une 'linear combinaison fitting', que 65 à 100% de l'As était oxydés malgré les conditions oxydantes du milieu lors des prélèvements des échantillons.

Le Fe est la phase porteuse principale de l'As. La deuxième sphère de coordination de l'As, explorée par EXAFS, n'a montré que des voisins Fe. L'As se lie en bidentate mononucléaire (^{2}E) sur le Fer à une distance interatomique de 2.74-2.95 Å et en monodentate binucléaire ^{2}C à une distance de 3.28-3.43 Å. La colocalisation As-MO de certains hotspots observés en NanoSIMS n'a pas pu être expliquée.

La MO inhibe indirectement l'oxydation de l'As, catalysée par Fe, en influençant la nature de sa phase porteuse. La phase porteuse principale de l'As a été identifiée comme étant de la nano-lépidocrocite par la présence d'une distance Fe-Fe à 3.90 Å dans les spectres EXAFS au seuil K du Fe et par le faible nombre de voisins Fe extrapolés en comparaison d'une lépidocrocite de référence. La présence de MO inhibe la croissance cristalline des oxydes de Fe. Une autre fraction du Fe est également piégée dans la matrice de MO (distance Fe-C détectée à 2.77 Å) sous forme de monomères et/ou de petits polymères. La formation de ces phases de Fe (monomères, petits polymères et nano-oxydes) favorise le nombre de sites en ^{2}E par rapport à ceux en ^{2}C d'où la formation de complexes bidentates mononucléaires ^{2}E et la persistance d'As(III) dans l'échantillon naturel.

V.1.2 Spéciation de l'As lors de la réoxydation de la zone humide riparienne ?

Les solides oxydés sont issus d'un processus de réoxydation de la solution de sol produite en condition réductrice (saturation en eau du sol), via la chute des précipitations et l'augmentation de l'évapotranspiration. La première étape de cette réoxydation est la formation d'une suspension riche en produits oxydés du Fe et en MO. La formation de cette suspension est donc une étape clef dans la compréhension de la spéciation et de la mobilité de l'As. J'ai donc produit, au laboratoire, une solution de sol de zone humide réduite que j'ai ensuite réoxydée afin d'étudier la spéciation de l'As, du Fe et la composition de la MO. Pour cela, j'ai réalisé des fractionnements en taille et poids moléculaires de la suspension obtenue et analysé chaque fraction par XAS, HPLC-ICP-MS, MET et THM-GC-MS. Ce travail m'a permis d'aboutir aux conclusions suivantes :

L'As est majoritairement présent sous forme d'As(V). Les analyses d'EXAFS et d'HPLC-ICP-MS indiquent que l'As est majoritairement sous forme d'As(V). Cependant, un épaulement dans les spectres XANES des grosses fractions ainsi que les mesures en HPLC-ICP-MS sur les petites fractions indiquent qu'une fraction de l'As(III) subsiste, comme observé pour les échantillons naturels solides (Chapitre II).

Deux types de nano-phases semblent contrôler l'As. Dans les fractions colloïdales supérieures à 30 kDa, l'As est associé à des colloïdes Fe-MO alors que dans celles inférieure à 30 kDa, l'As est associé à des colloïdes plus riches en MO.

La fraction 0.2µm-30kDa est une fraction de transition. Cette fraction contient les concentrations les plus importantes en As et en Fe. Le Fe y est à la fois sous forme de nano-oxydes mais aussi sous forme de plus petits polymères, voire de monomères, comme le montre la présence de la distance Fe-C à 2.95 Å dans le spectre EXAFS. La quantité d'As présente montre le rôle clef de cette fraction dans sa spéciation et sa distribution.

La composition de la MO varie en fonction des fractions. La caractérisation de la MO au THM-GC-MS a montré que la fraction > 0.2 µm était composée de MO de haut poids moléculaire d'origine végétale et enrichie en acides gras dont la teneur en groupements COOH est importante. La

fraction < 0.2 µm, au contraire, est majoritairement formée de composés organiques dérivés de la lignine, plus humifiés et plus riches en groupements phénols ayant une forte affinité pour le Fe. Dans la plus petite fraction, les composés organiques sont issus majoritairement des activités microbiologiques.

Formation de complexes ternaires. Dans les fractions < 30kDa, le traitement des données EXAFS au seuil du Fe a mis en évidence la disparition de la distance Fe-Fe à 3.05 Å. Cette disparition indique que plus aucun nano-oxydes de Fe n'est présent dans ces fractions (résultats confirmés par MET). Par contre, une distance Fe-C entre 2.86 et 2.95 Å est mis en évidence. Elle suggère la présence de Fe sous forme de petits polymères (dimères et/ou trimères) liés à la MO. L'EXAFS au seuil K de l'As pour ces fractions <30kDa indiquent que la distance As-Fe à 3.35 Å est toujours présente et que l'As se complexe en partie sous forme de bidentates binucléaires aux polymères de Fe liés à la matière organique. Ce complexe à 3 membres démontre la présence de complexes ternaires dans les fractions <30kDa. Leur présence est d'ailleurs confirmée par les analyses SEC-ICP-MS qui montrent une co-élution de l'As, du Fe et de la MO.

Présence d'As organique. Les résultats EXAFS combinés à ceux de THM-GC-MS et d'HPLC-ICP-MS ont mis en évidence la présence d'As(V) organique dans toutes les fractions. Ces formes méthylées, comme le DMA, ou plus complexes comme l'AB, sont probablement d'origine biologique. Elles seraient produites par les organismes vivants (plantes, champignons, petits invertébrés) via des processus de métabolisme ou de détoxification. Ces formes organiques ne sont pas solubles mais liées aux phases colloïdales Fe-MO ou intégrées dans des fragments de la dégradation d'organismes vivants.

La mobilisation de l'As via les zones humides serait plus faible qu'attendu. Même si la fraction 0.2µm-30kDa est la plus concentrée en As, en considérant la masse totale que représente chaque fraction, la fraction particulaire (>0.2µm) est beaucoup plus importante que la fraction nanométriques (<0.2µm). Plus de 90 % de l'As est présent dans la fraction >3µm, soit lié à des particules soit intégré dans des particules biologiques. Du fait de leur taille ces particules

sédimentent très rapidement et ne sont donc pas mobiles. La fraction 0.2µm-30kDa reste cependant critique car même si elle contient une quantité plus faible d'As, cette concentration reste substantielle et elle peut être considérée comme beaucoup plus mobile.

V.1.3 La variation de la structure des agrégats Fe-MO influence l'adsorption de l'As

Les résultats décrits dans les parties précédentes ont mis en exergue le rôle des agrégats nanométriques Fe-MO dans la dynamique de l'As. Cependant, la structure physique de ces agrégats et leurs impacts sur l'adsorption de l'As restent très mal connus. Afin de simplifier le système naturel et ne considérer qu'une variable à la fois, nous avons synthétisé des agrégats nanométriques Fe-MO à différents rapports Fe/carbone organique (CO). Les structures de ces agrégats ont été étudiées par SANS/SAXS, EXAFS et MET. J'ai ensuite réalisé des expériences d'adsorption d'As, à un rapport As/Fe constant pour chaque agrégat, afin de tester l'impact de la structure sur leur capacité d'adsorption en As. Plusieurs résultats très intéressants peuvent être relevés :

Le Fe forme des agrégats fractals dans une matrice de MO. Une unité de base, appelée bille primaire mesurant 0.8 nm (petits polymères de Fe) s'associent pour former des agrégats intermédiaires (nano-oxydes) qui s'agrègent eux-mêmes en agrégats secondaires. La majorité des agrégats intermédiaires et probablement quelques billes primaires sont non associés dans les agrégats secondaires, c'est-à-dire isolés les uns des autres dans la MO.

Deux comportements de la MO peuvent être distingués. Une grande partie de la MO forme une phase continue de molécules organiques non agrégées dont certaines sont complexées au Fe(III) en tant que monomères, billes primaires et agrégats intermédiaires. Une autre partie de la MO est agrégée au sein des agrégats secondaires et forme un agrégat sphérique dense.

La taille des agrégats augmente avec le ratio Fe/CO. Avec l'augmentation du ratio Fe/CO de 0.1 à 0.4, les tailles des agrégats intermédiaires et de la partie Fe des agrégats secondaires augmentent en passant respectivement de 3.3 à 5.7 nm et de 131 à 689 nm. La partie MO des agrégats secondaires augmente également mais de façon moins prononcée (90 à 136 nm). La dimension fractale de l'agrégat intermédiaire augmente également, indiquant une compaction des

agrégats avec le rapport Fe/CO. Au contraire, la dimension fractale des agrégats secondaires (partie Fe) diminue, indiquant une ouverture de la structure.

L'adsorption de l'As augmente avec le rapport Fe/CO. Pour un rapport As/Fe constant, la quantité d'As adsorbé sur les agrégats Fe/MO augmente. Pourtant les calculs de la surface spécifique des agrégats secondaires ont montré que celle-ci était constante quel que soit le rapport Fe/CO.

L'augmentation du taux d'adsorption de l'As pourrait s'expliquer par une augmentation des forces de répulsion entre les agrégats intermédiaires contenus dans les agrégats secondaires. L'augmentation des distances entre agrégats intermédiaires augmenterait la disponibilité des sites d'adsorption de l'As. De plus, avec le rapport Fe/CO, la taille des agrégats intermédiaires au sein des agrégats secondaires augmente plus fortement que la taille de l'agrégat organique. Ainsi plus, le rapport est important, moins le taux de recouvrement des agrégats intermédiaires de Fe par l'agrégat organique est fort et plus le nombre de sites disponibles pour l'adsorption de l'As est important.

V.1.4 Les zones humides sources ou pièges d'As ?

Les zones humides subissent des alternances saisonnières de saturation/désaturation en eaux en lien avec les nappes d'eau de sub-surface et le système hydrographique de surface. En période de hautes eaux, le milieu se réduit et une dissolution réductrice des oxydes de Fe conduit à la libération de l'As dans la solution de sol. Les réactions de réduction entrainent également une solubilisation de la MO, via une augmentation du pH et la destruction des oxydes de Fe (Grybos et al., 2009). L'As(V) libéré est réduit en As(III) par des bactéries autochtones via des processus de détoxification ou de métabolisme (Dia et al., 2015). L'As(III) se trouve alors dans une solution riche en Fe(II) et en MO dans laquelle plusieurs processus peuvent contrôler sa spéciation, et cela en fonction des rapports de concentration entre As, Fe(II) et MO. L'As(III) peut 1) se complexer directement à la MO via ses sites thiols, si leur quantité le permet, 2) former des complexes ternaires As(III)-Fe(II)-MO (Catrouillet et al., 2014), 3) rester en solution, ou enfin 4) être mis en jeu dans des réactions

biologiques avec les organismes vivants qui développent des systèmes de détoxification pour s'adapter à sa présence en solution (Dembitsky and Rezanka, 2003).

Lorsque le niveau de l'eau baisse dans le sol de la zone humide, la diffusion de l'O_2 augmente et les conditions oxydantes sont rétablies. Les communautés bactériennes sont modifiées, les bactéries ferri-réductrices disparaissent en faveur des bactéries aérobies utilisant l'O_2. Les éléments chimiques redox sensibles tel que le Fe se réoxydent. Seulement, la solution de sol est très enrichie en MO, et cette présence contraint les espèces et la phase de Fe(III) en formation. Cette MO est très hétérogène avec des molécules de hauts poids moléculaires, peu dégradées, d'origine végétale et peu complexantes, et des fractions nanométriques (< 0.2 µm) composées de MO dégradée, plus humique, riche en phénol et plus complexante. Le Fe(III) forme ainsi des monomères, des petits polymères (dimères/trimères) et nano-oxydes complexés à la MO humique nanométrique. La complexation des nano-oxydes par la MO limite drastiquement la croissance cristalline de l'oxyde de Fe formé. Si l'on extrapole les données obtenues avec notre système modèle Fe-MO (Chapitre IV), il est possible de considérer que ces nano-oxydes sont en fait des agrégats de quelques dizaines de nm. Une majorité d'entre eux sont dispersés dans la matrice de MO non agrégée. Les autres se sont agrégés pour former de plus gros agrégats secondaires dont la taille varie entre 100 et presque 1000 nm et qui sont de plus en plus ramifiés et au sein desquels la MO, elle-même, s'est agrégée en un gros agrégat sphérique et dense dont la taille peut varier entre 50 et 100 nm. L'As s'adsorbe en grande quantité sur les agrégats de Fe dispersés ou agrégés. Son taux d'adsorption varie en fonction de la disponibilité des sites de complexation qui pourrait dépendre des distances inhérentes aux répulsions entre les agrégats au sein des agrégats secondaires ou encore du taux de recouvrement des agrégats de Fe par la MO au sein des agrégats secondaires. L'As, le Fe et la MO forment donc des complexes ternaires. Le Fe(III) est oxydé et précipite avec l'As(III), une partie de l'As a donc été adsorbé sur les agrégats de Fe sous forme d'As(III). S'il a formé des complexes bidentates binucléaires ^{2}C avec les agrégats de Fe, l'As(III) est réoxydé en As(V) mais s'il s'est complexé sous forme de bidentates mononucléaires ^{2}E alors il est conservé, complexé sous forme d'As(III).

Une autre fraction de l'As (III) est intégrée dans le métabolisme des végétaux, champignons et petits invertébrés et autres bactéries qui le transforment en espèce organique via des processus de détoxification par méthylation oxydative. L'As peut également former des molécules organiques plus complexes en se combinant à des sucres ou des lipides dans les organismes. Une partie de l'As méthylé est exsudé et se complexe probablement aux agrégats de Fe alors qu'une autre partie est intégrée dans les organismes et se retrouve dans la phase particulaire du sol lorsqu'ils sont dégradés.

A l'issue de l'oxydation mais avant l'assèchement du sol, l'As est donc présent dans une suspension hétérogène sous forme :

1. As(V) organique intégré dans du matériel biologique particulaire,
2. As(V) organique ou As(V, III) inorganique associé à des agrégats secondaires de Fe/MO dont la taille peut atteindre près de 1000 nm,
3. As(V) organique et As(V, III) complexé à des agrégats de Fe, eux-mêmes complexés à des molécules organiques de quelques nm,
4. As(V) organique et As(V, III) complexé à des petits polymères de Fe (dimères , trimères, etc.) complexés à des molécules organiques.

Dans les deux premiers cas, l'As est lié à des particules qui sédiment rapidement et ne pourra donc pas être transféré hors de la zone humide. Dans les deux derniers cas, le transfert de l'As vers les rivières ou la nappe dépendra entièrement de la capacité des nano agrégats et des polymères piégés par des processus physiques et biogéochimiques dans la porosité du sol. Mais l'étude réalisée dans le chapitre II montre qu'une partie de ces agrégats se dépose dans la porosité du sol après assèchement du sol. En effet, si l'on compare les données EXAFS des solides de terrain et ceux des fractions, une partie des solides de terrain est composée de petits polymères de Fe, d'agrégats de Fe et d'agrégats de Fe secondaires qui sont dans ce cas tous agglomérés. Enfin, les bilans massiques des fractions montrent que les fractions particulaires contrôlent plus de 90% de l'As total produit lors de la réduction du sol de ZH. La proportion d'As potentiellement exportée vers les aquifères ou la rivière est donc faible. Les ZH ont ainsi la capacité de se comporter comme des puits importants d'As.

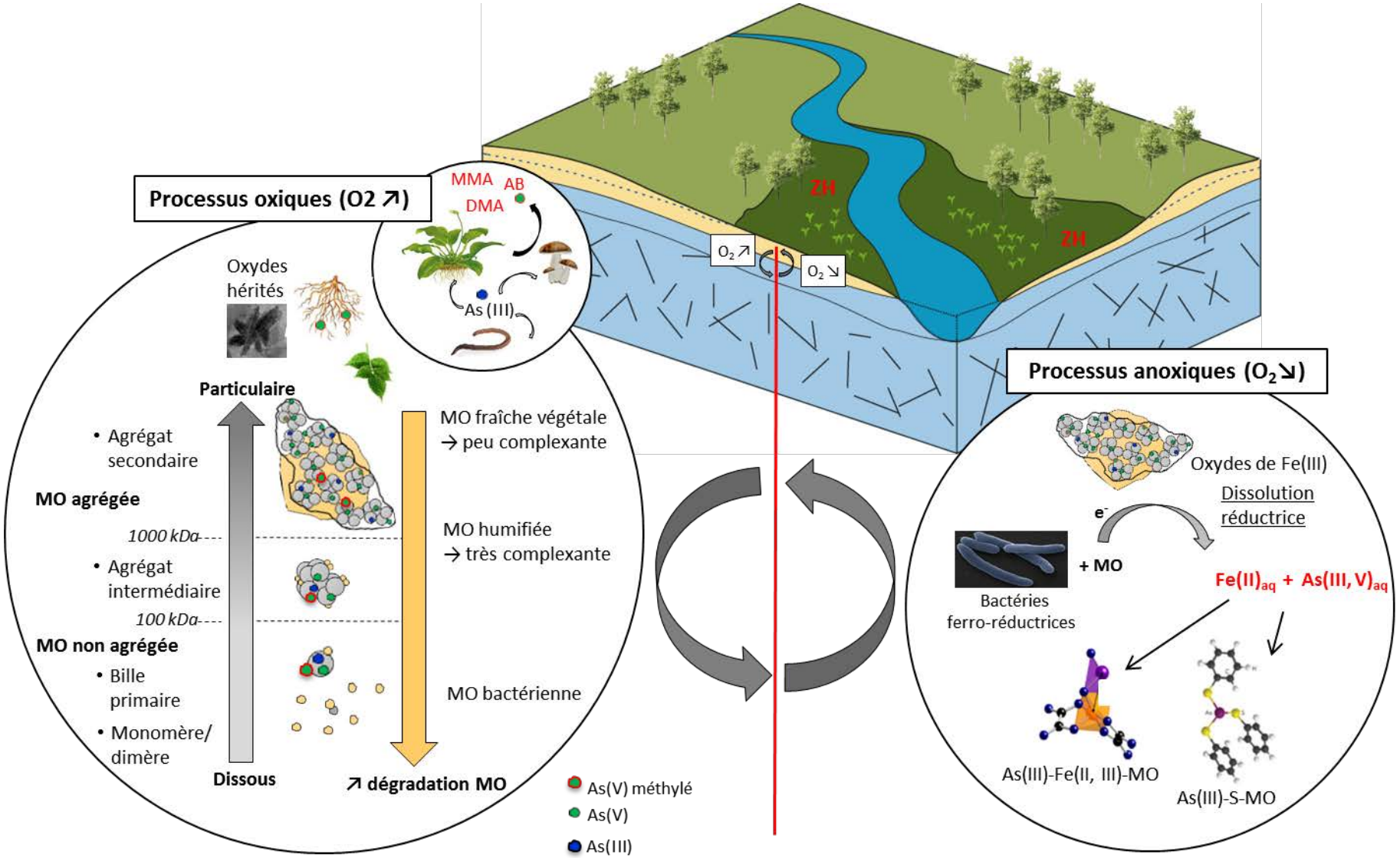

Figure V Schéma récapitulatif des processus d'oxydo-réduction au sein d'une zone humide (ZH) lors de l'alternance de saturation et désaturation en eau.

V.2 Perspectives

V.2.1 Influence de paramètres physico-chimiques sur la structure des agrégats Fe-MO

Le troisième chapitre de cette thèse m'a permis de montrer que la technique de diffusion de neutron aux petits angles (SANS) était parfaitement adaptée à l'analyse d'échantillons mixtes Fe-MO de taille nanométrique. En utilisant le principe de la variation de contraste, le SANS permet de sonder soit la composante Fe soit la composante MO des agrégats et de suivre leur évolution de structure indépendamment. Dans l'environnement, de nombreux paramètres physico-chimiques varient lors des changements de conditions d'oxydoréduction : le pH, la force ionique, la charge en cations et en anions, etc. Il serait donc intéressant de modifier un à un ces facteurs dans notre système modèle afin de simuler au mieux les évolutions naturelles de la structure des agrégats Fe-MO.

La MO naturelle est chimiquement complexe et très hétérogène. Elle peut être composée d'acides humiques/fulviques, acides gras, monosaccarides, sucres, acides aminés, etc. Dans notre composé synthétique mixte, nous n'avons considéré que les acides humiques. En effet, ils représentent une part importante du cycle global du carbone et constituent la majeure partie du carbone organique des solutions de sol : jusqu'à 60 % du carbone organique dissous (COD) dans la majorité des eaux de sol et jusqu'à 90% du COD dans les tourbières (Thurman, 1985). Les acides humiques peuvent donc être représentatifs de la MO naturelle. Cependant, il serait intéressant de faire une synthèse d'agrégats mixtes Fe/MO en utilisant différents mélanges de composés organiques pour déterminer l'influence de la composition de la MO dans la construction des agrégats Fe/MO.

V.2.2 Application de la diffusion de neutrons aux systèmes naturels

Une perspective intéressante serait d'adapter les paramètres de la variation de contraste obtenue pour les échantillons synthétiques sur des échantillons naturels. La difficulté de mesurer des échantillons naturels est leur faible concentration, ce qui peut parfois nécessiter une préconcentration avant mesure. La concentration minimum idéale est de 1% w/w. Certains auteurs

préconisent l'ultrafiltration pour éviter d'utiliser le séchage qui change la structure des agrégats. Deux possibilités s'offrent ainsi à nous, 1) la solution réduite peut être prélevée sur le terrain puis réoxydée en laboratoire ou 2) le sol de la zone humide peut être incubé en chambre anaérobie puis la solution réduite obtenue réoxydée. Les agrégats en suspension pourront être mis en perspective avec les modèles Fe-MO (dimension fractale, rayon géométrique des particules, etc.) obtenues avec des solutions synthétiques à des ratios Fe/CO similaires au milieu naturel.

V.2.3 Confirmation de la libération de sites d'adsorption dans les agrégats secondaires

Lors de l'augmentation du ratio Fe/CO, nous avons fait l'hypothèse que les distances entre les agrégats intermédiaires au sein des agrégats secondaires étaient de plus en plus grandes. Ainsi, des sites se libèrent pour l'adsorption de l'As ce qui permettrait d'expliquer l'augmentation de l'adsorption de l'As avec l'augmentation du rapport Fe/CO (à ratio As/Fe constant). La DLS, utilisée sur le ratio Fe/CO de 0.4, a permis de détecter les seuils de coupure séparant les agrégats secondaires des agrégats intermédiaires. Pour pouvoir confirmer notre hypothèse sur les distances et donc que la variation du pourcentage d'adsorption concerne les agrégats secondaires, il serait nécessaire de faire des expériences d'adsorption d'As (au même ratio As/Fe de 0.005) sur des agrégats synthétisés à plusieurs ratios Fe/CO. Chaque nouvelle suspension devra être ultrafiltrée à 1000 kDa (pour séparer les agrégats secondaires) et à 100 kDa (pour séparer les agrégats intermédiaires) puis analyser la concentration en Fe, MO et As dans chaque fraction. Je m'attends à observer une proportion de l'As adsorbé sur les agrégats secondaires qui augmente avec le rapport Fe/CO.

V.2.4 Mesures dynamiques de spéciation du Fe lors de la formation des agrégats Fe-MO

La conformation et la taille des agrégats Fe-MO contrôle leur capacité d'adsorption comme je l'ai montré dans le quatrième chapitre de ce travail de thèse. Cependant les mécanismes exacts de formation et d'agrégation de ces colloïdes ne sont pas entièrement compris. Une expérience a été programmée au synchrotron SOLEIL (Saclay, France) sur la ligne ROCK afin de caractériser la phase du

Fe (à travers sa spéciation) tout le long de la réaction d'oxydation/hydrolyse du Fe en présence de MO. Cette ligne de lumière est une ligne de spectroscopie d'absorption X en mode quick-XAS qui permet d'étudier *in situ* des processus cinétiques rapides. L'objectif de cette expérimentation sera d'observer les étapes de formation des agrégats Fe-MO et les premiers mécanismes instigateurs de l'association étroite entre le Fe et la MO.

V.2.5 Adaptation des processus déterminés à un autre environnement de zone humide

Les deux premières parties de ce travail de thèse se sont intéressées à une zone humide riparienne très bien caractérisée pédo-hydro-climato et géochimiquement, et dont la recharge en eau se fait essentiellement par la remontée de la nappe. D'autres zones humides avec un fonctionnement différent seraient intéressantes à étudier et comparer en termes de dynamique des éléments Fe, As et MO, comme les plaines d'inondation dans lesquelles la recharge en eau se fait par un apport des rivières lors des crues. Dans ces zones, comme la plaine d'inondation du Mékong, la biomasse est très différente de celle des zones humides ripariennes. La composition de la MO produite par la décomposition de cette biomasse devrait alors être différente de celle de notre zone d'étude, donc peut-être avoir des propriétés différentes (complexation, agrégation, etc.). Les sédiments dont sont issus les oxyhydroxides de Fe porteurs d'As sont apportés en masse par le fleuve Mékong puis déposés dans les plaines d'inondation alors que dans la zone humide riparienne ces sédiments sont *in situ* dans l'aquifère. Il peut en résulter, entre autres, une différence dans les rapports de concentration des éléments entre les deux zones humides. Ainsi, il serait judicieux de construire des relations internationales avec les pays limitrophes du fleuve Mékong en Asie du Sud-Est pour confronter les mécanismes régissant le comportement de l'As entre ces deux types de zone humide.

Bibliographie

Abernathy, C.O., Liu, Y.-P., Longfellow, D., Aposhian, H.V., Beck, B., Fowler, B., Goyer, R., Menzer, R., Rossman, T., Thompson, C., others, 1999. Arsenic: health effects, mechanisms of actions, and research issues. Environ. Health Perspect. 107, 593.

AFNOR, 1982. Essais des eaux - Dosage du fer - Méthode spectrométrique à la phénantroline-1,10.

Allard, T., Menguy, N., Salomon, J., Calligaro, T., Weber, T., Calas, G., Benedetti, M.F., 2004. Revealing forms of iron in river-borne material from major tropical rivers of the Amazon Basin (Brazil). Geochim. Cosmochim. Acta 68, 3079–3094.

Al-Sid-Cheikh, M., Pédrot, M., Dia, A., Guenet, H., Vantelon, D., Davranche, M., Gruau, G., Delhaye, T., 2015. Interactions between natural organic matter, sulfur, arsenic and iron oxides in re-oxidation compounds within riparian wetlands: NanoSIMS and X-ray adsorption spectroscopy evidences. Sci. Total Environ. 515-516, 118–128. doi:10.1016/j.scitotenv.2015.02.047

Anawar, H.M., Akai, J., Komaki, K., Terao, H., Yoshioka, T., Ishizuka, T., Safiullah, S., Kato, K., 2003. Geochemical occurrence of arsenic in groundwater of Bangladesh: sources and mobilization processes. J. Geochem. Explor. 77, 109–131. doi:10.1016/S0375-6742(02)00273-X

Arai, Y., Elzinga, E.J., Sparks, D.L., 2001. X-ray Absorption Spectroscopic Investigation of Arsenite and Arsenate Adsorption at the Aluminum Oxide–Water Interface. J. Colloid Interface Sci. 235, 80–88. doi:10.1006/jcis.2000.7249

Arčon, I., van Elteren, J.T., Glass, H.J., Kodre, A., Šlejkovec, Z., 2005. EXAFS and XANES study of arsenic in contaminated soil. X-Ray Spectrom. 34, 435–438. doi:10.1002/xrs.857

Aström, M., Corin, N., 2000. Abundance, sources and speciation of trace elements in humus-rich streams affected by acid sulphate soils. Aquat. Geochem. 6, 367–383.

Auffan, M., Rose, J., Proux, O., Borschneck, D., Masion, A., Chaurand, P., Hazemann, J.-L., Chaneac, C., Jolivet, J.-P., Wiesner, M.R., Van Geen, A., Bottero, J.-Y., 2008. Enhanced Adsorption of Arsenic onto Maghemites Nanoparticles: As(III) as a Probe of the Surface Structure and Heterogeneity. Langmuir 24, 3215–3222. doi:10.1021/la702998x

Baigorri, R., Fuentes, M., González-Gaitano, G., García-Mina, J.M., 2007. Analysis of molecular aggregation in humic substances in solution. Colloids Surf. Physicochem. Eng. Asp. 302, 301–306. doi:10.1016/j.colsurfa.2007.02.048

Bardelli, F., Benvenuti, M., Costagliola, P., Di Benedetto, F., Lattanzi, P., Meneghini, C., Romanelli, M., Valenzano, L., 2011. Arsenic uptake by natural calcite: An XAS study. Geochim. Cosmochim. Acta 75, 3011–3023. doi:10.1016/j.gca.2011.03.003

Bauer, M., Blodau, C., 2009. Arsenic distribution in the dissolved, colloidal and particulate size fraction of experimental solutions rich in dissolved organic matter and ferric iron. Geochim. Cosmochim. Acta 73, 529–542. doi:10.1016/j.gca.2008.10.030

Bauer, M., Blodau, C., 2006. Mobilization of arsenic by dissolved organic matter from iron oxides, soils and sediments. Sci. Total Environ. 354, 179–190. doi:10.1016/j.scitotenv.2005.01.027

Belzile, N., De Vitre, R.R., Tessier, A., 1989. In situ collection of diagenetic iron and manganese oxyhydroxdes from natural sediments. Nature 340, 376–377.

Bolte, S., Cordelieres, F.P., 2006. A guided tour into subcellular colocalization analysis in light microscopy. J. Microsc. 224, 213–232.

Bottero, J.Y., Manceau, A., Villieras, F., Tchoubar, D., 1994. Structure and mechanisms of formation of FeOOH(Cl) polymers. Langmuir 10.

Bourrié, G., Trolard, F., Jaffrezic, J.-M.R.G., Maître, V., Abdelmoula, M., 1999. Iron control by equilibria between hydroxy-green rusts and solutions in hydromorphic soils. Geochim. Cosmochim. Acta 63, 3417–3427.

Bowell, R.J., 1994. Sorption of arsenic by iron oxides and oxyhydroxides in soils. Appl. Geochem. 9, 279–286.

Brûlet, A., Lairez, D., Lapp, A., Cotton, J.-P., 2007. Improvement of data treatment in small-angle neutron scattering. J. Appl. Crystallogr. 40, 165–177.

Buffle, J., Wilkinson, K.J., Stoll, S., Filella, M., Zhang, J., 1998. A generalized description of aquatic colloidal interactions: the three-colloidal component approach. Environ. Sci. Technol. 32, 2887–2899.

Buschmann, J., Kappeler, A., Lindauer, U., Kistler, D., Berg, M., Sigg, L., 2006. Arsenite and arsenate binding to dissolved humic acids: Influence of pH, type of humic acid, and aluminum. Environ. Sci. Technol. 40, 6015–6020.

Catrouillet, C., Davranche, M., Dia, A., Bouhnik-Le Coz, M., Demangeat, E., Gruau, G., 2016. Does As(III) interact with Fe(II), Fe(III) and organic matter through ternary complexes? J. Colloid Interface Sci. 470, 153–161. doi:10.1016/j.jcis.2016.02.047

Catrouillet, C., Davranche, M., Dia, A., Bouhnik-Le Coz, M., Marsac, R., Pourret, O., Gruau, G., 2014. Geochemical modeling of Fe(II) binding to humic and fulvic acids. Chem. Geol. 372, 109–118. doi:10.1016/j.chemgeo.2014.02.019

Catrouillet, C., Davranche, M., Dia, A., Bouhnik-Le Coz, M., Pédrot, M., Marsac, R., Gruau, G., 2015. Thiol groups controls on arsenite binding by organic matter: New experimental and modeling evidence. J. Colloid Interface Sci. 460, 310–320. doi:10.1016/j.jcis.2015.08.045

Chen, C., Kukkadapu, R., Sparks, D.L., 2015. Influence of Coprecipitated Organic Matter on $Fe^{2+}_{(aq)}$ -Catalyzed Transformation of Ferrihydrite: Implications for Carbon Dynamics. Environ. Sci. Technol. 49, 10927–10936. doi:10.1021/acs.est.5b02448

Combes, J.M., Manceau, A., Calas, G., Bottero, J.Y., 1989. Formation of ferric oxides from aqueous solutions: A polyhedral approach by X-ray absorption spectroscopy: 1. Hydrolysis and formation of ferric gels. Geochim. Cosmochim. Acta 53, 583–594.

Cornell, R.M., Schwertmann, U., 2003. The Iron Oxides: Structures, Properties, Reactions, Occurence and Uses, VCH. ed. Weinheim, Germany.

Couture, R.-M., Wallschläger, D., Rose, J., Van Cappellen, P., 2013. Arsenic binding to organic and inorganic sulfur species during microbial sulfate reduction: a sediment flow-through reactor experiment. Environ. Chem. 10, 285. doi:10.1071/EN13010

Cox, C.D., Ghosh, M.M., 1994. Surface complexation of methylated arsenate by hydrous oxides. Water Res. 28, 1181–1188.

Cranwell, P.A., 1974. Monocarboxylic acids in lake sediments: indicators, derived from terrestrial and aquatic biota, of paleoenvironmental trophic levels. Chem. Geol. 14, 1–14.

Cullen, W.R., Reimer, K.J., 1989. Arsenic Speciation in the Environment. Chem. Rev. 89, 713–764.

Dahlqvist, R., Andersson, K., Ingri, J., Larsson, T., Stolpe, B., Turner, D., 2007. Temporal variations of colloidal carrier phases and associated trace elements in a boreal river. Geochim. Cosmochim. Acta 71, 5339–5354. doi:10.1016/j.gca.2007.09.016

Davranche, M., Dia, A., Fakih, M., Nowack, B., Gruau, G., Ona-nguema, G., Petitjean, P., Martin, S., Hochreutener, R., 2013. Organic matter control on the reactivity of Fe(III)-oxyhydroxides and associated As in wetland soils: A kinetic modeling study. Chem. Geol. 335, 24–35. doi:10.1016/j.chemgeo.2012.10.040

Davranche, M., Grybos, M., Gruau, G., Pédrot, M., Dia, A., Marsac, R., 2011. Rare earth element patterns: A tool for identifying trace metal sources during wetland soil reduction. Chem. Geol. 284, 127–137. doi:10.1016/j.chemgeo.2011.02.014

Dembitsky, V.M., Rezanka, T., 2003. Natural occurrence of arseno compounds in plants, lichens, fungi, algal species, and microorganisms. Plant Sci. 165, 1177–1192. doi:10.1016/j.plantsci.2003.08.007

Desai, A.G., Milburn, R.M., 1969. Iron(III)-Phenol Complexes. IV. Further thermodynamics studies of iron(III)-phenolate and proton-phenolate associations. J. Am. Chem. Soc. 91, 1958–1961.

Dia, A., Gruau, G., Olivié-Lauquet, G., Riou, C., Molénat, J., Curmi, P., 2000. The distribution of rare earth elements in groundwaters: assessing the role of source-rock composition, redox changes and colloidal particles. Geochim. Cosmochim. Acta 64, 4131–4151.

Dia, A., Lauga, B., Davranche, M., Fahy, A., Duran, R., Nowack, B., Petitjean, P., Henin, O., Martin, S., Marsac, R., Gruau, G., 2015. Bacteria-mediated reduction of As(V)-doped lepidocrocite in a flooded soil sample. Chem. Geol. 406, 34–44. doi:10.1016/j.chemgeo.2015.04.008

Dixit, S., Hering, J.G., 2003. Comparison of Arsenic(V) and Arsenic(III) Sorption onto Iron Oxide Minerals: Implications for Arsenic Mobility. Environ. Sci. Technol. 37, 4182–4189. doi:10.1021/es030309t

Dobran, S., Zagury, G.J., 2006. Arsenic speciation and mobilization in CCA-contaminated soils: Influence of organic matter content. Sci. Total Environ. 364, 239–250. doi:10.1016/j.scitotenv.2005.06.006

Downward, L., Booth, C.H., Lukens, W.W., Bridges, F., 2006. A variation of the F-test for determining statistical relevance of particular parameters in EXAFS fits. Lawrence Berkeley Natl. Lab.

Du Laing, G., Rinklebe, J., Vandecasteele, B., Meers, E., Tack, F.M.G., 2009. Trace metal behaviour in estuarine and riverine floodplain soils and sediments: A review. Sci. Total Environ. 407, 3972–3985. doi:10.1016/j.scitotenv.2008.07.025

Eary, L.E., Schramke, J.A., 1990. Rates of Inorganic Oxidation Reactions Involving Dissolved Oxygen, in: Chemical Modeling of Aqueous Systems II. American Chemical Society, pp. 379–396.

Engel, A.S., Johnson, L.R., Porter, M.L., 2013. Arsenite oxidase gene diversity among *C hloroflexi* and *P roteobacteria* from El Tatio Geyser Field, Chile. FEMS Microbiol. Ecol. 83, 745–756. doi:10.1111/1574-6941.12030

Farquhar, M.L., Charnock, J.M., Livens, F.R., Vaughan, D.J., 2002. Mechanisms of Arsenic Uptake from Aqueous Solution by Interaction with Goethite, Lepidocrocite, Mackinawite, and Pyrite: An X-ray Absorption Spectroscopy Study. Environ. Sci. Technol. 36, 1757–1762. doi:10.1021/es010216g

Fendorf, S., 2010. Arsenic chemistry in soils and sediments. Lawrence Berkeley Natl. Lab.

Fendorf, S., Eick, M.J., Grossl, P., Sparks, D.L., 1997. Arsenate and chromate retention mechanisms on goethite. 1. Surface structure. Environ. Sci. Technol. 31, 315–320.

Flank, A.-M., Cauchon, G., Lagarde, P., Bac, S., Janousch, M., Wetter, R., Dubuisson, J.-M., Idir, M., Langlois, F., Moreno, T., Vantelon, D., 2006. LUCIA, a microfocus soft XAS beamline. Nucl. Instrum. Methods Phys. Res. Sect. B Beam Interact. Mater. At. 246, 269–274. doi:10.1016/j.nimb.2005.12.007

Foster, A.L., Kim, C.S., 2014. Arsenic Speciation in Solids Using X-ray Absorption Spectroscopy. Rev. Mineral. Geochem. 79, 257–369. doi:10.2138/rmg.2014.79.5

Francesconi, K.A., Kuehnelt, D., 2002. Arsenic compounds in the environment, Frankenberger WT Jr. ed, Environmental Chemistry of Arsenic. Marcel Dekker, New-York.

Frohne, T., Rinklebe, J., Diaz-Bone, R.A., 2014. Contamination of Floodplain Soils along the Wupper River, Germany, with As, Co, Cu, Ni, Sb, and Zn and the Impact of Pre-definite Redox Variations on the Mobility of These Elements. Soil Sediment Contam. Int. J. 23, 779–799. doi:10.1080/15320383.2014.872597

Geiszinger, A., Goessler, W., Kosmus, W., 2002. Organoarsenic compounds in plants and soil on top of an ore vein. Appl. Organomet. Chem. 16, 245–249. doi:10.1002/aoc.294

Geiszinger, A., Goessler, W., Kuehnelt, D., Francesconi, K., Kosmus, W., 1998. Determination of Arsenic Compounds in Earthworms. Environ. Sci. Technol. 32, 2238–2243.

George, G.N., Pickering, I.J., 2007. X-ray absorption spectroscopy in biology and chemistry, in: Brilliant Light in Life and Material Sciences. Springer, pp. 97–119.

Goldberg, S., 2002. Competitive adsorption of arsenate and arsenite on oxides and clay minerals. Soil Sci. Soc. Am. J. 66, 413–421.

Grafe, M., Eick, M.J., Grossl, P.R., 2001. Adsorption of arsenate (V) and arsenite (III) on goethite in the presence and absence of dissolved organic carbon. Soil Sci. Soc. Am. J. 65, 1680–1687.

Greenleaf, J.E., Cumbal, L., Staina, I., Sengupta, A.K., 2003. Abiotic As(III) oxidation by hydrated Fe(III) oxide (HFO) microparticles in a plug flow columnar configuration. Process Saf. Environ. Prot. 81, 87–98.

Gruau, G., Dia, A., Olivié-Lauquet, G., Davranche, M., Pinay, G., 2004. Controls on the distribution of rare earth elements in shallow groundwaters. Water Res. 38, 3576–3586. doi:10.1016/j.watres.2004.04.056

Grybos, M., Davranche, M., Gruau, G., Petitjean, P., 2007. Is trace metal release in wetland soils controlled by organic matter mobility or Fe-oxyhydroxides reduction? J. Colloid Interface Sci. 314, 490–501. doi:10.1016/j.jcis.2007.04.062

Grybos, M., Davranche, M., Gruau, G., Petitjean, P., Pédrot, M., 2009. Increasing pH drives organic matter solubilization from wetland soils under reducing conditions. Geoderma 154, 13–19. doi:10.1016/j.geoderma.2009.09.001

Gu, B., Schmitt, J., Chen, Z., Liang, L., McCarthy, J.F., 1995. Adsorption and desorption of different organic matter fractions on iron oxide. Geochim. Cosmochim. Acta 59, 219–229.

Guénet, H., Davranche, M., Vantelon, D., Pédrot, M., Al-Sid-Cheikh, M., Dia, A., Jestin, J., 2016. Evidence of organic matter control on As oxidation by iron oxides in riparian wetlands. Chem. Geol. 439, 161–172. doi:10.1016/j.chemgeo.2016.06.023

Guinier, A., Fournet, G., 1955. , Wiley Intersciences. ed. New-York.

Guo, H., Zhang, B., Zhang, Y., 2011. Control of organic and iron colloids on arsenic partition and transport in high arsenic groundwaters in the Hetao basin, Inner Mongolia. Appl. Geochem. 26, 360–370. doi:10.1016/j.apgeochem.2010.12.009

Gustafsson, J.P., 2001. Modeling the Acid–Base Properties and Metal Complexation of Humic Substances with the Stockholm Humic Model. J. Colloid Interface Sci. 244, 102–112. doi:10.1006/jcis.2001.7871

Harvey, C.F., Ashfaque, K.N., Yu, W., Badruzzaman, A.B.M., Ali, M.A., Oates, P.M., Michael, H.A., Neumann, R.B., Beckie, R., Islam, S., Ahmed, M.F., 2006. Groundwater dynamics and arsenic contamination in Bangladesh. Chem. Geol. 228, 112–136. doi:10.1016/j.chemgeo.2005.11.025

Hasegawa, H., 1997. The behavior of trivalent and pentavalent methylarsenicals in Lake Biwa. Appl. Organomet. Chem. 11, 305–311.

Hazemann, J.-L., Bérar, J.F., Manceau, A., 1991. Rietveld Studies of the Aluminium-Iron Substitution in Synthetic Goethite. Mater. Sci. Forum 79-82, 821–826.

Hedges, J.I., Parker, P.L., 1976. Land-derived organic matter in surface sediments from the Gulf of Mexico. Geochim. Cosmochim. Acta 40, 1019–1029.

Hiemstra, T., van Riemsdijk, W.H., 2007. Adsorption and surface oxidation of Fe(II) on metal (hydr)oxides. Geochim. Cosmochim. Acta 71, 5913–5933. doi:10.1016/j.gca.2007.09.030

Hoffmann, M., Mikutta, C., Kretzschmar, R., 2014. Arsenite binding to sulfhydryl groups in the absence and presence of ferrihydrite: a model study. Environ. Sci. Technol. 48, 3822–3831.

Hoffmann, M., Mikutta, C., Kretzschmar, R., 2013. Arsenite Binding to Natural Organic Matter: Spectroscopic Evidence for Ligand Exchange and Ternary Complex Formation. Environ. Sci. Technol. 47, 12165–12173. doi:10.1021/es4023317

Hoffmann, M., Mikutta, C., Kretzschmar, R., 2012. Bisulfide Reaction with Natural Organic Matter Enhances Arsenite Sorption: Insights from X-ray Absorption Spectroscopy. Environ. Sci. Technol. 46, 11788–11797. doi:10.1021/es302590x

Hofmann, A., Pelletier, M., Michot, L., Stradner, A., Schurtenberger, P., Kretzschmar, R., 2004. Characterization of the pores in hydrous ferric oxide aggregates formed by freezing and thawing. J. Colloid Interface Sci. 271, 163–173. doi:10.1016/j.jcis.2003.11.053

Horcajada, P., Surble, S., Serre, C., Hong, D.-Y., Seo, Y.K., Chang, J.S., Greneche, J.M., Margiolaki, I., Ferey, G., 2007. Synthesis and catalytic properties of MIL-100(Fe), an iron(iii) carboxylate with large pores. Chem. Commun. 2820. doi:10.1039/b704325b

Huang, J.-H., Matzner, E., 2007. Biogeochemistry of Organic and Inorganic Arsenic Species in a Forested Catchment in Germany. Environ. Sci. Technol. 41, 1564–1569. doi:10.1021/es061586d

Huang, J.-H., Scherr, F., Matzner, E., 2007. Demethylation of Dimethylarsinic Acid and Arsenobetaine in Different Organic Soils. Water. Air. Soil Pollut. 182, 31–41. doi:10.1007/s11270-006-9318-4

Huguet, A., Vacher, L., Relexans, S., Saubusse, S., Froidefond, J.M., Parlanti, E., 2009. Properties of fluorescent dissolved organic matter in the Gironde Estuary. Org. Geochem. 40, 706–719. doi:10.1016/j.orggeochem.2009.03.002

Ilina, S.M., Poitrasson, F., Lapitskiy, S.A., Alekhin, Y.V., Viers, J., Pokrovsky, O.S., 2013. Extreme iron isotope fractionation between colloids and particles of boreal and temperate organic-rich waters. Geochim. Cosmochim. Acta 101, 96–111. doi:10.1016/j.gca.2012.10.023

Jain, C., Ali, I., 2000. Arsenic: occurrence, toxicity and speciation techniques 34.

Janot, N., Reiller, P.E., Benedetti, M.F., 2013. Modelling Eu(III) speciation in a Eu(III)/PAHA/α-Al2O3 ternary system. Colloids Surf. Physicochem. Eng. Asp. 435, 9–15. doi:10.1016/j.colsurfa.2013.02.052

Jarvie, H.P., King, S.M., 2007. Small-Angle Neutron Scattering Study of Natural Aquatic Nanocolloids. Environ. Sci. Technol. 41, 2868–2873. doi:10.1021/es061912p

Jiang, Z., Li, P., Jiang, D., Wu, G., Dong, H., Wang, Y., Li, B., Wang, Y., Guo, Q., 2014. Diversity and abundance of the arsenite oxidase gene aioA in geothermal areas of Tengchong, Yunnan, China. Extremophiles 18, 161–170. doi:10.1007/s00792-013-0608-7

Kalbitz, K., Wennrich, R., 1998. Mobilization of heavy metals and arsenic in polluted wetland soils and its dependence on dissolved organic matter. Sci. Total Environ. 209, 27–39.

Karlsson, T., Persson, P., 2012. Complexes with aquatic organic matter suppress hydrolysis and precipitation of Fe(III). Chem. Geol. 322-323, 19–27. doi:10.1016/j.chemgeo.2012.06.003

Karlsson, T., Persson, P., 2010. Coordination chemistry and hydrolysis of Fe(III) in a peat humic acid studied by X-ray absorption spectroscopy. Geochim. Cosmochim. Acta 74, 30–40. doi:10.1016/j.gca.2009.09.023

Kim, J.-I., Buckau, G., Li, G.H., Duschner, H., Psarros, N., 1990. Characterization of humic and fulvic acids from Gorleben groundwater. Fresenius J. Anal. Chem. 338, 245–252.

Kitahama, K., Kiriyama, R., Baba, Y., 1975. Refinement of crystal-structure of scorodite. Acta Crystallogr. Sect. B-Struct. Sci. 31, 322–324.

Kocar, B.D., Polizzotto, M.L., Benner, S.G., Ying, S.C., Ung, M., Ouch, K., Samreth, S., Suy, B., Phan, K., Sampson, M., Fendorf, S., 2008. Integrated biogeochemical and hydrologic processes driving arsenic release from shallow sediments to groundwaters of the Mekong delta. Appl. Geochem. 23, 3059–3071. doi:10.1016/j.apgeochem.2008.06.026

Kretzschmar, R., Schäfer, T., 2005. Metal retention and transport on colloidal particles in the environment. Elements 1, 205–210.

Langner, P., Mikutta, C., Kretzschmar, R., 2012. Arsenic sequestration by organic sulphur in peat. Nat. Geosci. 5, 66–73. doi:10.1038/ngeo1329

Langner, P., Mikutta, C., Kretzschmar, R., 2011. Arsenic sequestration by organic sulphur in peat. Nat. Geosci. 5, 66–73. doi:10.1038/ngeo1329

Larese-Casanova, P., Scherer, M.M., 2007. Fe (II) sorption on hematite: New insights based on spectroscopic measurements. Environ. Sci. Technol. 41, 471–477.

Lenoble, V., Laclautre, C., Deluchat, V., Serpaud, B., Bollinger, J.-C., 2005. Arsenic removal by adsorption on iron(III) phosphate. J. Hazard. Mater. 123, 262–268. doi:10.1016/j.jhazmat.2005.04.005

Lewis, W.M., 1995. Wetlands: characteristics and boundaries. Natl Academy Pr.

Liang, L., McCarthy, J.F., Jolley, L.W., McNabb, J.A., Mehlhorn, T.L., 1993. Iron dynamics: Transformation of Fe (II)/Fe (III) during injection of natural organic matter in a sandy aquifer. Geochim. Cosmochim. Acta 57, 1987–1999.

Lippold, H., Lippmann-Pipke, J., 2009. Effect of humic matter on metal adsorption onto clay materials: Testing the linear additive model. J. Contam. Hydrol. 109, 40–48. doi:10.1016/j.jconhyd.2009.07.009

Liu, G., Cai, Y., 2010. Complexation of arsenite with dissolved organic matter: Conditional distribution coefficients and apparent stability constants. Chemosphere 81, 890–896. doi:10.1016/j.chemosphere.2010.08.002

Liu, G., Fernandez, A., Cai, Y., 2011. Complexation of Arsenite with Humic Acid in the Presence of Ferric Iron. Environ. Sci. Technol. 45, 3210–3216. doi:10.1021/es102931p

Lombi, E., Scheckel, K.G., Pallon, J., Carey, A.M., Zhu, Y.G., Meharg, A.A., 2009. Speciation and distribution of arsenic and localization of nutrients in rice grains. New Phytol. 184, 193–201. doi:10.1111/j.1469-8137.2009.02912.x

Lowry, J.D., Lowry, S.B., 2002. Oxidation of As(III) by aeration and storage. NRML Off. Res. Dev.

Luciani, X., Mounier, S., Paraquetti, H.H.M., Redon, R., Lucas, Y., Bois, A., Lacerda, L.D., Raynaud, M., Ripert, M., 2008. Tracing of dissolved organic matter from the SEPETIBA Bay (Brazil) by PARAFAC analysis of total luminescence matrices. Mar. Environ. Res. 65, 148–157. doi:10.1016/j.marenvres.2007.09.004

Majumder, S., Nath, B., Sarkar, S., Chatterjee, D., Roman-Ross, G., Hidalgo, M., 2014. Size-fractionation of groundwater arsenic in alluvial aquifers of West Bengal, India: The role of organic and inorganic colloids. Sci. Total Environ. 468-469, 804–812. doi:10.1016/j.scitotenv.2013.08.087

Manceau, A., 1995. The mechanism of anion adsortion on iron oxides: Evidence for the bonding of arsenate tetrahedra on free Fe(O,OH)6 edges. Geochim. Cosmochim. Acta 59, 3647–3653.

Manceau, A., Combes, J.M., 1988. Structure of Mn and Fe oxides and oxyhydroxides: a topological approach by EXAFS. Phys. Chem. Miner. 15, 283–295.

Manceau, A., Drits, V.A., 1993. Local structure of ferrihydrite and feroxyhite by EXAFS spectroscopy. Clay Miner. 28, 165–184.

Manceau, A., Gates, W.P., 1997. Surface structural model for ferrihydrite. Clays Clay Miner. 45, 448–460.

Manders, E.M.M., Verbeek, F.J., Aten, J.A., 1993. Measurement of co-localization of objects in dual-colour confocal images. J. Microsc. 169, 375–382.

Manning, B.A., Fendorf, S.E., Goldberg, S., 1998. Surface structures and stability of arsenic (III) on goethite: spectroscopic evidence for inner-sphere complexes. Environ. Sci. Technol. 32, 2383–2388.

Manning, B.A., Hunt, M.L., Amrhein, C., Yarmoff, J.A., 2002. Arsenic (III) and arsenic (V) reactions with zerovalent iron corrosion products. Environ. Sci. Technol. 36, 5455–5461.

Marcus, M.A., MacDowell, A.A., Celestre, R., Manceau, A., Miller, T., Padmore, H.A., Sublett, R.E., 2004. Beamline 10.3.2 at ALS: a hard X-ray microprobe for environmental and materials sciences. J. Synchrotron Radiat. 11, 239–247.

Mass, M.J., Tennant, A., Roop, B.C., Cullen, W.R., Styblo, M., Thomas, D.J., Kligerman, A.D., 2001. Methylated Trivalent Arsenic Species Are Genotoxic †. Chem. Res. Toxicol. 14, 355–361. doi:10.1021/tx000251l

Matschullat, J., 2000. Arsenic in the geosphere—a review. Sci. Total Environ. 249, 297–312.

McArthur, J.., Banerjee, D.., Hudson-Edwards, K.., Mishra, R., Purohit, R., Ravenscroft, P., Cronin, A., Howarth, R.., Chatterjee, A., Talukder, T., Lowry, D., Houghton, S., Chadha, D.., 2004. Natural organic matter in sedimentary basins and its relation to arsenic in anoxic ground water: the example of West Bengal and its worldwide implications. Appl. Geochem. 19, 1255–1293. doi:10.1016/j.apgeochem.2004.02.001

McKnight, D.M., Boyer, E.W., Westerhoff, P.K., Doran, P.T., Kulbe, T., Andersen, D.T., 2001. Spectrofluorometric characterization of dissolved organic matter for indication of precursor organic material and aromaticity. Limnol. Oceanogr. 46, 38–48. doi:10.4319/lo.2001.46.1.0038

Mikutta, C., 2011. X-ray absorption spectroscopy study on the effect of hydroxybenzoic acids on the formation and structure of ferrihydrite. Geochim. Cosmochim. Acta 75, 5122–5139. doi:10.1016/j.gca.2011.06.002

Mikutta, C., Kretzschmar, R., 2011. Spectroscopic Evidence for Ternary Complex Formation between Arsenate and Ferric Iron Complexes of Humic Substances. Environ. Sci. Technol. 45, 9550–9557. doi:10.1021/es202300w

Miot, J., Morin, G., Skouri-Panet, F., Férard, C., Aubry, E., Briand, J., Wang, Y., Ona-Nguema, G., Guyot, F., Brown, G.E., 2008. XAS study of arsenic coordination in Euglena gracilis exposed to arsenite. Environ. Sci. Technol. 42, 5342–5347.

Mitsch, W.J., Gosselink, J.G., 2000. The value of wetlands: importance of scale and landscape setting. Ecol. Econ. 35, 25–33.

Morin, G., Lecocq, D., Juillot, F., Calas, G., Ildefonse, P., Belin, S., Briois, V., Dillmann, P., Chevallier, P., Gauthier, C., others, 2002. EXAFS evidence of sorbed arsenic (V) and pharmacosiderite in a soil overlying the Echassières geochemical anomaly, Allier, France. Bull. Société Géologique Fr. 173, 281–291.

Morin, G., Ona-Nguema, G., Wang, Y., Menguy, N., Juillot, F., Proux, O., Guyot, F., Calas, G., Brown Jr., G.E., 2008. Extended X-ray Absorption Fine Structure Analysis of Arsenite and Arsenate Adsorption on Maghemite. Environ. Sci. Technol. 42, 2361–2366. doi:10.1021/es072057s

Morin, G., Rousse, G., Elkaim, E., 2007. Crystal structure of tooeleite, Fe6(AsO3)4SO4(OH)4{middle dot}4H2O, a new iron arsenite oxyhydroxy-sulfate mineral relevant to acid mine drainage. Am. Mineral. 92, 193–197. doi:10.2138/am.2007.2361

Mosselmans, J.F.W., Quinn, P.., Dent, A.J., Cavill, S.., Moreno, S.D., 2009. I18-the microfocus spectroscopy beamline at the Diamond Light Source. J. Synchrotron Radiat. 16, 818–824.

Neubauer, E., Köhler, S.J., von der Kammer, F., Laudon, H., Hofmann, T., 2013a. Effect of pH and Stream Order on Iron and Arsenic Speciation in Boreal Catchments. Environ. Sci. Technol. 47, 7120–7128. doi:10.1021/es401193j

Neubauer, E., v.d. Kammer, F., Hofmann, T., 2013b. Using FLOWFFF and HPSEC to determine trace metal–colloid associations in wetland runoff. Water Res. 47, 2757–2769. doi:10.1016/j.watres.2013.02.030

Neubauer, E., von der Kammer, F., Knorr, K.-H., Peiffer, S., Reichert, M., Hofmann, T., 2013. Colloid-associated export of arsenic in stream water during stormflow events. Chem. Geol. 352, 81–91. doi:10.1016/j.chemgeo.2013.05.017

Nierop, K.G.J., Preston, C.M., Kaal, J., 2005. Thermally Assisted Hydrolysis and Methylation of Purified Tannins from Plants. Anal. Chem. 77, 5604–5614. doi:10.1021/ac050564r

Nierop, K.G.J., Verstraten, J.M., 2004. Rapid molecular assessment of the bioturbation extent in sandy soil horizons under pine using ester-bound lipids by on-line thermally assisted hydrolysis and methylation-gas chromatography/mass spectrometry. Rapid Commun. Mass Spectrom. 18, 1081–1088. doi:10.1002/rcm.1449

Nuttall, R.H., Hunter, W.N., 1995. Redetermination of 4-Hydroxy-3-nitro-benzenearsonic Acid. Acta Crystallogr. Sect. C-Org. Compd. 51, 2342–2344.

O'Day, P.A., 2006. Chemistry and mineralogy of arsenic. Elements 2, 77–83.

Olivié-Lauquet, G., Gruau, G., Dia, A., Riou, C., Jaffrezic, A., Henin, O., 2001. Release of trace elements in wetlands: role of seasonal variability. Water Res. 35, 943–952.

Ona-Nguema, G., Morin, G., Juillot, F., Calas, G., Brown, G.E., 2005. EXAFS Analysis of Arsenite Adsorption onto Two-Line Ferrihydrite, Hematite, Goethite, and Lepidocrocite. Environ. Sci. Technol. 39, 9147–9155. doi:10.1021/es050889p

Ona-Nguema, G., Morin, G., Wang, Y., Menguy, N., Juillot, F., Olivi, L., Aquilanti, G., Abdelmoula, M., Ruby, C., Bargar, J.R., Guyot, F., Calas, G., Brown, G.E., 2009. Arsenite sequestration at the surface of nano-Fe(OH)2, ferrous-carbonate hydroxide, and green-rust after bioreduction of arsenic-sorbed lepidocrocite by Shewanella putrefaciens. Geochim. Cosmochim. Acta 73, 1359–1381. doi:10.1016/j.gca.2008.12.005

Parsons, C.T., Couture, R.-M., Omoregie, E.O., Bardelli, F., Greneche, J.-M., Roman-Ross, G., Charlet, L., 2013. The impact of oscillating redox conditions: Arsenic immobilisation in contaminated calcareous floodplain soils. Environ. Pollut. 178, 254–263. doi:10.1016/j.envpol.2013.02.028

Pédrot, M., Boudec, A.L., Davranche, M., Dia, A., Henin, O., 2011a. How does organic matter constrain the nature, size and availability of Fe nanoparticles for biological reduction? J. Colloid Interface Sci. 359, 75–85. doi:10.1016/j.jcis.2011.03.067

Pédrot, M., Boudec, A.L., Davranche, M., Dia, A., Henin, O., 2011b. How does organic matter constrain the nature, size and availability of Fe nanoparticles for biological reduction? J. Colloid Interface Sci. 359, 75–85. doi:10.1016/j.jcis.2011.03.067

Pédrot, M., Dia, A., Davranche, M., Bouhnik-Le Coz, M., Henin, O., Gruau, G., 2008. Insights into colloid-mediated trace element release at the soil/water interface. J. Colloid Interface Sci. 325, 187–197. doi:10.1016/j.jcis.2008.05.019

Piccolo, A., Nardi, S., Concheri, G., 1996. Macromolecular changes of humic substances induced by interaction with organic acids. Eur. J. Soil Sci. 47, 319–328.

Pierce, M.L., Moore, C., 1982. Adsorption of arsenite and arsenate on amorphous iron hydroxide. Water Res. 16, 1247–1253.

Pinakidou, F., Katsikini, M., Simeonidis, K., Paloura, E.C., Mitrakas, M., 2015. An X-ray absorption study of synthesis- and As adsorption-induced microstructural modifications in Fe oxy-hydroxides. J. Hazard. Mater. 298, 203–209. doi:10.1016/j.jhazmat.2015.05.037

Pokrovsky, O.S., Dupré, B., Schott, J., 2005. Fe–Al–organic Colloids Control of Trace Elements in Peat Soil Solutions: Results of Ultrafiltration and Dialysis. Aquat. Geochem. 11, 241–278. doi:10.1007/s10498-004-4765-2

Pokrovsky, O.S., Schott, J., 2002. Iron colloids/organic matter associated transport of major and trace elements in small boreal rivers and their estuaries (NW Russia). Chem. Geol. 190, 141–179.

Pokrovsky, O.S., Shirokova, L.S., Kirpotin, S.N., Audry, S., Viers, J., Dupré, B., 2011. Effect of permafrost thawing on organic carbon and trace element colloidal speciation in the thermokarst lakes of western Siberia. Biogeosciences 8, 565–583. doi:10.5194/bg-8-565-2011

Polizzotto, M.L., Kocar, B.D., Benner, S.G., Sampson, M., Fendorf, S., 2008. Near-surface wetland sediments as a source of arsenic release to ground water in Asia. Nature 454, 505–508. doi:10.1038/nature07093

Pongratz, R., 1998. Arsenic speciation in environmental samples of contaminated soil. Sci. Total Environ. 224, 133–141.

Ponnamperuma, F.N., 1972. The chemistry of submerged soils. Adv. Agron. 24, 29–96.

Pourret, O., Dia, A., Davranche, M., Gruau, G., Hénin, O., Angée, M., 2007. Organo-colloidal control on major- and trace-element partitioning in shallow groundwaters: Confronting ultrafiltration and modelling. Appl. Geochem. 22, 1568–1582. doi:10.1016/j.apgeochem.2007.03.022

Ravel, B., Newville, M., 2005. ATHENA, ARTEMIS, HEPHAESTUS: data analysis for X-ray absorption spectroscopy using IFEFFIT. J. Synchrotron Radiat. 12, 537–541. doi:10.1107/S0909049505012719

Reddy, R., Delaune, R.D., 2008. Biogeochemistry of wetlands: science and applications. CRC Press edn, New-York.

Redman, A.D., Macalady, D.L., Ahmann, D., 2002. Natural Organic Matter Affects Arsenic Speciation and Sorption onto Hematite. Environ. Sci. Technol. 36, 2889–2896. doi:10.1021/es0112801

Regelink, I.C., Voegelin, A., Weng, L., Koopmans, G.F., Comans, R.N.J., 2014. Characterization of Colloidal Fe from Soils Using Field-Flow Fractionation and Fe K-Edge X-ray Absorption Spectroscopy. Environ. Sci. Technol. 48, 4307–4316. doi:10.1021/es405330x

Reiller, P.E., 2012. Modelling metal–humic substances–surface systems: reasons for success, failure and possible routes for peace of mind. Mineral. Mag. 76, 2643–2658. doi:10.1180/minmag.2012.076.7.02

Ritchie, A., 2004. An origin for arsenobetaine involving bacterial formation of an arsenic?carbon bond. FEMS Microbiol. Lett. 235, 95–99. doi:10.1016/j.femsle.2004.04.016

Ritchie, J.D., Perdue, E.M., 2003. Proton-binding study of standard and reference fulvic acids, humic acids, and natural organic matter. Geochim. Cosmochim. Acta 67, 85–96.

Ritter, K., Aiken, G., R., Ranville, J.F., Bauer, M., Macalady, D.L., 2006. Evidence for the Aquatic Binding of Arsenate by Natural Organic Matter−Suspended Fe(III). Environ. Sci. Technol. 40, 5380–5387. doi:10.1021/es0519334

Robertus, C., Philipse, W.H., Joosten, J.G.H., Levine, Y.K., 1989. Solution of the Percus–Yevick approximation of the multicomponent adhesive spheres system applied to the small angle x-ray scattering from microemulsions. J. Chem. Phys. 90, 4482.

Ronkart, S.N., Laurent, V., Carbonnelle, P., Mabon, N., Copin, A., Barthélemy, J.-P., 2007. Speciation of five arsenic species (arsenite, arsenate, MMAAV, DMAAV and AsBet) in different kind of water by HPLC-ICP-MS. Chemosphere 66, 738–745. doi:10.1016/j.chemosphere.2006.07.056

Rose, J., Vilge, A., Olivie-Lauquet, G., Masion, A., Frechou, C., Bottero, J.-Y., 1998. Iron speciation in natural organic matter colloids. Colloids Surf. -Physicochem. Eng. Asp. 136, 11–19.

Rumpel, C., Dignac, M.-F., 2006. Gas chromatographic analysis of monosaccharides in a forest soil profile: Analysis by gas chromatography after trifluoroacetic acid hydrolysis and reduction–acetylation. Soil Biol. Biochem. 38, 1478–1481. doi:10.1016/j.soilbio.2005.09.017

Ryan, J.N., Elimelech, M., 1996. Colloid mobilization and transport in groundwater. Colloids Surf. Physicochem. Eng. Asp. 107, 1–56.

Sanyal, S.K., Mou, T.J., Chakrabarty, R.P., Hoque, S., Hossain, M.A., Sultana, M., 2016. Diversity of arsenite oxidase gene and arsenotrophic bacteria in arsenic affected Bangladesh soils. AMB Express 6. doi:10.1186/s13568-016-0193-0

Schwertmann, U., Cornell, R.M., 1991. Iron oxides in the Laboratory: Preparation and Characterization, Wiley-VCH. ed. Weinheim, Germany.

Schwertmann, U., Taylor, R.M., 1979. Natural and synthetic poorly crystallized lepidocrocite. Clay Miner. 14, 285–293.

Scott, M.J., Morgan, J.J., 1995. Reactions at oxide surfaces. 1. Oxidation of As (III) by synthetic birnessite. Environ. Sci. Technol. 29, 1898–1905.

Shaheen, S.M., Rinklebe, J., Frohne, T., White, J.R., DeLaune, R.D., 2016. Redox effects on release kinetics of arsenic, cadmium, cobalt, and vanadium in Wax Lake Deltaic freshwater marsh soils. Chemosphere 150, 740–748. doi:10.1016/j.chemosphere.2015.12.043

Sharma, P., Rolle, M., Kocar, B., Fendorf, S., Kappler, A., 2011. Influence of Natural Organic Matter on As Transport and Retention. Environ. Sci. Technol. 45, 546–553. doi:10.1021/es1026008

Shen, S., Li, X.-F., Cullen, W.R., Weinfeld, M., Le, X.C., 2013. Arsenic Binding to Proteins. Chem. Rev. 113, 7769–7792. doi:10.1021/cr300015c

Sherman, D.M., Randall, S.R., 2003. Surface complexation of arsenic(V) to iron(III) (hydr)oxides: structural mechanism from ab initio molecular geometries and EXAFS spectroscopy. Geochim. Cosmochim. Acta 67, 4223–4230. doi:10.1016/S0016-7037(03)00237-0

Sjöstedt, C., Persson, I., Hesterberg, D., Kleja, D.B., Borg, H., Gustafsson, J.P., 2013. Iron speciation in soft-water lakes and soils as determined by EXAFS spectroscopy and geochemical modelling. Geochim. Cosmochim. Acta 105, 172–186. doi:10.1016/j.gca.2012.11.035

Smedley, P.L., Kinniburgh, D.G., 2002. A review of the source, behavior and distribution of arsenic in natural waters. Appl. Geochem. 17, 517–568.

Smith, P.G., Koch, I., Gordon, R.A., Mandoli, D.F., Chapman, B.D., Reimer, K.J., 2005. X-ray Absorption Near-Edge Structure Analysis of Arsenic Species for Application to Biological Environmental Samples. Environ. Sci. Technol. 39, 248–254. doi:10.1021/es049358b

Sposito, G., Weber, J.H., 1986. Sorption of trace metals by humic materials in soils and natural waters. Crit. Rev. Environ. Control 16, 193–229. doi:10.1080/10643388609381745

Stolpe, B., Hassellöv, M., 2007. Changes in size distribution of fresh water nanoscale colloidal matter and associated elements on mixing with seawater. Geochim. Cosmochim. Acta 71, 3292–3301. doi:10.1016/j.gca.2007.04.025

Stumm, W., Morgan, J.J., Drever, J.I., 1996. Aquatic Chemistry. J. Environ. Qual. 25, 1162.

Takahashi, Y., Minamikawa, R., Hattori, K.H., Kurishima, K., Kihou, N., Yuita, K., 2004. Arsenic Behavior in Paddy Fields during the Cycle of Flooded and Non-flooded Periods. Environ. Sci. Technol. 38, 1038–1044. doi:10.1021/es034383n

Tamaki, S., Frankenberger, W.T., 1992. Environmental Biochemistry of Arsenic. Rev. Environ. Contam. Toxicol. 124, 79–110.

Tang, J., Johannesson, K.H., 2003. Speciation of rare earth elements in natural terrestrial waters: assessing the role of dissolved organic matter from the modeling approach. Geochim. Cosmochim. Acta 67, 2321–2339. doi:10.1016/S0016-7037(02)01413-8

Teasdale, P.R., Allen, L., Apte, S.C., Batley, G.E., Birch, G., 1998. In situ collection of diagenetic and induced oxyhydroxide precipitates from riverine and estuarine sediments. Environ. Technol. 19, 1191–1201.

Teixeira, J., 1988. Small-angle scattering by fractal systems. J. Appl. Crystallogr. 21, 781–785. doi:10.1107/S0021889888000263

Thanabalasingam, P., Pickering, W.F., 1986. Effect of pH on interaction between As (III) or As (V) and manganese (IV) oxide. Water. Air. Soil Pollut. 29, 205–216.

ThomasArrigo, L.K., Mikutta, C., Byrne, J., Barmettler, K., Kappler, A., Kretzschmar, R., 2014. Iron and Arsenic Speciation and Distribution in Organic Flocs from Streambeds of an Arsenic-Enriched Peatland. Environ. Sci. Technol. 48, 13218–13228. doi:10.1021/es503550g

Thompson, A., Chadwick, O.A., Rancourt, D.G., Chorover, J., 2006. Iron-oxide crystallinity increases during soil redox oscillations. Geochim. Cosmochim. Acta 70, 1710–1727. doi:10.1016/j.gca.2005.12.005

Thoral, S., Rose, J., Garnier, J.M., Van Geen, A., Refait, P., Traverse, A., Fonda, E., Nahon, D., Bottero, J.Y., 2005. XAS study of iron and arsenic speciation during Fe (II) oxidation in the presence of As (III). Environ. Sci. Technol. 39, 9478–9485.

Thurman, E., 1985. Organic Geochemistry of Natural Waters. Springer.

Tipping, E., 1998. Humic ion-binding model VI: an improved description of the interactions of protons and metal ions with humic substances. Aquat. Geochem. 4, 3–47.

Tipping, E., Rey-Castro, C., Bryan, S.E., Hamilton-Taylor, J., 2002. Al (III) and Fe (III) binding by humic substances in freshwaters, and implications for trace metal speciation. Geochim. Cosmochim. Acta 66, 3211–3224.

Vermeer, A.W.P., Van Riemsdijk, W.H., Koopal, L.K., 1998. Adsorption of humic acid to mineral particles. 1. Specific and electrostatic interactions. Langmuir 14, 2810–2819.

Vilgé-Ritter, A., Rose, J., Masion, A., Bottero, J.-Y., Lainé, J.-M., 1999. Chemistry and structure of aggregates formed with Fe-salts and natural organic matter. Colloids Surf. Physicochem. Eng. Asp. 147, 297–308.

Voegelin, A., Kaegi, R., Frommer, J., Vantelon, D., Hug, S.J., 2010. Effect of phosphate, silicate, and Ca on Fe(III)-precipitates formed in aerated Fe(II)- and As(III)-containing water studied by X-ray absorption spectroscopy. Geochim. Cosmochim. Acta 74, 164–186. doi:10.1016/j.gca.2009.09.020

Voegelin, A., Weber, F.-A., Kretzschmar, R., 2007. Distribution and speciation of arsenic around roots in a contaminated riparian floodplain soil: Micro-XRF element mapping and EXAFS spectroscopy. Geochim. Cosmochim. Acta 71, 5804–5820. doi:10.1016/j.gca.2007.05.030

Wang, H., Shadman, F., 2013. Effect of particle size on the adsorption and desorption properties of oxide nanoparticles. AIChE J. 59, 1502–1510. doi:10.1002/aic.13936

Wang, S., Mulligan, C.N., 2006. Natural attenuation processes for remediation of arsenic contaminated soils and groundwater. J. Hazard. Mater. 138, 459–470. doi:10.1016/j.jhazmat.2006.09.048

Waychunas, G.A., Rea, B.A., Fuller, C.C., Davis, J.A., 1993. Surface chemistry of ferrihydrite: Part1. EXAFS studies of the geometry of coprecipitated and adsorbed arsenate. Geochim. Cosmochim. Acta 57, 2251–2269.

Weng, L., Van Riemsdijk, W.H., Hiemstra, T., 2009. Effects of Fulvic and Humic Acids on Arsenate Adsorption to Goethite: Experiments and Modeling. Environ. Sci. Technol. 43, 7198–7204. doi:10.1021/es9000196

Wershaw, R.L., 1999. Molecular aggregation of humic substances. Soil Sci. 164, 775–876.

Wilkie, J.A., Hering, J.G., 1996. Adsorption of arsenic onto hydrous ferric oxide: effects of adsorbate/adsorbent ratios and co-occurring solutes. Colloids Surf. -Physicochem. Eng. Asp. 107, 97–110.

Yamaguchi, N., Ohkura, T., Takahashi, Y., Maejima, Y., Arao, T., 2014. Arsenic Distribution and Speciation near Rice Roots Influenced by Iron Plaques and Redox Conditions of the Soil Matrix. Environ. Sci. Technol. 48, 1549–1556. doi:10.1021/es402739a

Yean, S., Cong, L., Yavuz, C.T., Mayo, J.T., Yu, W.., Kan, A.T., Colvin, V.L., Tomson, M.B., 2005. Effect of magnetite particle size on adsorption and desorption of arsenite and arsenate. J. Mater. Res. 20, 3255–3264.

Zhao, Z., Jia, Y., Xu, L., Zhao, S., 2011. Adsorption and heterogeneous oxidation of As(III) on ferrihydrite. Water Res. 45, 6496–6504. doi:10.1016/j.watres.2011.09.051

Zhukhlistov, A.P., 2001. Crystal structure of lepidocrocite FeO (OH) from the electron-diffractometry data. Crystallogr. Rep. 46, 730–733.

Zsolnay, A., Baigar, E., Jimenez, M., Steinweg, B., Saccomandi, F., 1999. Differentiating with fluorescence spectroscopy the sources of dissolved organic matter in soils subjected to drying. Chemosphere 38, 45–50. doi:10.1016/S0045-6535(98)00166-0

ANNEXES

Annexe I TEM micrographs of the 3-0.2µm fraction

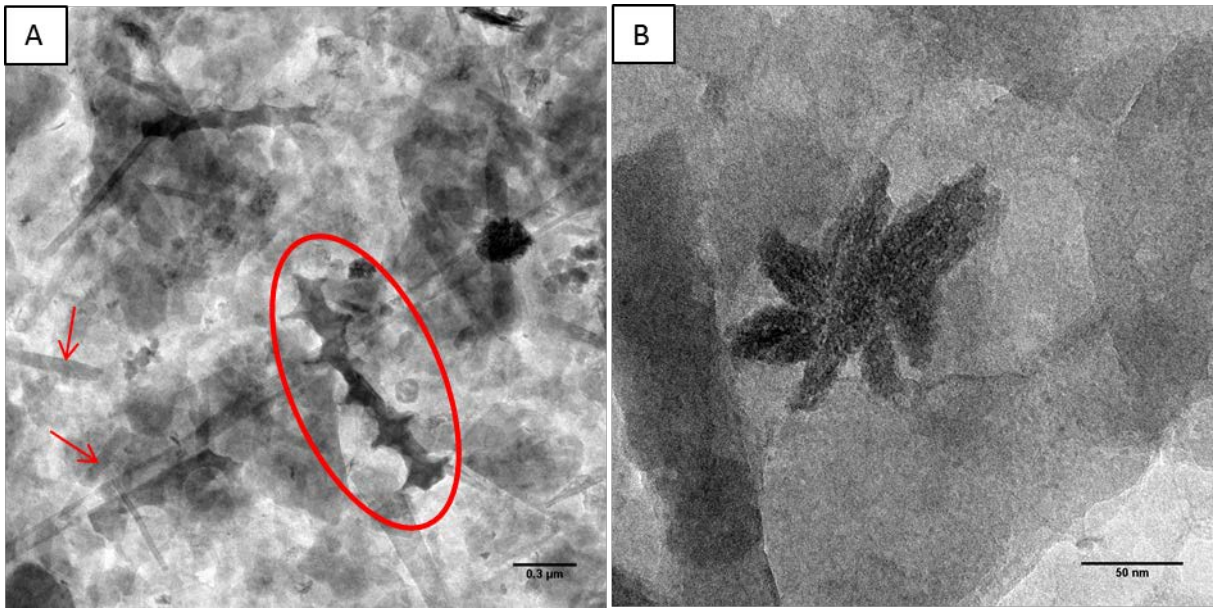

Annexe I TEM micrographs of the 3-0.2µm fraction showing: A) Diatoms remains (red circle) with silicate plants (ed arrows) and B) Goethite-like crystal.

Annexe II Calibration curves for HPLC measurements and recovery estimation

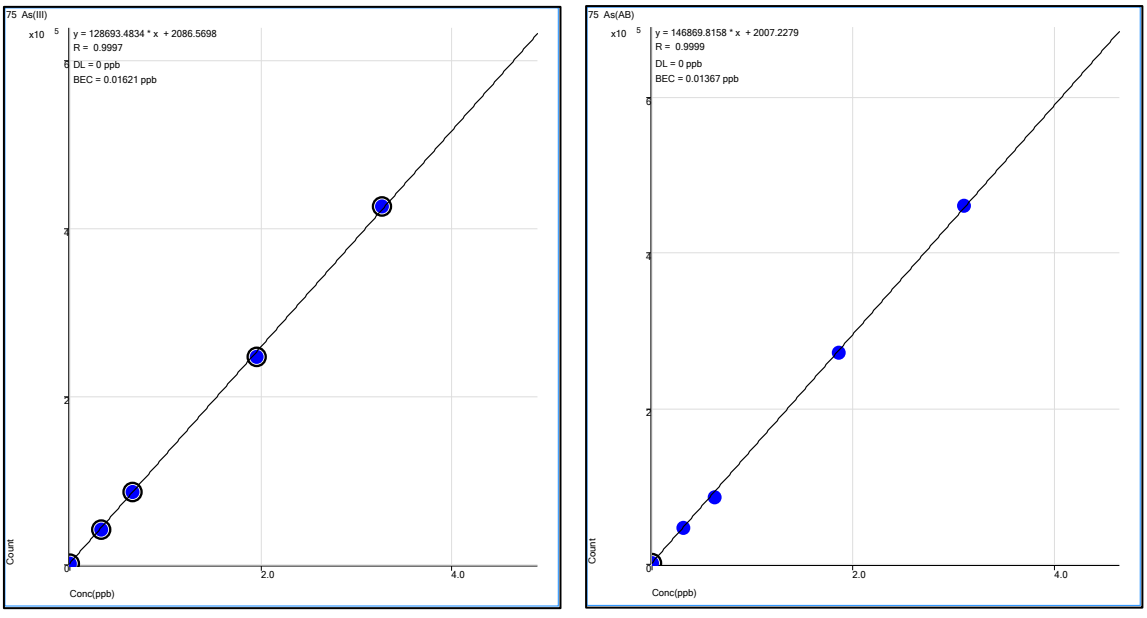

Annexe II-1 Calibration curves for As(III) and AB standards injected at different concentrations

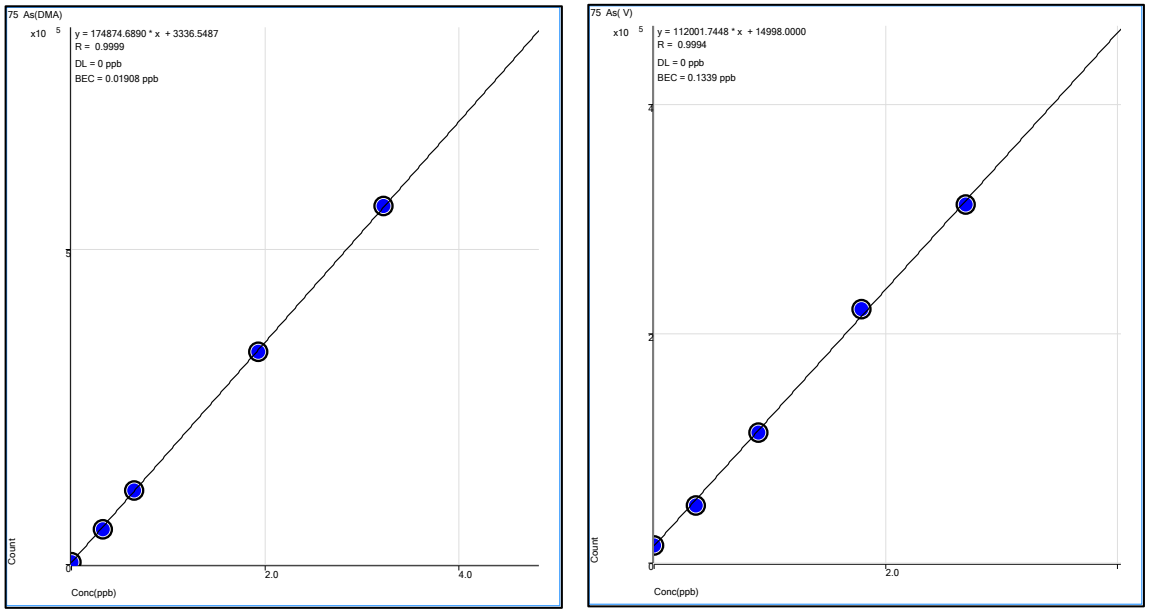

Annexe II-2 Calibration curves for DMA and As(V) standards injected at different concentrations

Annexe II-3 Estimation of As recovery in the samples (<5 kDa and <30kDa), using the concentrations determined by the calibration curves and the concentrations determined by directly injecting the sample in the ICP-MS.

	<5kDa	**<30kDa**
As(III)	0.02	0.23
AsB	0.32	0.35
DMA	0.14	0.16
As(V)	0.98	0.88
As tot (ppb)	1.46	1.62
As direct (ppb)	2.24	5.11
Recovery (%)	65	32